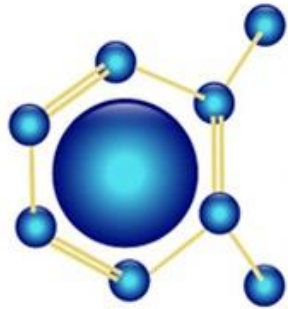# SETCOR
Conferences & Events

S M S
Smart Materials and Surfaces

B A N G K O K   2 0 1 4
Conference And Exhibition
26 - 28 August 2014

Sheraton Grande Sukhumvit Hotel - Bangkok-Thailand

Smart Materials and Surfaces

SMS Bangkok 2014 International Conference Proceeding

www.setcor.org/conferences/SMS-Bangkok-2014

Table of contents

Smart Materials and Surfaces: Fabrication, Characterization & Properties

Smart Materials and Surfaces for Energy and Environment

	O. Abbes, A. Portavoce, C. Girardeaux, A. Spiesser, and V. Le Thanh GREMI CNRS-Université d'Orléans, Aix-Marseille Université, CNRS, IM2NP-UMR 6242 and Aix-Marseille Université, CNRS, CINaM-UMR 7325, Marseille, **France**
10	**Strength and Ductility of SGFRP Confined Concrete**
	Q. Hussain, A. Pimanmas and **L. Lalin**, Sirindhorn International Institute of Technology, Thammasat University, Thailand.
11	**Smart Focused-Ion-Beam-fabricated Nanostructures for Improving Sur-face Enhanced Raman Scattering on Trace Detection of Single Molecules**
	K. Sivashanmugan, J-D Liao and C-K Yao Department of Materials Science and Engineering, Center for Micro/Nano Science and Technology, Nation-al Cheng Kung University, **Taiwan**.
12	**Nanostructured metal oxides: catalyst-free synthesis, characterization and Integration with MEMS processing for gas sensor**
	S. Chandra and B. Behera Centre for applied Research in Electronics, Indian Institute of Technology Delhi, India
13	**A Microscale Piezoelectric Harvester for Mechanical Energy from Fluid Flow**
	K. Koyvanich, N. Muensit and P. Smithmaitrie Center of Excellence in Nanotechnology for Energy (CENE), Physics Department, Faculty of Science and Department of Mechanical Engineering, Faculty of Engineering, Prince of Songkla University (PSU), HatYai, Songkla, **Thailand.**
14	**Effect of electron beam on thermal, morphological and anti-oxidant properties of kraft lignin**
	T.Venkatappa Rao, N.Rajeswara Rao, SVS Ramana Reddy and B.Sanjeeva Rao National Institute of Technology, Warangal, **India**
15	**Facile growth of carbon nanotube electrode from electroplated Ni catalyst for supercapacitors**
	V. Yordsri, **W. Wongwiriyapan** and C. Thanachayanont College of Nanotechnology, King Mongkut's Institute of Technology Ladkrabang/ Nanotec-KMITL Center of Excellence on Nanoelectronic Device/ Thailand Center of Excellence in Physics/ National Metal and Materials Technology Center, **Thailand**

Smart Materials and Surfaces for life science

1.	**Immobilization of Urease Based on Adsorption in Eggshell Membrane for Urea Biosensor Application**
	T. Suwanchaituch, S. Imthong and **K. Panpae** Department of Chemistry, Faculty of Science, King Mongkut's University of Technology Thonburi, KMUTT, Bangkok, **Thailand**
2.	**Needle-less Jet Injection System with Multi-Pore Nozzle for Viscous Drug Delivery Applications**
	Y. C. Jo, H. K. Hong, Y. S. Choi and H. S. Kim Korea Electronics Technology Institute, Medical IT Convergence Research Center, SeongNam-Si and Korea Electronics Technology Institute, Contents Research Center, SeongNam-Si, **South Korea**

Silicon Nitride Protective Coating by Gas-timing RF Magnetron Sputtering Deposition

N. Khemasiri[1], N. Paleeya[1], D. Sae-tang Phromyothin[1], M. Horprathum[2], S.Porntheeraphat[2], A. Sungthong[3] J. Nukeaw[1] and S. Pratontep[1*]

[1]College of Nanotechnology, King Mongkut's Institute of Technology Ladkrabang, Bangkok 10520, Thailand
[2]National Electronics and Computer Technology Center (NECTEC), NSTDA, Pathumthani 12120, Thailand
[3]Rajanagarindra Rajabhat University, Chachoengsao 24000, Thailand
[*]Corresponding author. Tel: (+66) 3298000 ext. 3077; E-mail: kpsirapa@live.kmitl.ac.th

Abstract: Protective coating based on silicon nitride is a promising alternative to carbon based coatings, owing to its compatibility with existing semiconductor technology. However, the fabrication of silicon nitride thin films, e.g. reactive sputtering and chemical vapor deposition, often face difficulties in obtaining desirable properties, owing to the complexity of the process and contaminations. Here we explore a method to better control the properties of silicon nitride thin films from plasma sputtering deposition by the gas-timing technique. The gas-timing sputtering technique controls the on-off sequence of the reactive sputtering gases during deposition. In this study, Ar plasma sputtering with a pure silicon target was employed. The Ar gas was injected in alternation with N_2 gas with the timing ratio (in seconds) of Ar:N_2 from 10:0, 10:1, 10:3, 10:5, 10:7 and 10:10. The effect of the gas-timing ratio on the properties of silicon nitride films was investigated by Atomic Force Microscopy, Raman Spectroscopy, Auger Electron Spectroscopy, X-ray Diffraction. The chemical resistance was measured by electrochemical corrosion test in sulfuric acid, while the hardness was obtained by the nano-indentation technique. The results reveal that while the gas timing technique is able to slightly vary the nitrogen content in the films, other properties of the films are significantly improved, such as surface morphology, acid corrosion resistance, hardness properties.

Keywords: hard coatings, silicon nitride, corrosion, plasma sputtering

Introduction

Silicon Nitride (Si_3N_4) is a promising candidate for hard coating applications, owing to high corrosion resistance, high hardness value, chemical and thermal stability [1]. The main advantage is its compatibility to the silicon-based microfabrication technology. In general, silicon nitride coating may be fabricated by several processes, such as chemical vapor deposition [2]. However, such processes often require high operating temperature and hazardous chemicals as the nitrogen source. RF magnetron sputtering is an alternative technique for silicon nitride fabrication, which offers a low temperature operation, and high

film adhesion [3]. Conventional magnetron sputtering with a homogenous mixture of sputtering gas and reactive gas often has a drawback of the difficulties in precisely controlling the properties. Recently, a novel rf magnetron sputtering technique called "reactive gas-timing" with an on-off sequence of reactive and sputtering gases have been demonstrated in metal oxynitride thin film fabrication with a precise control the properties and the composition of the films [4,5].

In this research, silicon nitride thin films have been fabricated by reactive gas-timing rf magnetron sputtering system without substrate heating or substrate bias. We investigate the effect of the nitrogen timing (1, 3, 7 and 10 s) alternated with a fixed Ar timing of 10 s on the properties of the deposited films by atomic force microscopy, Raman spectroscopy, Auger electron spectroscopy, electrochemical corrosion test, and nanoindentation.

Experimental

Sputtered silicon nitride (SiN_x) thin films with different Ar:N_2 timing ratios were fabricated onto p-type si(100) and glass substrates by rf magnetron sputtering system with reactive gas-timing technique using a 99.999% silicon target. The target was also cleaned by pre-sputtering with pure Ar at the start of each run. The substrates were ultrasonically cleaned in isopropanol alcohol, acetone, DI water and then dried by N_2.blow gun. The sputtering conditions are listed in Table 1.

The properties of the deposited silicon nitride thin films were investigated: surface morphology by Atomic Force Microscope (AFM, Seiko SPI400) in the non-contact mode, chemical composition by Auger Electron Spectroscopy (AES, ULVAC PHI700,

Table 1: Sputtering parameters for SiN_x deposition

Deposition parameter	Condition
Base pressure	6.0×10^{-6} mbar
RF Power	80 W
Sputtering temperature	Room temperature
Ar flow rate	10 sccm
N_2 flow rate	3 sccm
Ar timing	10 sec
N_2 timing	1, 3, 7, 10 sec
Film thickness	100 nm
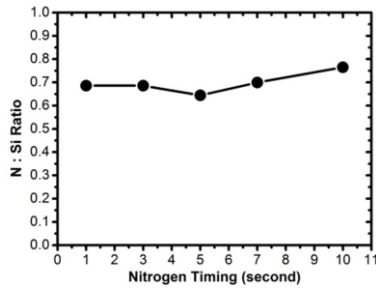
Figure 1: N:Si composition ratio of the silicon nitride thin films as a function of N timing.

Figure 2: Surface roughness (rms, 1 μm^2 area) of the silicon nitride thin films deposited with different N timing.

measured at 10 nm below the surface), and chemical bonding by Raman spectroscopy (Thermo Scientific DXR Smart Raman). The anticorrosion performance was studied by the electrochemical corrosion test (Autolab PGST AT302) in 1M H_2SO_4 (Sigma-Aldrich). The hardness of the silicon nitride coatings was characterized by nanoindentation (Micro Materials), with the load range of 0-1000 μN using the Berkovich tip.

Results and Discussion

Figure 1 shows the N:Si atomic composition ratio obtained by AES as a function of the N gas-timing duration. The content of N in the sputtered films increases slightly with the N:Si ratios around 70-75%, as the N injection duration expands. The AES results also indicate that some oxygen is present in the films, possibly for the background gases. The Raman results (not shown) confirm a mixture of a Si-N_x phase and possibly a Si or a Si-O phase.

From such small increase in the N content in the films, other properties of the films are not expected to vary greatly. Figure 2 illustrates that the root-mean-square (rms) surface roughness measured by AFM exhibit a sharp increase for the Ar:N_2 timing ratio of 10:7. The corrosion test results as shown in Fig. 3 also demonstrate such trend. The corrosive current significantly decreases at high N timing, with the lowest current at the 10:7 ratio.

Figure 4 illustrates the hardness and elastic modulus results from the force-displacement curve obtained by the nanoindentation. As the N timing increases, the hardness of the silicon nitride films gradually increases, while the elastic modulus exhibit the opposite trend. In other words, at long N timing, the films become stronger but less rigid. This suggests that the timing sequence may induce better N-incorporation and some structural differences in the films, possibly multilayers.

Conclusions

This work demonstrate that N content may not be the only factor that affects the film properties in reactive sputtering processes. The reactive gas-timing sputtering technique offers a better control of the properties, together with the composition and the structure of the films.
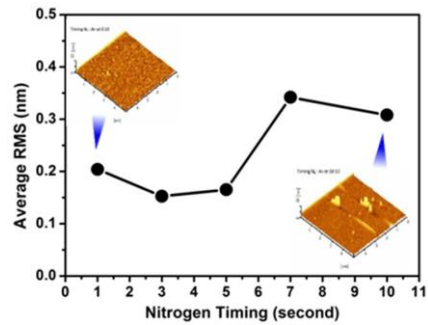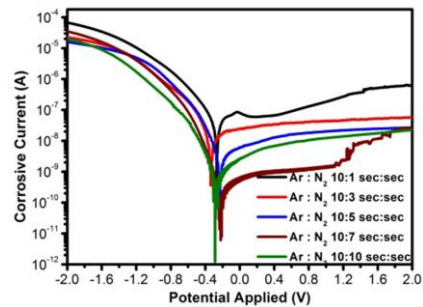
Figure 3: I-V polarization curve of the silicon nitride thin films in 1M H_2SO_4.
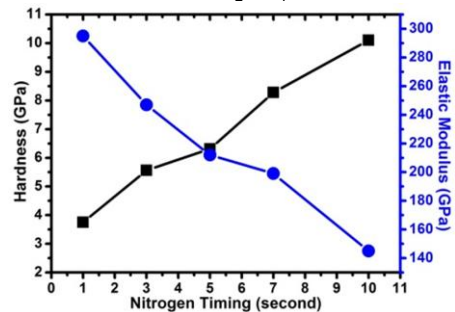
Figure 4: Hardness and elastic modulus of the silicon nitride thin films deposited with different N timing.

References

1. Krstic, Z., Krstic, V.D. (2012) *J. Mater. Sci.*, 47, 535-552.
2. Oliphant, C.J., *et al.* (2013) *Appl. Surf. Sci.*, 285P, 440-449.
3. Zambom, L.S. *et al.* (2012) *Microelectr. J.*, 40, 66-69.
4. Nukeaw, J., Sungthong, A., T-Thienprasert. *et al.* (2008) *App. Phys. Lett,.* 93, 051903.
5. Klaitabtim, D., Pratontep, S., Nukeaw, J. (2008) *Ceram. Int.*, 34, 1103-1107.

Simple Methods to Fabricate Multilayer Microfluidic Devices

T. Jiemsakul [1], C. Kortchana [2], S. Manakasettharn [1,*]

[1]National Nanotechnology Center, Integrated Nanosystem Laboratory, Pathum Thani, Thailand

[2]King Mongkut's Institute of Technology Ladkrabang, College of Nanotechnology, Bangkok, Thailand

*Corresponding author, supone@nanotec.or.th

ABSTRACT

Microfluidic devices have attracted wide attention with practical applications to microtechnology and nanotechnology, primarily due to their advantages such as low fluid volume consumption and compactness of the devices. Microfluidic devices can consist of one or more microchannels with at least one dimension less than 1 mm. In traditional two-layer microfluidic devices, the microchannels are fabricated on a substrate (the first layer) and are then sealed with a cover plate (the second layer). In multilayer microfluidic devices, longer microchannels can be fabricated to achieve more performances. This work presents two simple methods to fabricate multilayer microfluidic devices. For the first method, we have used a CO_2 laser beam to cut through 100-µm-thick polyvinyl chloride (PVC) substrates to create microchannels. For the second one, we have used the CO_2 laser beam to engrave microchannels on 1-mm-thick poly(methyl methacrylate) (PMMA) substrates. The cover plates are made of the same material. For both methods, we have used thermal bonding to bond substrates and cover plates together. The PVC microchannels resulting from the first method have approximately rectangular cross-sections, where as the engraved PMMA microchannels have approximately triangular cross-sections. The depth of the PVC microchannels is controlled by the thickness of the PVC substrates, whereas the depth of the engraved PMMA microchannels depends on laser power. The width of microchannels for both methods can be adjusted by varying the laser power. Compared to conventional photolithography, these two fabrication methods are simpler, faster, and cheaper. We hope that these two methods will be implemented to manufacture sophisticated multilayer microfluidic devices

Keywords

Microfluidic devices, microchannels, multilayer, fabrication, CO_2 laser, polyvinyl chloride, PVC, poly(methyl methacrylate), PMMA.

1. INTRODUCTION

Microfluidic devices have received wide interest with practical applications to microtechnology and nanotechnology, mainly due to their advantages such as low fluid volume consumption and compactness of the devices. As early as 1975, a microfluidic device was fabricated on silicon using integrated circuit technology consisting of a series of deposition, photolithography, and etching steps [1]. Later, methods to fabricate microfluidic devices have been developed [2]. This work presents simple methods to fabricate microchannels using CO_2 laser cutting and engraving on substrates. Later, the substrates were thermally bonded together to form closed microchannels and multilayer microfluidic devices.

2. EXPERIMENTAL SECTION

2.1 Materials and apparatus

We used 100-µm-thick polyvinyl chloride (PVC) transparency sheets (OfficeMate Plc., Thailand) and 1-mm-thick poly(methyl methacrylate) (PMMA) sheets (Panglas, Pan Asia Industrial Co., Ltd., Thailand) as substrates since they are transparent, thin, cheap, and locally available. We used DraftSight and LaserWorkV6 software to design microchannels. Later, microchannels were fabricated on the substrates by the computer controlled CO_2 laser machine (SMLA-9060, Nextconcept9999 Co., Ltd., Thailand). Isopropyl alcohol (Fisher Scientific Ltd., UK) was used to clean the substrates. The fold back clips (No.415/No.111, Horse, Nanmee Co., Ltd., Thailand) and the microscope slides (No.7101, Sail Brand, China) were used to clamp the substrates in the glass oven (B-585, Buchi (Thailand) Co. Ltd., Thailand) for thermal bonding. The optical microscope (BX51M, Olympus Corp., Japan) was used to characterize the sizes of the fabricated microchannels.

2.2 Fabrication of PVC microchannels

For the first method to fabricate microchannels, we used the CO_2 laser beam to cut through the 100-µm-thick PVC substrates. To form the closed microchannels, two PVC substrates were thermally bonded on top and bottom of the PVC substrate with the cut-through microchannels at 140℃ for 20 min. To form multilayer microfluidic devices, multilayers of PVC substrates with the microchannels were thermally bonded together.

2.3 Fabrication of PMMA microchannels

For the second method, we used the CO_2 laser beam to engrave microchannels on the 1-mm-thick PMMA substrates. Another PMMA substrate was thermally bonded on top of the PMMA substrate with the engraved microchannels at 120℃ for 20 min to form the closed microchannels. Multilayers of PMMA substrates with the microchannels were thermally bonded together to form multilayer microfluidic devices.

3. RESULTS AND DISCUSSION
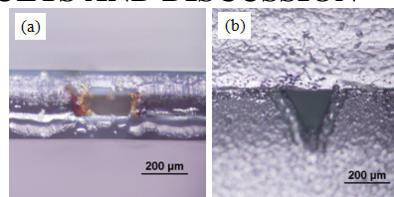
Figure. 1 The optical microscope images showing the cross-section of (a) a PVC microchannel and (b) a PMMA microchannel.
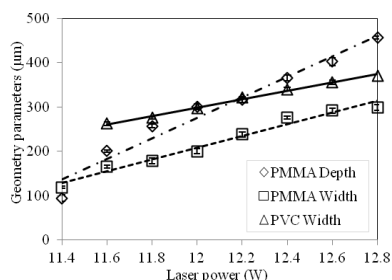
Figure. 2 Relationships between laser power and geometrical parameters of microchannels.

3.1 Laser cutting of PVC microchannels

The CO_2 laser machine generated the continuously focused laser beam with a wavelength of 10.6 µm to heat the substrates. The 100-µm-thick PVC substrates were melted and cut through with laser power of 11.6 W and above at the speed of the laser beam of 4 mm/s. The cross-section of the closed PVC microchannel is approximately rectangular as shown in Figure.1(a). The influence of laser cutting power on the width of the PVC microchannels is shown in Figure.2. The average width of the cut-through PVC microchannels increases linearly from 263 µm to 371 µm with the laser cutting power varied from 11.6 W to 12.8 W at the constant speed of the laser beam of 4 mm/s. The depth of the PVC microchannels is controlled by the thickness of the PVC substrates.

3.2 Laser engraving of PMMA microchannels

Figure.1(b) shows the cross-section of a PVC microchannel having approximately a triangular shape. Figure.2 presents the influence of laser engraving power on the width and the depth of the engraved PMMA microchannel. The laser engraving power was varied from 11.4 W to 12.8 W at the constant speed of the laser beam of 10 mm/s. The average depth of the PMMA microchannels increases linearly with the laser cutting power from 95 µm to 456 µm while the average width of the PMMA microchannels increases slightly 119 µm to 299 µm. Our results of laser engraving on PMMA substrates and thermal bonding are comparable to the previous work [3]. The 1-mm-thick PMMA substrates are thick enough to use laser engraving in the range of a set of the laser power mentioned above.

3.3 Multilayer microfluidic devices

In this work, we fabricated two designs of multilayer microfluidic devices with different materials, i.e. PVC and PMMA, using laser cutting and laser engraving. Figure.3 presents schematic illustrations of the exploded views of the fabricated multilayer microfluidic devices in Figure.4. Figures.4(a),(c) show seven-layer PVC microfluidic devices with total thickness of 0.7 mm. Figures.4(b),(d) show 4.1-mm-thick multilayer microfluidic devices consisting of four PMMA layers and a PVC bottom layer. Figures.4(a),(b) show the multilayer microfluidic devices consisting of three microchannels with red, green, and blue dyed water inside crossing over and under each other. Figures.4(c),(d) show the multilayer microfluidic devices consisting of the microchannel with blue dyed water inside alternately crossing over and under the microchannel with red dyed water inside. With the same design of microchannels, using laser cutting of microchannels requires more layers to form multilayer microfluidic devices compared to using laser engraving of microchannels.
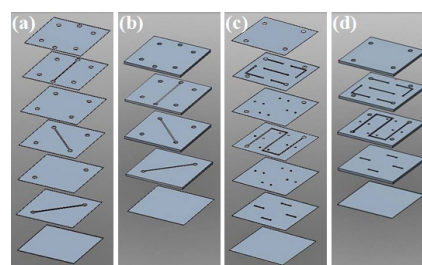
Figure. 3 Schematic illustrations of the exploded views of multilayer microfluidic devices in Figure. 4(a)-(d), respectively.
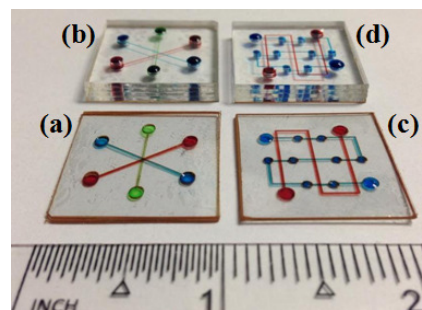
Figure. 4 A photograph of four fabricated multilayer microfluidic devices next to the ruler.

4. CONCLUSION

We have demonstrated the fabrication of the microchannels using CO_2 laser cutting on the 100-µm-thick PVC substrates and CO_2 laser engraving on the 1-mm-thick PMMA substrates. The PVC and the PMMA substrates were bonded thermally to form the closed microchannels and multilayer microfluidic devices. The cross-sections of the cut-through PVC microchannels and the engraved PMMA microchannels are approximately rectangular and triangular, respectively. The laser power has influence on the width of the cut-through microchannels and the engraved microchannels. The laser power also has influence on the depth of the engraved microchannels, whereas the depth of the cut-through microchannels is controlled by the thickness of the substrates. These simple methods can be implemented in the fabrication of sophisticated multilayer microfluidic devices.

5. ACKNOWLEDGMENT

6. REFERENCES

[1] Terry, S. C. 1975. *A Gas Chromatography System Fabricated on a Silicon Wafer using Integrated Circuit Technology.* Ph.D. Dissertation, Stanford University, Stanford, CA. Also, Stanford Electronics Laboratories Technical Report No. 4603-1.

[2] Abgrall, P., and Gue, A.-M. 2007. Lab-on-chip technologies: making a microfluidic network and coupling it into a complete microsystem—a review. *J. Micromech. Microeng.* 17, 5 (Apr. 2007), R15-R19.

[3] Sun, Y., Kwok, Y. C., and Nguyen, N.-T. 2006. Low-pressure, high-temperature thermal bonding of polymeric microfluidic devices and their applications for electrophoretic separation. *J. Micromech. Microeng.* 16, 8 (July 2006), 1681-1688.

Electrochromic Materials and their Characterization by Solar Radiation Glazing Factors for Smart Window Applications

Bjørn Petter Jelle [ab*], Tao Gao [c], Yingpeng Zhen [b] and Arild Gustavsen [c]

[a] SINTEF Building and Infrastructure,
Department of Materials and Structures, NO-7465 Trondheim, Norway.

[b] Norwegian University of Science and Technology (NTNU),
Department of Civil and Transport Engineering, NO-7491 Trondheim, Norway.

[c] Norwegian University of Science and Technology (NTNU),
Department of Architectural Design, History and Technology, NO-7491 Trondheim, Norway.

* Corresponding author: bjorn.petter.jelle@sintef.no (e-mail), +47-73593377 (phone).

Abstract

Electrochromic materials (ECM) and windows (ECW) are able to regulate the solar radiation throughput by application of an external electrical voltage. Hence, as smart window applications, the ECWs may decrease heating, cooling and electricity loads in buildings by admitting the optimum level of solar energy and daylight into the buildings at any given time, e.g. cold winter climate versus warm summer climate demands. In order to achieve as dynamic and flexible solar radiation control as possible, the ECWs may be characterized by solar radiation glazing factors, i.e. ultraviolet solar transmittance (T_{uv}), visible solar transmittance (T_{vis}), solar transmittance (T_{sol}), solar material protection factor (SMPF), solar skin protection factor (SSPF), external visible solar reflectance ($R_{vis,ext}$), internal visible solar reflectance ($R_{vis,int}$), solar reflectance (R_{sol}), solar absorbance (A_{sol}), emissivity (ε), solar factor (SF) and colour rendering factor (CRF). Comparison of these important solar quantities for various ECM and ECW combinations and configurations enables one to select the most appropriate ones for specific smart window and building applications.

Keywords: Electrochromic, Smart, Material, Window, Solar radiation, Solar factor, Solar heat gain coefficient.

Introduction

The application of electrochromic materials (ECM) in electrochromic windows (ECW) aims at controlling the solar radiation throughput at the earth's surface, which is roughly located between 300 nm and 3000 nm. Such windows are often denoted smart windows. The ECW solar control is achieved by application of an external voltage. The visible (VIS) light lies between 380 and 780 nm. Ultraviolet (UV) and near infrared (NIR) radiation are located below and above the VIS region, respectively. Above 3000 nm, and not part of the direct solar radiation, lies the thermal radiation called infrared (IR) radiation, which all materials radiate above 0 K, peaking around 10 000 nm (10 μm) at room temperature. However, the ECWs are not aimed at controlling the IR radiation. Normally, as low as possible heat loss through windows is desired, i.e. low U-value, which is accomplished by the application of various static low emissivity coatings on the window glass panes. Miscellaneous ECMs and ECWs and their various properties are investigated in the literature [1-10]. Some commercial ECWs are also already on the market [8,9]. ECMs and ECWs may also be used together with other materials and technologies, e.g. self-cleaning glazing materials and building integrated photovoltaics (BIPV) like solar cell glazing [11-15]. In general, it is of major importance to investigate the durability of building materials and components, also newly developed ones like e.g. ECMs and ECWs, which may be performed by carrying out accelerated climate ageing in the laboratory [16]. Thus, conducting a robustness assessment of these materials and components may also be found to be beneficial [17]. Hence, a durability and robustness evaluation of the new ECMs and ECWs should be carried out. This work presents two ECWs and their readily characterization by solar radiation glazing factors, i.e. ultraviolet solar transmittance (T_{uv}), visible solar transmittance (T_{vis}), solar transmittance (T_{sol}), solar material protection factor (SMPF), solar skin protection factor (SSPF), external visible solar reflectance ($R_{vis,ext}$), internal visible solar reflectance ($R_{vis,int}$), solar reflectance (R_{sol}), solar absorbance (A_{sol}), emissivity (ε), solar factor (SF) and colour rendering factor (CRF). The solar factor (SF), which is the total solar energy transmittance, is also often denoted as the solar heat gain coefficient (SHGC) and the g-value. Further details about the solar radiation glazing factors are given in the literature [10,18,19].

Experimental

For various experimental details concerning the synthesis and manufacturing of the ECMs and ECWs, and their electrochemical and spectroscopical characterization, it is referred to the studies by Jelle [10], Jelle and Hagen [20-22] and Jelle et al. [23]. In short, the ECMs polyaniline (PANI), prussian blue (PB)

and tungsten oxide (WO_3) were deposited electrochemically onto transparent conducting glass plates coated with indium-tin-oxide (ITO), i.e. indium oxide doped with tin ($In_2O_3(Sn)$), whereas solid state ECWs were then constructed by applying the solid state polymer electrolyte poly(2-acrylamido-2-methyl-propane-sulphonic acid) (PAMPS) as an ionic conductor, see Fig.1 for a schematic drawing of the two ECWs presented here (denoted as ECW1 and ECW3).
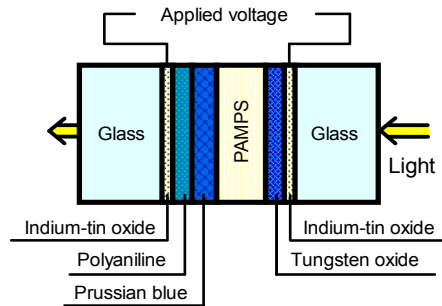

Figure 1. Schematic drawing of the ECW configuration used for ECW1 and ECW3 based on the ECMs polyaniline (PANI), prussian blue (PB) and tungsten oxide (WO_3).

Furthermore, for the spectroscopical measurements, a Cary 5 UV-VIS-NIR spectrophotometer, with an absolute reflectance accessory (Strong-type, VW principle), was used to measure the transmittance and reflectance of the ECWs, whereas emissivity measurements were performed with a SOC-100 HDR Hemispherical Directional Reflectometer from Surface Optics Corporation connected to a Thermo Nicolet 8700 Fourier transform infrared (FTIR) Spectrometer.

Results and Discussion

Measured transmittance spectra for two different ECWs at various applied electrical potentials (voltages) are given in Fig.2, with corresponding calculated solar radiation glazing factors and factor modulations in Table 1 and Table 2, respectively.

As to show an example how to calculate the solar radiation glazing factors, the solar transmittance (T_{sol}) is given by the following expression [9]:

$$T_{sol} = \frac{\sum_{\lambda=300nm}^{2500nm} T(\lambda)S_\lambda \Delta\lambda}{\sum_{\lambda=300nm}^{2500nm} S_\lambda \Delta\lambda} \tag{1}$$

where S_λ is the relative spectral distribution of solar radiation, $T(\lambda)$ is the spectral transmittance of the glass, λ is the wavelength, $\Delta\lambda$ is the wavelength interval, and the $S_\lambda\Delta\lambda$ values at different wavelengths are given as tabulated values [10,18]. The T_{sol} value will thus be a number between 0 and 1 (or 0 and 100 %), calculated in the main part of the solar spectrum, i.e. 300-2500 nm. A low number indicates a low transmission of solar radiation, whereas a high number represents a high solar radiation transmission. Note that the whole solar spectrum is not covered in the (standard) calculation of T_{sol}, and in future versions the wavelength range may favourably be extended to cover an even larger part of the solar radiation, e.g. from 290 nm to 3000 nm. In similar ways the other solar radiation glazing factors may be calculated, except the ε, SF and CRF values which follow other calculation procedures [10,18]. The ECW modulation level given in Table 2 is calculated by subtracting the solar radiation glazing factors for the same ECW at the high and low potentials given in Table 1, e.g. as for ΔT_{sol}:

$$\Delta T_{sol} = T_{sol}(\text{bleached}) - T_{sol}(\text{coloured}) \tag{2}$$

where the T_{sol} values in Table 1 are calculated from Eq.1 and likewise for the other solar radiation glazing factors.

From Table 1 it is observed that various solar radiation glazing factors may obtain both high and low values depending upon the applied electrical potential in the ECWs, e.g. changing the T_{vis} value from 0.78 to 0.17 for the ECW1 device and from 0.69 to 0.09 for the darker ECW3 device. It is also noted that these ECWs contain solar radiation absorbing electrochromic materials, i.e. not reflecting materials, as the changes with applied potential occur in the transmittance (e.g. T_{sol}) and absorbance (e.g. A_{sol}) values, and not in the reflectance (e.g. R_{sol}) values. As expected, the highest colouration level gives the largest SMPF values, i.e. the best protection of materials is achieved with the darkest ECW, e.g.

compare a SMPF value of 0.71 for ECW1 and 0.83 for ECW3 in the coloured state, with 0.43 (ECW1) and 0.59 (ECW3) in the transparent (bleached) state, respectively. The CRF values are very high, i.e. a very good colour rendering, for both ECW configurations in the transparent (bleached) state, with CRF values ranging from 0.96 to 0.99. However, in the coloured state, the CRF values are substantially reduced for both ECWs. ECW1 has CRF = 0.68 and ECW3 has CRF = 0.59 in the coloured state.
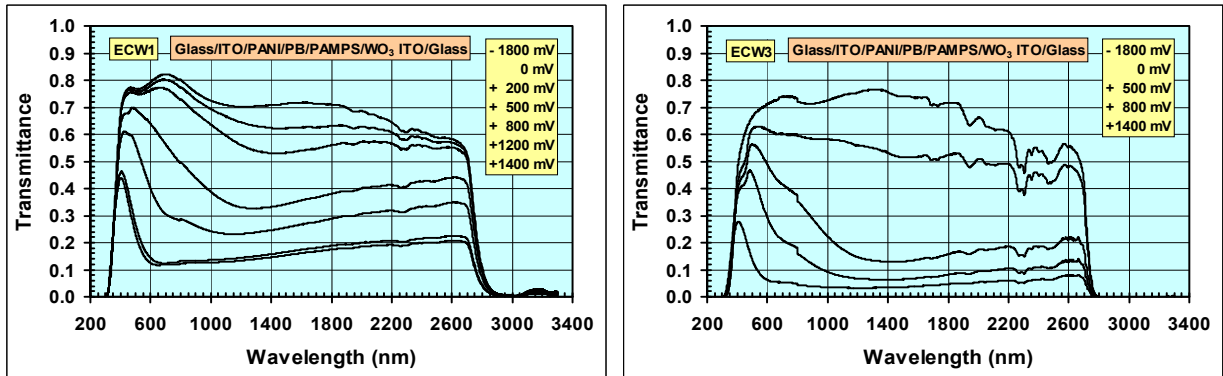

Figure 2. Transmittance versus wavelength in the whole solar spectrum measured for two different ECWs at various applied potentials [10,21,23]. Highest colouration level is at +1400 mV.

Table 1. Calculated solar radiation glazing factors for two different ECWs at various colouration levels (with transparent and dark coloured as the extremes), i.e. at various applied potentials (e.g. Eq.1). Corresponding transmittance spectra are given in Figure 2.

Glass Configuration	n	T_{uv}	T_{vis}	T_{sol}	SMPF	SSPF	$R_{vis,ext}$	$R_{vis,int}$	R_{sol}	A_{sol}	ε	SF	CRF
ECW1 (-1800 mV)	1	0.23	0.78	0.74	0.43	0.93	0.09	0.09	0.08	0.18	0.836	0.79	0.98
ECW1 (0 mV)	1	0.23	0.77	0.72	0.43	0.93	0.09	0.09	0.08	0.21	0.836	0.77	0.98
ECW1 (+200 mV)	1	0.24	0.75	0.68	0.44	0.93	0.09	0.09	0.08	0.24	0.836	0.74	0.99
ECW1 (+500 mV)	1	0.25	0.66	0.52	0.48	0.93	0.09	0.09	0.08	0.40	0.836	0.62	0.95
ECW1 (+800 mV)	1	0.26	0.47	0.36	0.54	0.92	0.09	0.09	0.08	0.56	0.836	0.51	0.82
ECW1 (+1200 mV)	1	0.24	0.19	0.19	0.68	0.93	0.09	0.09	0.08	0.73	0.836	0.38	0.68
ECW1 (+1400 mV)	1	0.23	0.17	0.17	0.71	0.93	0.09	0.09	0.08	0.75	0.836	0.37	0.68
ECW3 (-1800 mV)	1	0.08	0.69	0.67	0.59	0.97	0.09	0.09	0.08	0.25	0.836	0.74	0.96
ECW3 (+1400 mV)	1	0.12	0.09	0.08	0.83	0.97	0.09	0.09	0.08	0.84	0.836	0.30	0.59

Table 2. Calculated solar radiation glazing factor modulations for two different ECWs. The modulation level is calculated by subtracting the solar radiation glazing factors for the same ECW at the high and low potentials given in Table 1 (e.g. Eq.2).

Glass Configuration	n	ΔT_{uv}	ΔT_{vis}	ΔT_{sol}	ΔSMPF	ΔSSPF	$\Delta R_{vis,ext}$	$\Delta R_{vis,int}$	ΔR_{sol}	ΔA_{sol}	ε	ΔSF	ΔCRF
ECW1 (-1800 mV)	1	0.00	0.61	0.57	-0.28	0.00	0.00	0.00	0.00	-0.57	-	0.42	0.30
ECW1 (+1400 mV)													
ECW3 (-1800 mV)	1	-0.04	0.60	0.59	-0.24	0.00	0.00	0.00	0.00	-0.59	-	0.44	0.37
ECW3 (+1400 mV)													

The ECW1 and ECW3 devices have rather large solar radiation modulation abilities, e.g. $\Delta T_{vis} = 0.61$ and $\Delta T_{sol} = 0.57$ for ECW1, and $\Delta T_{vis} = 0.60$ and $\Delta T_{sol} = 0.59$ for ECW3, where the transmittance modulation is assumed to be due to absorbance regulation, i.e. $\Delta A_{sol} = -0.57$ for ECW1 and $\Delta A_{sol} = -0.59$ for ECW3. Note that reflectance values of the ECWs have not been measured, but as the (absorbing) electrochromic coatings are located between two glass plates, the (low) reflectance values will be close to the values for float glass, and these are hence employed in the current calculations. Although the solar factor modulations are lower than their solar transmission counterparts for the ECWs, the solar factor modulations are still quite high, i.e. ΔSF = 0.42 for ECW1 and ΔSF = 0.44 for ECW3. Thus, these ECWs are able to regulate large parts of the solar radiation, and their regulation may be readily characterized by the solar radiation glazing factors. Applying the ECWs into two-layer and three-layer window pane configurations reduces the total solar energy throughput modulation in the windows, which may also be seen in the ΔT_{sol} and ΔSF values, as several layers of glass and coatings will increase the total reflectance and absorbance (not depicted here, for examples it is referred to the work by Jelle [10]), i.e. less solar radiation left for the ECWs to modulate (regulate). That is, the solar radiation

modulation by an ECW will decrease with the number of glass panes and low emittance coatings added to the total window configuration.

Conclusions

Electrochromic windows (ECW) may dynamically control daylight and solar energy in buildings. This control may be readily characterized by solar radiation glazing factors, i.e. ultraviolet solar transmittance (T_{uv}), visible solar transmittance (T_{vis}), solar transmittance (T_{sol}), solar material protection factor (SMPF), solar skin protection factor (SSPF), external visible solar reflectance ($R_{vis,ext}$), internal visible solar reflectance ($R_{vis,int}$), solar reflectance (R_{sol}), solar absorbance (A_{sol}), emissivity (ε), solar factor (SF) and colour rendering factor (CRF). Two ECWs have been presented, demonstrating a large solar radiation modulation.

Acknowledgements

References

1. B.P. Jelle, G. Hagen and S. Nødland, "Transmission spectra of an electrochromic window consisting of polyaniline, prussian blue and tungsten oxide", *Electrochimica Acta*, **38**, 1497-1500, 1993.
2. B.P. Jelle, G. Hagen, S.M. Hesjevik and R. Ødegård, "Reduction factor for polyaniline films on ITO from cyclic voltammetry and visible absorption spectra", *Electrochimica Acta*, **38**, 1643-1647, 1993.
3. C.G. Granqvist, "Handbook of inorganic electrochromic materials", Elsevier, Amsterdam, 1995.
4. P.M.S. Monk, R.J. Mortimer and D.R. Rosseinsky, "Electrochromism: Fundamentals and applications", VCH, 1995.
5. B.P. Jelle and G. Hagen, "Electrochemical multilayer deposition of polyaniline and prussian blue and their application in solid state electrochromic windows", *Journal of Applied Electrochemistry*, **28**, 1061-1065, 1998.
6. B.P. Jelle and G. Hagen, "Correlation between light absorption and electric charge in solid state electrochromic windows", *Journal of Applied Electrochemistry*, **29**, 1103-1110, 1999.
7. R.J. Mortimer, "Organic electrochromic materials", *Electrochimica Acta*, **44**, 2971-2981, 1999.
8. R. Baetens, B.P. Jelle and A. Gustavsen, "Properties, requirements and possibilities of smart windows for dynamic daylight and solar energy control in buildings: A state-of-the-art review", *Solar Energy Materials and Solar Cells*, **94**, 87-105, 2010.
9. B.P. Jelle, A. Hynd, A. Gustavsen, D. Arasteh, H. Goudey and R. Hart, "Fenestration of today and tomorrow: A state-of-the-art review and future research opportunities", *Solar Energy Materials and Solar Cells*, **96**, 1-28, 2012.
10. B.P. Jelle, "Solar radiation glazing factors for window panes, glass structures and electrochromic windows in buildings - Measurement and calculation", *Solar Energy Materials and Solar Cells*, **116**, 291-323, 2013.
11. S.K. Deb, S.-H. Lee, C.E. Tracy, J.R. Pitts, B.A. Gregg and H.M. Branz, "Stand-alone photovoltaic-powered electrochromic smart window", *Electrochimica Acta*, **46**, 2125-2130, 2001.
12. C.M. Lampert, "Large-area smart glass and integrated photovoltaics", *Solar Energy Materials and Solar Cells*, **76**, 489-499, 2003.
13. B.P. Jelle, C. Breivik and H.D. Røkenes, "Building integrated photovoltaic products: A state-of-the-art review and future research opportunities", *Solar Energy Materials and Solar Cells*, **100**, 69-96, 2012.
14. K. Midtdal and B.P. Jelle, "Self-cleaning glazing products: A state-of-the-art review and future research pathways", *Solar Energy Materials and Solar Cells*, **109**, 126-141, 2013.
15. B.P. Jelle, "The challenge of removing snow downfall on photovoltaic solar cell roofs in order to maximize solar energy efficiency - Research opportunities for the future", *Energy and Buildings*, **67**, 334-351, 2013.
16. B.P. Jelle, "Accelerated climate ageing of building materials, components and structures in the laboratory", *Journal of Materials Science*, **47**, 6475-6496, 2012.
17. B.P. Jelle, E. Sveipe, E. Wegger, A. Gustavsen, S. Grynning, J.V. Thue, B. Time and K.R. Lisø, "Robustness classification of materials, assemblies and buildings", *Journal of Building Physics*, **37**, 213-245, 2014.
18. ISO 9050:2003(E), "Glass in building - Determination of light transmittance, solar direct transmittance, total solar energy transmittance, ultraviolet transmittance and related glazing factors", 2003.
19. B.P. Jelle, A. Gustavsen, T.-N. Nilsen and T. Jacobsen, "Solar material protection factor (SMPF) and solar skin protection factor (SSPF) for window panes and other glass structures in buildings", *Solar Energy Materials and Solar Cells*, **91**, 342-354, 2007.
20. B.P. Jelle and G. Hagen, "Transmission spectra of an electrochromic window based on polyaniline, prussian blue and tungsten oxide", *Journal of Electrochemical Society*, **140**, 3560-3564, 1993.
21. B.P. Jelle and G. Hagen, "Solar modulation in an electrochromic window using polyaniline, prussian blue and tungsten oxide", in *Electrochromic Materials II*, (PV 94-2), K. C. Ho and D. A. MacArthur (eds.), pp. 324-338, *Proceedings of the Symposium on Electrochromic Materials, The 184th Meeting of The Electrochemical Society*, New Orleans, Louisiana, U.S.A., 10-15 October, 1993, The Electrochemical Society, Pennington, NJ, 1994.
22. B.P. Jelle and G. Hagen, "Performance of an electrochromic window based on polyaniline, prussian blue and tungsten oxide", *Solar Energy Materials and Solar Cells*, **58**, 277-286, 1999.
23. B.P. Jelle, G. Hagen and Ø. Birketveit, "Transmission properties for individual electrochromic layers in solid state devices based on polyaniline, prussian blue and tungsten oxide", *Journal of Applied Electrochemistry*, **28**, 483-489, 1998.

Molecular Simulations of Anti-stain Polymeric Coatings

Y. Singhvi,[1] I. V. N. Tejasvini,[1] G. Manik[1,*]

[1]Department of Polymer and Process Engineering, IIT Roorkee (Saharanpur Campus), Saharanpur, India

Abstract: There has been an immense interest in the development of anti-stain polymeric coatings in the past (Fong *et al*., 2012 and Robert *et al*., 1999). Polyvinyl acetate (PVA) based coatings find extensive use in various coating and paints industries globally. Blending and co-polymerization of PVA with oleophobic polymers/monomers has resulted in potential coating formulations that possess enhance stain-resistance. In this work, we employ molecular simulations to understand the effect of blending of some selective fluoropolymers with PVA on the oleophobic behaviour of formulated coatings. Material Studio™ software available from Accelrys® has been employed for running Molecular Dynamics (MD) simulations to describe polymer coatings behavior under stain-like conditions (using a decane molecule). Simulation results have been quantified in terms of movement of oil-representative molecules away from the formulated coatings surface, and clearly demonstrate the effect of selective fluorine based blends with PVA matrix. To confirm accuracy of the simulation protocol, the simulated density of coatings is found to confirm to experimentally derived values. Results demonstrate that with increasing fluoro content the oleophobic behaviour is improved as found by increased msd values.

Keywords: oleophobic, anti-stain, molecular simulations, coatings

Introduction

Many advancement in coatings formulation synthesis have given rise to HFPO, Teflon, PVDF and other modified molecules, that are significantly oleophobic to be used as industrially useful stain-repellent coating materials. Recently, Dalvi *et al.* have used atomistic MD to explain the underlying reasons of hydrophobicity, and hence oleophobicity. Recently, Nguyen *et al*., 2014 have synthesized superhydrophobic coatings that also provide superoleophobicity, by optimizing on the coating surface roughness and chemistry. Cansoy *et al*., (2014) have employed decane, octane, tetradecane and hexadecane to understand the oleophobicity of perfluoro alkyl based coatings. Hence, in this work we employ a decane molecule to represent oil-like

*Communicating Author: Dr. Gaurav Manik
Email Address: manikfpt@iitr.ac.in

behavior and quantify it through the mean squared displacement (msd) of stain molecule against different simulated coatings.

Molecular Simulation Strategy

Material Studio™ software available from Accelrys® Inc., has been employed for running MD to compare coating's performance properties, and propose a potential optimized anti-stain formulation. The Amorphous Cell and Forcite modules have been used in this work-

- Simulation cells are constructed containing pure polymeric systems (PVA, PVF, PVDF, etc) and their blends/copolymers of varied compositions with PVA as base matrix. A total of 10 chains of homopolymers or blends are packed into simulation cells and the composition of oleophobic polymers (PVF, PVDF, etc) is varied from 0-100%.

- NPT MD is run for a simulation time of about 300-500ps to stabilize the density. COMPASS force field was employed to compute the intermolecular and intramolecular interactions. The intermolecular interactions are computed upto a distance of $12A^o$.

- A layer of polymeric coating material is then constructed, with decane separated from this coating surface by $\sim 10A^O$. The decane molecule, is used to imitiate oil-like material or fumes that emerge from exhausts of 2,4-wheelers in form of unburnt hydrocarbons.

- The entire set of polymer chains in the coating are then frozen from moving, while MD simulations are applied on the decane molecule. The movement of decane molecule is then quantified through its *msd* from the coating for 100-120ps.

Results and Discussion

The accuracy of the simulation protocol is confirmed by obtaining the simulated density of coatings post-NPT MD, and comparing it with the experimentally derived values for PVF-PVA system (Table 1), and also to values obtained from group contribution theory (Synthia module of Material Studio™). The results clearly indicate that the simulated values are closer to experimental values and also values derived from group contribution theory.

Table 1. Results of MD simulated densities compared with experimental density and group contribution obtained density for PVF-PVA system.

Composition PVF in PVA (mol%)	Simulated Density (g/cc)		
	MD	Group Contribution	Experimental
0.0	1.203	1.218	PVA, 1.192-1.312
20.0	1.279	1.278	-
50.0	1.378	1.378	-
100.0	1.511	1.529	PVF, 1.5-1.916

Formulated coatings of some of such compounds have been simulated and oleophobic properties quantified in terms of msd of decane molecule, compared for varying compostion of PVDF (0%, 20%, 50% and 100%) in the formulated coating. Fig. 1(a) and (b) show that the decane molecule moves very close to the PVA based coating, whereas in Fig. 1(c) and (d) the decane molecule is visually seen to have moved quite away from the pure PVF based coating surface, when compared at $t = 120ps$ simulation times.

(a) PVA(t = 0s)   **(b) PVA(t = 120ps)**

(c) PVF(t = 0 ps)   **(d) PVF(t = 120ps)**
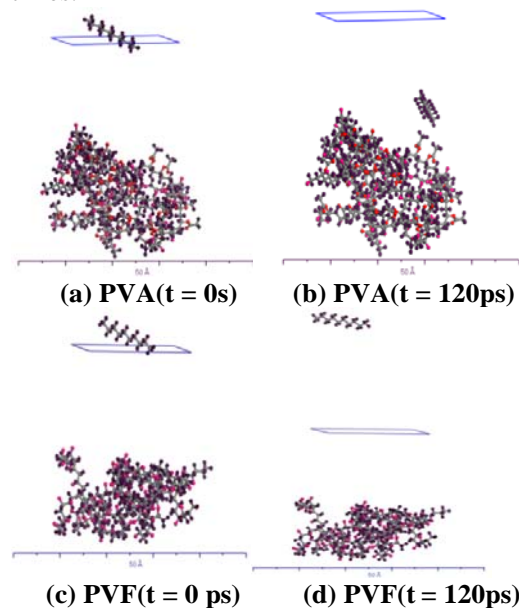
Figure 1: Illustration of behavior of a decane molecule against pure PVA coating (a & b) compared with pure PVF coating (c & d) at $t = 0ps$ and 120ps simulation times.

Results presented Fig. 2 clearly demonstrate that with increasing fluoropolymer (PVDF) content the oleophobic behaviour is improved as found by increased msd values.
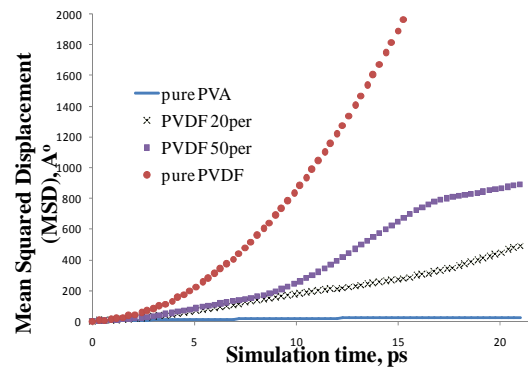
Figure 2: Illustration of mean squared displacement of decane molecule against a coating with varied PVDF compositions (0%, 20%, 50% and 100%) with simulation times.

Conclusions

This paper demonstrates use of MD as a potential tool in determing the performance of coating against hydrocarbons or stain-like molecules. The work establishes a procedure which can be used to screen potential different oleophobic formulations without the necessity of actually synthesizing the formulations, thereby, reducing the huge efforts and resources lost in synthesizing and characterizing the performance of such coatings, and finally screening them.

References

Cansoy, C. E., Cengiz, U. (2014), The effect of perfluoroalkyl and hydrocarbon liquid chain lengths on oleophobic behaviours of copolymer surfaces, *Colloids and Surfaces A: Physicochem. Eng. Aspects*, 441, 695-700.

Dalvi, H. And Rossky, P.J. (2010), "Molecular Origins of Fluorocarbon Hydrophobicity", *PNAS*, 107(31), 13603-13607.

Fong, B. C., Huang, T-L. J., Ko, J.H., Zhu, D-W., (2001), Patterned article having alternating hydrophilic and hydrophobic surface regions, Patent Number EP1084178A1.

Material studio™, by Dassault systems, UK (Accelrys®), http://accelrys.com/products/materials-studio/

Nguyen, T. P. N., Dufour, R., Thomy, V., Senez, V., Boukherroub, R., Coffinier, Y. (2014), Fabrication of superhydrophobic and highly oleophobic silicon based surfaces via electroless etching method, *Applied surface science*, 295, 38-43.

Robert, H. B., Perlman, D. (1999), Improved anti-graffiti coatings and method of graffiti removal, Patent Number EP0912260A1.

Study of Electrical Conductivity of Polypyridine-PVAc Composite Thin-Film doped with $Ni(NO_3)_2$

Gopal. R. Dhokane *

* Department of Physics, Arts, Science & Commerce College, Chikhaldara, Maharashtra 444807 (India)
E-mail:grdhokane@gmail.com, grdhokane_2007@india.com.

Abstract: Pyridine shows interesting properties due to hetroaromatic nature combined to its electron deficient nitrogen and molecular simplicity. Herein Ni doped Polypyridine-PVAc composite films were prepared by isothermal evaporation technique with varying concentration of 2,5-Dibromopyridine as well as oxidizing agent $Ni(NO_3)_2$. In XRD spectra sharp reflection peaks are observed at 2θ value of 26.46 and 29.78^0, and 26.51, and 29.81^0, corresponding to d-spacing of 3.36 and 3.00, and 3.36 and 2.99 A^0 respectively, may be due to the phases of polypyridine. The dc conductivity of polypyridine-PVAc composite films depends on temperature and increases with increase in temperature, indicating negative temperature coefficient (NTC) of resistance. This shows the semiconducting nature of the films. Ac electrical conductivity is measured for all prepared samples in the frequency range 100 Hz to 200 KHz. As frequency increases the ac electrical conductivity σ_{ac} increases linearly according to equation $\sigma_{ac} = A\ \omega^s$. The frequency exponent 's' was calculated for all the investigated samples and the frequency is found to have a pronounced effect on conductivity at relatively lower temperature.

Keywords: Composites; Conducting polymer; Polypyridine; XRD; Conductivity

1.Introduction

The basic property of a semiconductor is its electrical conductivity, which depends on the mobility and concentration of the charge carriers. In semiconductors, the electrical properties are sensitive to the impurity content and doping [1-2].

Several studies have been performed on the conjugated polymers such as polypyrrole, polyaniline, polythiophene and polyphenylene, since the discovery of the conducting properties of polypyrrole in 1979 [3]. These polymers are capable of exhibiting a significant level of electrical conductivity, hence termed as conducting polymers. Composites consisting of polymers with embedded metallic particles have unique properties and are of particular interest for optical, electrical, and opto-electronic applications [4-5].

Much research efforts have been generated to produce composites or blends of conducting polymer film with some insulating polymers in order to overcome the drawbacks such as poor processability and lack of essential mechanical properties exhibited by these polymers [6]. In this technique, a host of insulating polymers (namely, poly(styrenesulphonate), polycarbonate, poly(vinyl chloride), nitrile rubber, polyimide and poly(vinyl alcohol) have been combined with any conducting polymer (such as polypyrrole, polyaniline,

1

polythiophene) in an aqueous or organic medium to produce conducting polymer composites which will have the conducting properties of the conducting polymer [7-10].

Conductive polymers and their composites represent a potential for semiconductor technology. The mechanism of charge transfer between organic, inorganic, semiconductor and conductive polymer has been recently investigated by Halliday [11-13]. They suggested that polymer must have sufficiently low resistivity to minimize power dissipation. In spite of its molecular simplicity, pyridine shows interesting properties due to its hetroaromatic nature combined to its electron deficient nitrogen. It is well known that its nitrogen atom acts as a hydrogen bonding acceptor and it can be co-ordinate with metal cations and protoneted using strong acids. Pyridines are important molecules as they can be polymerized as conjugated chain like molecules. Due to their conjugation, polypyridines are luminant in the blue-green spectrum of visible light and are therefore of interest due to their photonic properties [14].

2. Materials and experimental methods:

Polyvinyl acetate (PVAc) (AR grade), 2,5-Dibromopyridine (Sigma Aldrich), Ni $(No_3)_2$, and Methanol used as a starting materials for the preparation of polypyridine-PVAc composite films.

2.1 Preparation of Polypyridine-PVAc composite films:

For the preparation of Ni doped composite films a mixed solution of PVAc and methanol (10:90) was prepared. In order to make the homogeneous solution the mixture is stirred for 3 to 4 hours and kept overnight. In prepared homogeneous solution 1 Mole Ni $(No_3)_2$ (0.5961 gm) was added and stirred about 60 minutes. Finally 2,5 dibromopyridine was added with different concentration. When 2,5 dibromopyridine was added to the solution of PVAc, methanol and Ni $(No_3)_2$, a dark green solution was obtained. The complete assembly was heated at constant temperature (water bath) to get homogeneous solution. Glass plates (30 x 30 Cm^2) thoroughly clean with water and then with acetone, were used as a substrate. To achieve perfect leveling and uniformity in the thickness of the films the glass plate was leveled by using sprit level. Now the homogeneous solution was poured on the glass plate to prepared films of the composites. The whole assembly was placed in a dust free chamber maintained at constant temperature. In this way the Ni doped Polypyridine-PVAc composite films were prepared by isothermal evaporation technique [15]. After evaporation of solvent the thin films were formed, which were then washed with distilled water to remove the excess of Ni $(No_3)_2$.

2.2 Thickness measurement:

2

The thickness of the films was measured by DIGIMATIC micrometer (Mitutoyo Corporation, Japan) having least count 0.001mm. Finally the electrical conductivity of all films was calculated by using the formula.

$$\sigma_{dc} = t/RA \tag{1}$$

Where, t is the thickness of the film, A is the area of the sample and R is the resistance of the film.

2.2 Dc conductivity measurement:

The dc electrical conductivity of all composite films was measured by using two probe method in the temperature range 313 to 358 K. The heating rate of the sample was 2°C/min and it was controlled by using DID oven. The potential applied to the sample was kept constant (5V) and temperature increases with the rate 2°C/min and corresponding current was observed with the help of Pico-ammeter.

2.3 Temperature and frequency dependence ac conductivity measurement

Ac electrical conductivity was measured in the temperature range 313 to 358 K by using digital LCR Q bridge 4230 (Wayhe Kerr, Uk) in the frequency range 100 Hz to 200 KHz.

3. Results and Discussion:

X-Ray Diffraction (X-RD)

The X-ray diffraction patterns of all Polypyridine-PVAc composite films are shown in figure 1. In the present work XRD technique has been used to investigate the amorphous or crystalline nature of the samples. X-ray diffraction pattern shows crystalline nature of the samples. The appearance of sharp peaks in diffractograms of all samples may indicate some degree of crystanality in the composites. The X-RD pattern of all samples reveals a sharp reflection peak at 2θ = 11.79^0 and d-value 7.52, this suggests the existence of intercalated water in the lamella of polypyridine corresponds to the plane (001) [16]. The sharp peaks occur in the X-ray diffraction patterns may be due the phases of polypyridine. The average crystallite size is estimated by using Scherrer's formula D=kλ/βcosθ .

Where D is the crystallite size of particle, λ = 1. 54 A^0 being the X-ray wave length of CuKα and k is the shape factor which can be assigned to a value of 0.89 if the sample is unknown, θ is diffraction angle at maximum intensity of peak and β is the full width at half maxima of angle of diffraction in radians.

3

The XRD spectrum of all sample shows that the sample is crystalline polymer. There are few medium peaks at angles 2θ = 13.29, 14.23, 15.45 and 18.21 indicates the presence of PVAc in the composites material. [17]

In XRD spectra of samples (SN$_5$ and SN$_7$) sharp reflection peaks are observed at 2θ value of 26.46 and 29.78^0, and 26.51, and 29.81^0, corresponding to d-spacing of 3.36 and 3.00, and 3.36 and 2.99 A^0 respectively, may be due to the phases of polypyridine and the corresponding planes are (200) and (020).

The reflectance peaks observed at 22.45, 33.65, 43.31 and 48.85^0 can be indexed as the hexagonal phase of Ni(OH)2 by comparison with the data of the JCPDS file No. 14-0117, which indicated that the crystalline state of the sample is typically (II)-type Ni(OH)2 phase. [18]
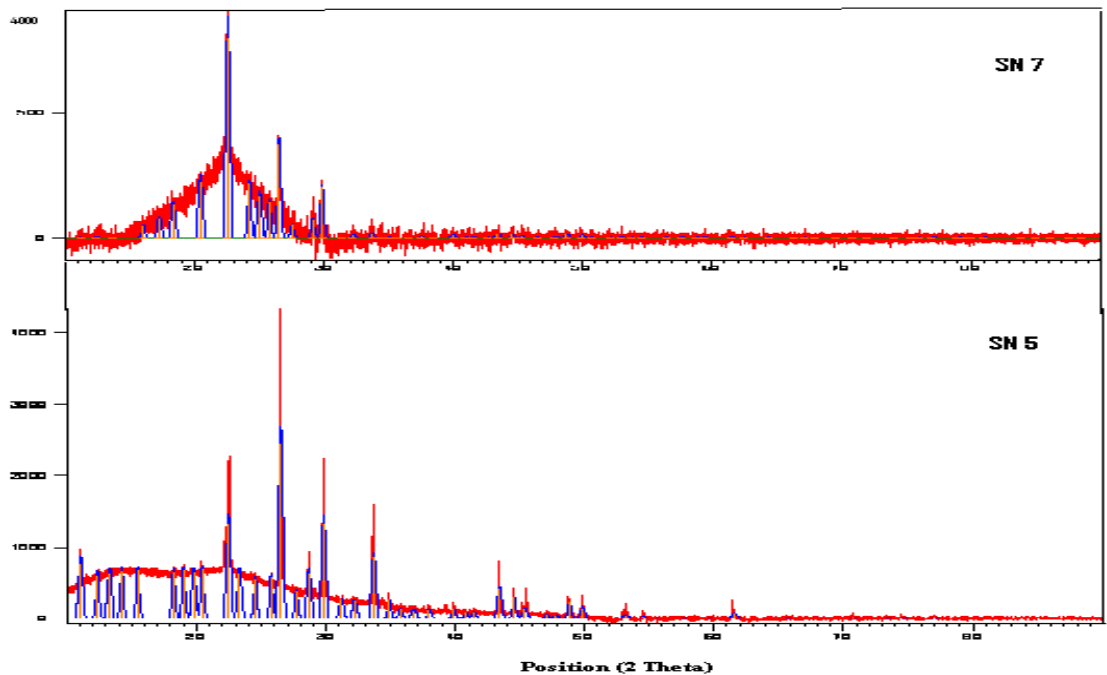

Figure 1: X-RD spectra for the *Polypyridine-PVAc composite films*

3.1 Temperature dependence dc conductivity

The present study focuses on temperature dependence of electrical conduction in doped polypyridine-PVAc composite films has been carried out to understand the role of dopant as

4

well oxidizing agent $Ni(No_3)_2$, when use in polymerization process with varying concentration of monomer 2, 5-dibromopyridine. The dc electrical conductivity of all samples was calculated in the temperature range 313 to 353 K by measuring the resistance of the sample. The observed dc electrical conductivity is as under.

S. No.	% of 2,5 Dibromopyridine	Dc conductivity (S/cm)
1	.05	1.660 x 10
2	0.1	1.210 x 10
3	0.2	3.7015 x 10
4	0.3	8.5015 x 10
5	0.5	4.2730 x 10
6	0.6	1.7268 x 10

Table 1: Variation of dc conductivity with wt % of 2,5-dibromopyridine at temperature 323 K.

Figure 2 shows variation of dc electrical conductivity with temperature ($\log\sigma_{dc}$ Vs 1000/T) for all samples in the temperature range 313 to 353 K. From conductivity plot it is observed that the dc conductivity of polypyridine-PVAc composite films depends on temperature. The dc electrical conductivity of these films increases with increase in temperature, indicating negative temperature coefficient (NTC) of resistance. This shows the semiconducting nature of the films. As the temperature increases the polymer become soft and the mobility of main chain segment as well as the rotation of side groups become easier. Thus, at higher temperature more and more dipoles are oriented resulting in the higher equivalent surface charge density. Dc conductivity follows Arrhenius equation [19-20].

$$\sigma = \sigma_0 \exp(-E_a/kT) \qquad (2)$$

Where σ_0 is the pre-exponential factor, E_a is activation energy and k the Boltzmann's constant. For the present composite films, these plot ($\log\sigma_{dc}$ Vs 1000/T) shows straight lines with negative slope indicating the temperature dependence of conductivity.

The values of activation energies have been calculated from Arrehenius plots using the equation (2).

At any temperature only a fraction of molecules or atoms in the system will have sufficient energy to reach activation energy level of E_a. As the temperature of the system is increased, more molecules or atoms will attain the activation energy level. At high temperature, the

5

activation energy of dipole segmental processes decreases due to disturbance of the cooperative movement of segments. This explains the decrease of activation energy with increase in temperature [21-22]. Figure 3 shows the variation of activation energy with concentration of monomer 2,5- dibromopyridine.
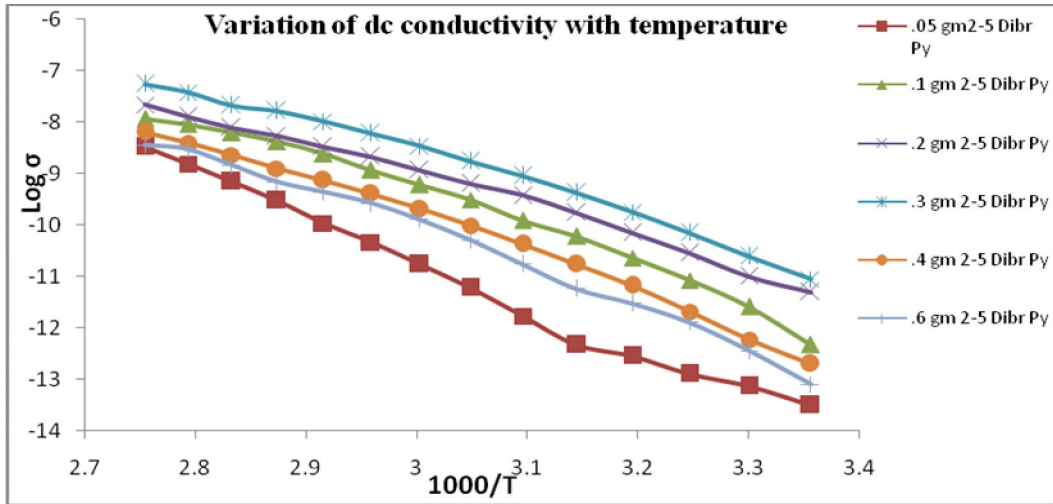

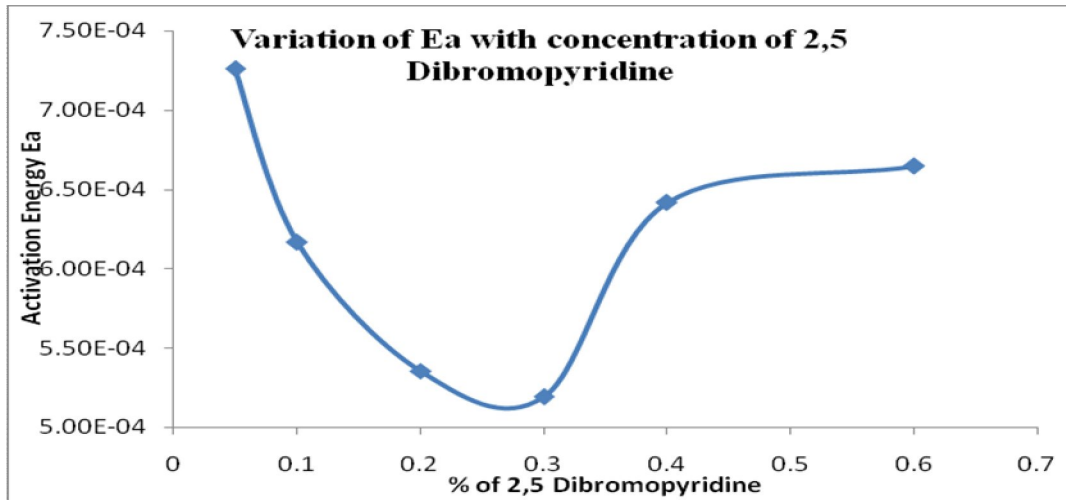Figure 2: Temperature dependence of dc electrical conductivity

Figure 3: Variation of activation energy with varying concentration of 2,5 – dobromopyridine.

3.2 Frequency dependence ac conductivity:

A common feature to all semiconductors is that ac electrical conductivity σ_{ac} increases with increasing frequency according to the equation [23].

6

$$\sigma_{ac} = \sigma_{tot} - \sigma_{dc} = A\,\omega^s \qquad (3)$$

Where ω is the angular frequency ($\omega = 2\pi f$), σ_{tot} is the total electrical conductivity, s is the frequency exponent (s<1) and A is the constant depends on temperature. In most cases the obtained value of s ranges from 0.7 to 1 at room temperature, and has a tendency to decrease with increasing temperature [24]. Therefore the correlated barrier hopping model (CBH) [25] has been extensively used to most semiconducting materials. The frequency exponent s is found to decrease with increasing temperature, as

$$s = 1 - \frac{6\,kT}{W_m + [kT \log \omega\tau_0]} \qquad (4)$$

This means that the obtained experimental results agree with the correlated barrier hopping model (CBH). Where W_m is the binding energy of the carriers in its localized site, which is assumed to be band gap and k, is the Boltzman constant.

According to the Austin-Mott formula [26], based on correlated barrier hopping (CHB) model, ac conductivity σ_{ac} can be explain in terms of the hopping of electrons between pairs of localized states at the Fermi level. The ac electrical conductivity σ_{ac} is related to the density of states N (E_f) at the Fermi level by

$$\sigma_{ac} = (\pi/3)\,[N\,(E_f)]^2\,kTe^2\,\alpha^{-5}\omega\,[\log\,(\upsilon_{ph}\,/\omega)]^4 \qquad (5)$$

Where α is the exponential decay parameter of the localized states wave function and υ_{ph} is the phonon frequency. N (E_f) is the energy density of the states near Fermi level.

The hopping distance R at frequency ω is given by

$$R = \frac{1}{2\alpha} \log\,(\upsilon_{ph}\,/\omega) \qquad (6)$$

In this quantum Mechanical Tunneling Model (QTM) 's' should be temperature independent but frequency dependent. The quantum mechanical tunneling of a carrier though the potential barrier between the sites separated by a distance R, demands that (i) ac conductivity σ_{ac} should be dependent on temperature and (ii) frequency exponent 's' should be frequency dependent.

The frequency dependent ac conductivity σ_{ac} was measured for investigated films. The plot of log (ω) against log ac conductivity (log σ_{ac}) at different temperatures (313, 323, 333, 343, and 353 K) in the frequency range 0.1 to 200 KH_z shown in figure 4. From figures it is clear that

7

the ac conductivity σ_{ac} increases linearly with increasing frequency according to equation $\sigma_{ac} = A \omega^s$
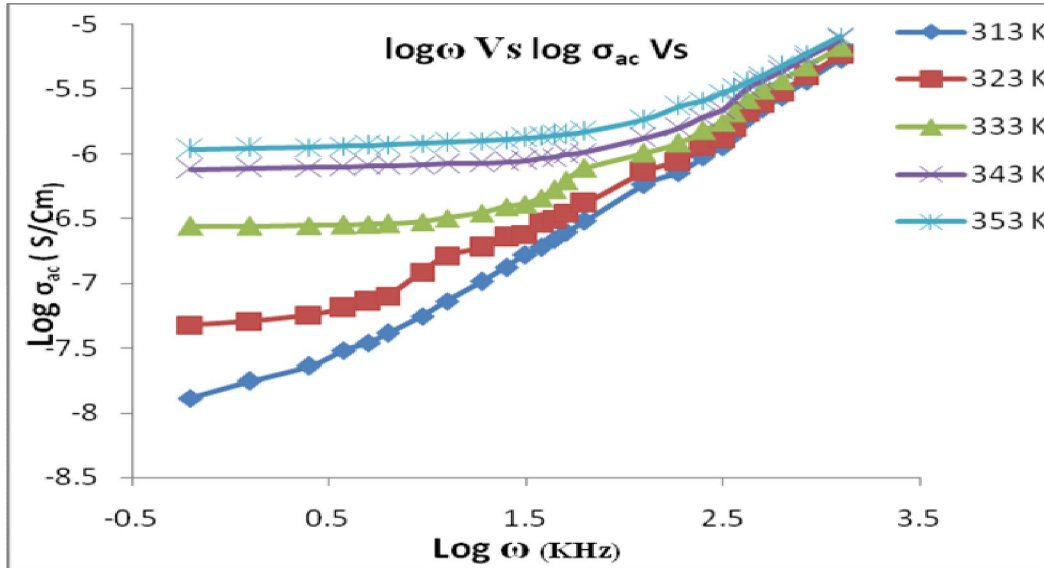

Figure 4: Frequency dependence of ac conductivity of optimized
sample of series I Ni(No₃)₂

3.3 Temperature dependence ac conductivity:

The temperature dependence ac conductivity σ_{ac} of Polypyridine-PVAc composite films were measured in the temperature range 313 – 353 K at different fixed frequencies (0.1, 1, 10, 100 and 200 KH$_Z$). The Plot of log of ac conductivity (logσ_{ac}) against reciprocal of temperature (1000/T) at different fixed frequencies of optimized sample shown in figure 5.

The obtained relation from the plot of logσ_{ac} against 1000/T indicates that ac conductivity σ_{ac} is independent of temperature at higher frequencies and increases linearly with the reciprocal of temperature (1/T) at lower frequencies. This suggested that the ac conductivity is a thermally activated process from different localized stated in the gap or its tails. Thus, the application of an Arrhenius type relation is used to describe the temperature dependence of ac conductivity as

$$\sigma_{ac} \;=\; \sigma_0 \exp. \, (-\Delta E_{ac} / kT) \qquad\qquad (7)$$

Where ΔE_{ac} is the activation energy and σ_0 is the pre-exponential factor. The activation energy of conduction is calculated at different frequencies from the slope of straight lines

8

using equation (7). For all investigated films it is observed that E_{ac} decreases with increase of frequency [27]. The increases in the applied field frequency enhance the electronic jump between the localized states, consequently the activation energy ΔE_{ac} decreases with increasing frequency. The smaller values of ac activation energy as compared with that of dc activation energy and the increases of ac conductivity with increase of frequency confirm that hopping conduction to be the dominant mechanism [28-31].
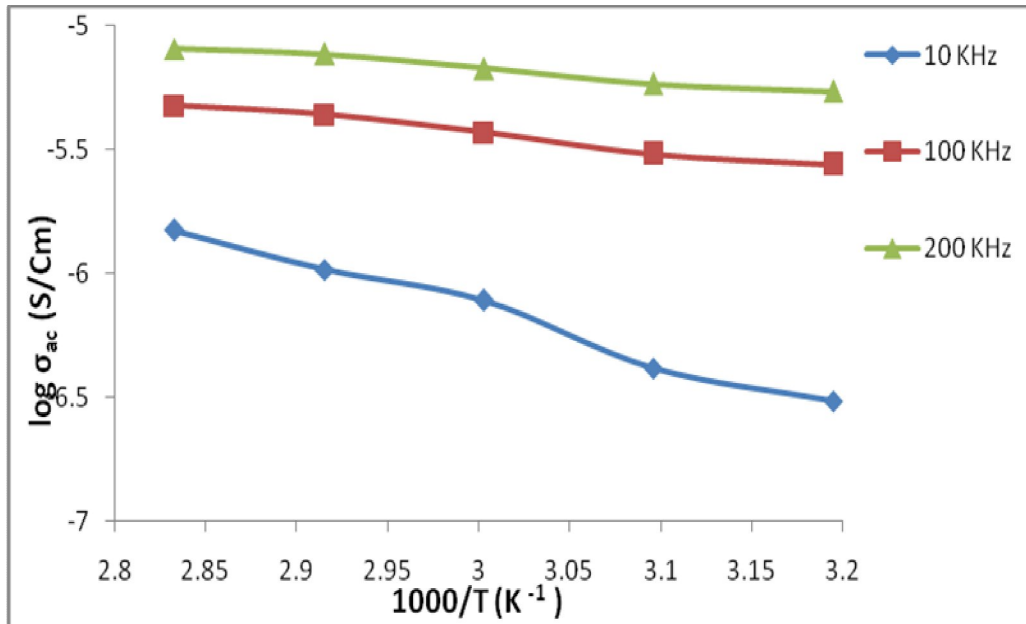

Figure 5: Temperature dependence of ac conductivity at different fixed
frequency of optimized sample of series I Ni(No$_3$)$_2$

Conclusions:

The chemical method is a simple and low cost method for synthesis of polypyridine-polyvinyl acetate (PPy-PVAc) composite films. Characteristics study of polypyridine-PVAc composite films has been made by analyzing the films with XRD. The XRD spectrum of all sample shows that the sample is crystalline polymer. There are few medium peaks at angles $2\theta = 13.29, 14.23, 15.45$ and 18.21 indicates the presence of PVAc in the composites material. In XRD spectra sharp reflection peaks are observed at 2θ value of 26.46 and $29.78^{0,}$ and 26.51, and 29.81^{0}, corresponding to d-spacing of 3.36 and 3.00, and 3.36 and 2.99 A^{0} respectively, may be due to the phases of polypyridine and the corresponding planes are (200) and (020). The reflectance peaks observed at $22.45, 33.65, 43.31$ and 48.85^{0} can be indexed as the hexagonal phase of Ni(OH)2 by comparison with the data of the JCPDS file

9

No. 14-0117, which indicated that the crystalline state of the sample is typically (II)-type Ni(OH)2 phase.

The dc electrical conductivity of these films increases with increase in temperature, indicating negative temperature coefficient (NTC) of resistance. This shows the semiconducting nature of the films. As the temperature increases the polymer become soft and the mobility of main chain segment as well as the rotation of side groups become easier. Thus, at higher temperature more and more dipoles are oriented resulting in the higher equivalent surface charge density. Dc conductivity follows Arrhenius equation $\sigma = \sigma_0 \exp(-E_a/kT)$. For the present composite films, the plots ($\log \sigma_{dc}$ Vs 1000/T) shows straight lines with negative slope indicating the temperature dependence of conductivity and the values of activation energies have been calculated from Arrehenius plots using the equation. This explains the decrease of activation energy with increase in temperature.

The frequency dependent ac conductivity σ_{ac} was measured for investigated films at different temperatures in the frequency range 0.1 to 200 KH$_z$. The ac conductivity σ_{ac} increases linearly with increasing frequency according to equation $\sigma_{ac} = A \omega^s$. The ac conductivity σ_{ac} is independent of temperature at higher frequencies and increases linearly with the reciprocal of temperature (1/T) at lower frequencies. This suggested that the ac conductivity is a thermally activated process from different localized states in the gap or its tails. Thus, the application of an Arrhenius type relation is used to describe the temperature dependence of ac conductivity. The smaller values of ac activation energy as compared with that of dc activation energy and the increases of ac conductivity with increase of frequency confirm that hopping conduction to be the dominant mechanism.

References:
1. B.G. Streetman, Solid State Electronic Devices, Prentice-Hall, Englewood, Cliffs, (1 980)
2**.** F**.** Gutman and L.E. Lyons, Organic Semiconductors, **A.** Krieger, Malabar, (1981)
3. Diaz A F, Kanazawa K K and Gardini G P (1979) Electrochemical polymerization of pyrrole. *J Chem Soc Chem Commun* 635-6.
4. U. Kreibig, M. Vollmer, Optical properties of metal clusters, Springer-Verlag, Berlin ; New York, 1995.
5. A. Biswas, H. Eilers, F. Hidden, O.C. Aktas, C.V.S. Kiran, Applied Physics Letters 88 (2006) 013103.
6. Niwa O and Tamamura T (1984) Electrochemical polymerization of pyrrole on polymer– coated electrodes. *J Chem Soc Chem Commun* 470, 817.
7. Otero T F and Sansinena J M (1996) Influence of synthesis conditions on polypyrrole- poly(styrenesulphonate) composite electroactivity. *J Electroanal Chem* 412, 109-16.
8. Wang H L, Toppare L and Fernandez J E (1990) Conducting polymer blends: polythiophene and polypyrrole blends with polystyrene and poly(bisphenol A carbonate)

10

Macromolecules 23, 1053-9.

9. De Paoli M A, Waltman R J, Diaz A F and Bargon J (1985) An electrically conductive plastic composite derived from polypyrrole and poly(vinyl chloride). *J Polym Sci Polym Chem Ed* 23, 1687-97.

10. Naoi K and Osaka T (1987) Highly enhanced anion dopingundoping process at the polypyrrole electrode of regulated morphology prepared with the aid of insulating NBR film. *J Electrochem Soc Electrochem Sci Tech* 134, 2479-83.

11. D. A. Halliday and E.R. Holland, *Thin Solid Films*, **276** (1994).

12. F. W. Harris, "Introduction to Polymer Chemistry,"J. Chem. Educ, **58** (1981) 837

13. R. B. Seymour, Conductive polymer, *Polymer Science and Technology*, New York, (1991).

14. Matti Knaapila, Mika Torkkeli and Tapio Makela, *Mat. Res. Soc.Symp. Proc.* **660** (2001) 1-6.

15. R. Bahri and B. R. Sood, *Thin Solid Films*, **100** (1983) 15

16. Pinggui Liu, Kecheng Hong, Peng Xiao and Min Xiao, *J. Mat. Chem.* **10** (2000) 933-935.

17. B. D. Cullity, *Elements of X-ray diffraction, Addison-Wesely co. Inc., London* (1978).

18. *X. Liu, L. Yu / Journal of Power Sources 128 (2004) 326–330].*

19. S. Selvasekarapandian and Vijaykumar, *Solid State Ionics*, **148** (2002)329.

20. R. V. Waghamare, N. G. Belasare, F. C. Raghuwanshi, S. N. Shilskar, *Bull. Matter. Sci.* **30 (2)** (2007) 167-172.

21. H. C. Shinha and A. P. Shriwastav, *Indian J. Pure and Appl. Phys.* **17** (1979) 726.

22. A. R. Tiwari, K. K. Saraf and A. P. Shriwastav, R. Nath, *Electrical and Optical Behavior of Solids*, **187.**

23. N. F. Mott and E. A. Davis, *Electronics Process in Non-Cryst. Materials, Clarendon Press, Oxford,* (1971) 211.

24. S. S. Fouad, A. E. Bekheet and A. Elfalaky, Eru. *Phys. Stat. Sol.* **(b), 210,** (1997) 449.

25. M. A. Afifi, A. E. Sayam, A. E. Bekheet and A. Elfalaky, *Eru. Phys.J. Appl.* **16,** (2001) 1999.

26. L. G. Austin, N. F. Mott, *Adv. Phys.* **18** (1969) 41.

27. N. A. Hegab, A. E. Bekheet, M. A. Afifi and H. A. Shehata, *Jou. Ovo. Research,* **3 (4)** (2007) 71-82.

28. N. A. Hegab, H. E. Atyia, *Jou. Ovo. Research*, **3 (5)** (2007) 93-102.

29. A. R. Long, *Adv. Phys.* **31** (1982) 553.

30. P. Nermec, M. Frumar, B. Frumarova, M. Jelinek, J. Lancok, *J. Jedelsky, Opt. At.* **15** (2000) 191.

31. A. Zolanvari, N. goyal, S. K. Tripathi, Pramana *J. of Phys.* **63 (3)** (2004) 617-625.

A Smart Material for Imaging Highway Substructure Damage

Kurt Rudahl, M.S.* and Sally E. Goldin, Ph.D.
Department of Computer Engineering
King Mongkut's University of Technology Thonburi
* ktr@goldin-rudahl.com

Abstract: Roads, highways, airport runways, railways, and levees (dikes) all consist of carefully designed and built layers which ultimately rest on an earthen subbase. Over time, erosion, nearby construction, weather, seismic activity, and other causes can weaken or create gaps in the subbase. Initially there is no sign of this on the surface, until a collapse suddenly occurs. This collapse entails expenses for immediate repair, and direct and indirect costs to the surrounding communities due to disruption of transport and damage to buildings. In some cases there can be environmental damage or human casualties.

At present there is no practical way to monitor the condition of the earthen subbase. Surveys are periodically made on important roads to detect pavement distress, and railway staff are continually monitoring the state of the railway track. However, subsurface degradation or cavities which form in the subbase are not detectable from visible pavement distress. Furthermore, existing techniques such as ground-penetrating radar, which allow indirect examination of the highway structural condition, are not appropriate for routine, repeated use.

In this paper we describe a "smart" material (patent applied for) that addresses this problem. This material can be embedded into roads and highways during construction or reconstruction. Subsequently, an easy-to-use and inexpensive sensor array can be used to verify the integrity of the highway subbase. We describe the theory and design of the material and sensor array, and the computer processing used to create the subsurface images. We then describe a simple setup for testing the material in a laboratory, and present the positive results of this testing. We also describe plans for further stages of testing, which will require incorporating the material into large-scale highway construction followed by a multi-year testing program.

Keywords: highway testing, road collapse, subsurface imaging, smart material

Background

Roads and highways form a major part of any nation's infrastructure, and their construction and maintenance are a major part of the nation's budget. They are used every day by almost everyone, and are the backbone of transportation for commercial goods. Airport runways, likewise, are crucial to a nation's economy. In this paper we will refer to roads, highways, airport runways, railway tracks, and river or ocean levees and dikes collectively as "roads".

The structure of modern roads has evolved gradually since the 17th century into a complex set of layers, whose details vary depending on the materials available, the environment, and the intended use. Well-known engineering principles provide a high level of confidence in the properties and stability of these structures.

However, all such constructions share a common weakness: they are not built with a rigid, self-supporting structure but depend for their support on the underlying ground. Despite the most careful design and the most exacting preparation, the ground behavior after the road has been completed is subject to forces and events which are known statistically but are unpredictable in detail. In particular, cavities and fractures in the underlying strata beneath the road can develop due to floods, gradual erosion, and other geological and hydrological forces. Leaks of fluids and foreign substances from landfills or hazardous waste dumps can also cause problems.

Subsidence of a railway track, which may not appear until it is put under load, can cause a train to come off the track, potentially resulting in serious injuries and great damage. A loss of strength in a dike can cause the dike to fail during a severe storm leading to property damage and possible loss of life.

The minimum implication of a failure such as shown in Figure 1 is a need for an expensive emergency repair, quite possibly during inclement weather since storms are a common cause of developing cavities or weaknesses in the subbase. In some cases, the collapse may cause the road to be closed for an extended period requiring travel and shipping to be rerouted for days or even months. In extreme cases such as following severe storms, towns can become isolated due to one or multiple failures. In addition, property damage and even loss of life may occur.

Figure 1. Road Collapse Example. (*123rf.com*)

Current Technology

Surveys are periodically made on important roads to detect pavement distress, and railway staff are continually monitoring the state of the track. However, vulnerability due to subbase or subsurface materials degradation is not related to visible pavement distress. There do not appear to be any good means currently available for real-time monitoring to discover subsurface failures.

Geophysical Methods

Geophysical survey methods are used to evaluate geological conditions during the design phase, but their usefulness for subsequent maintenance of road works is uncertain (*O'Flaherty;* 2002). Typically they depend on physical manipulation of the region to be tested, for example by boring temporary holes. In any case these methods require the use of specialist personnel.

Seismic refraction is one such geophysical survey method (*Daley et al.*; 1985). This methodology typically requires, at each location to be tested, a bore hole of several inches diameter filled with explosives. Approximately five locations per day can be tested.

2D resistivity imaging has also been used, especially for looking at possible collapsed mine shafts, and for karst regions. This methodology works on the principle that ground resistance changes when encountering a cavity. However, the nature of the change depends strongly on whether the cavity is water filled. Also, this technique is only applicable in some soil types.

Measurement of flexible (typically asphalt, as opposed to rigid concrete) pavement structure is commonly done by subjecting the pavement at suspect locations to stress such as Benkelman beam, Dynaflect and similar falling weight deflectometers, to measure road deflections (*Garber and Hoel; 2010*). Although these methods can detect weaknesses, they are sufficiently time consuming and equipment-intensive that it is difficult to justify using them routinely.

All of the above methods require manipulation of the ground or road at the location to be tested, which limits testing to a small number of locations per day. Thus, geophysical survey methods are not useful for routine monitoring of an entire road.

Radar and Other Non-contact Methods

Another category of methods uses equipment which does not require physical modifications to the road. The most widely used of these is *ground penetrating radar (GPR).*

The U.S. Federal Highway Administration (*FHA;* 2011) says that by using GPR, highway engineers can assess subsurface conditions at a fraction of the cost of conventional methods, claiming that GPR systems can survey pavements quickly and with minimal traffic disruption and safety risks. However, users have found numerous difficulties in interpreting the GPR data (*Cardamona;* undated).

GPR produces a recording of patterns of dielectric constant changes beneath the measuring device. Interpreting this information requires pre-existing knowledge of the dielectric constants of all materials (both pavement and soil) which will be encountered during the survey. Use of GPR also assumes that the road itself is of consistent and continuous structure.

Attempts to use *optical remote sensing* from satellites or airborne instruments for assessing road condition have not yet been effective even for discovering pavement surface conditions. One report said that it is difficult to even find and measure the width of roads (*Qihau;* 2008).

Lidar, which uses laser pulses to accurately measure elevation, is a possible approach to remote sensing of road conditions. It is true that lidar can detect pavement subsidence which is too small to be seen by the unaided eye. However, lidar is a difficult and expensive technology. Furthermore, except possibly for airport runways, the presence or absence of subsidence is not a strong indicator of subsurface problems.

Finally, all of the techniques described are looking for anomalies in the road structure and the underlying geology, rather than looking for actual early-stage damage. This is a problem because such anomalies may or may not indicate damage. The existing technologies cannot in themselves distinguish between benign and threatening situations.

Objectives

What is needed is a system which permits examining, or visualizing, the current condition of a road structure *before* the degradation of the structure becomes externally visible in the form of a subsidence or collapse. We would like this examination to be easy, fast, convenient, and not require specially trained personnel. It should be possible to perform this examination routinely (for example every year) or to meet a sudden demand (for example, a realization that extreme weather or seismic activities have put a road in danger).

The system we have designed meets these criteria, provided that the specialized geofabric has been embedded into the road during construction or reconstruction. Once embedded in the road, this geofabric is entirely passive. It does not require any power or external electrical connections, either permanently or during use. It does degrade over time of course. Everything degrades over time. However it is precisely this degradation which provides the information needed to visualize the road condition. Degradation of the geofabric indicates probable problems with the road structure.

Typical Use Configuration

The system consists of a material, the geofabric, plus a sensor apparatus for real-time monitoring and detection of subsurface failures of a road, highway, airport runway, railway track, river or ocean dike, or similar construction which is earth supported.

The geofabric must be built into the highway either inside or between pavement layers or above the subbase. There is no requirement for physical access to the geofabric after road construction and the fabric is entirely passive except during examination. An examination permits discovery of damage to the subsurface structure of a road before damage becomes apparent on the surface through subsidence or collapse.

Examining the condition of a road is done by passing the sensor assembly along the surface of the road, for example by attaching it to a car or truck as shown in Figure 2. When the sensor assembly probes the fabric remotely, damage, such as a tear, becomes apparent. This damage is assumed to imply possible damage to road structure, and can be shown as an image or automatically processed using conventional image-processing techniques. A sensor assembly would be constructed to detect potential failures probably across the full width of a road or road lane.
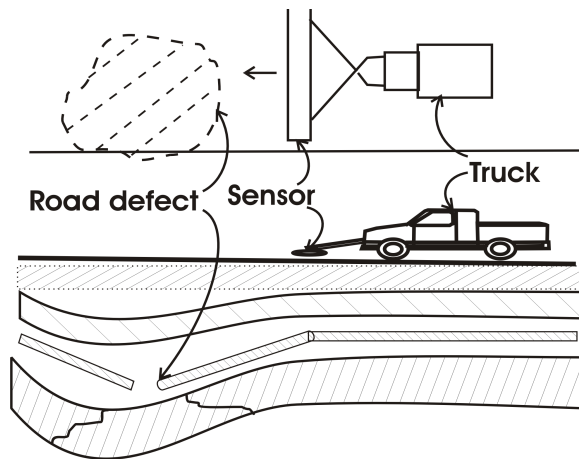

Figure 2. Road and Sensor Assembly.

Experimental Setup

As a laboratory test of this technology, we created a model of a single-lane road. The model, shown in Figure 3, is about 80 cm wide and two meters long. A simulation of the geofabric was constructed on the underside. We created a sensor apparatus following the descriptions in this paper. The potential imaging resolution for the combination of fabric and sensor was approximately 24 x 24 cm
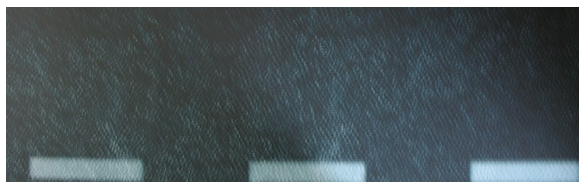

Figure 3. Model of One-Lane "Highway".

Figure 4 shows a block diagram of the sensor system. In our test system we replaced the geographic positioning system (GPS) receiver by a

sensor which allowed us to determine how far along the model highway the sensor system was located at any given moment. This corresponds to the odometer in a car. We did not include the optional alarm

The sensor measurements are converted to digital form and made available to a microprocessor (a laptop PC, in our case). The computer collects the measurements as the sensor is moved along the road surface. One set of measurements constitutes one line of data across a road. In a full implementation, each data line would be tagged with the exact time and location from a location sensor such as the GPS receiver shown and saved to a disk file for later processing and/or displayed as one line of an image on a display and/or used to warn the operator with an alarm. In our test system, we simply tagged the data with the time (seconds since start) and displayed it on the computer screen.
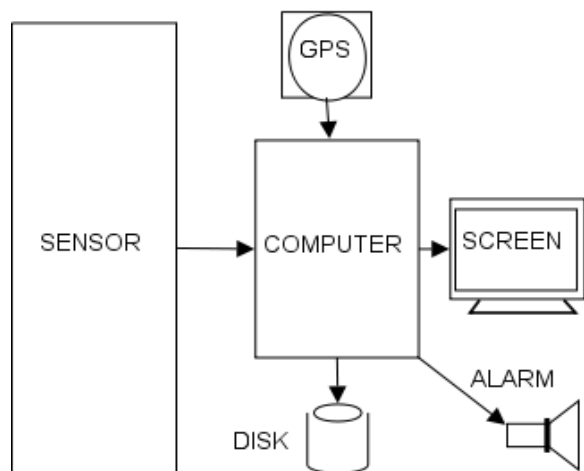

Figure 4. Sensor System Block Diagram

Figure 5 shows a flow chart of the software for the sensor assembly. The software consists of an infinite loop in which it first gets time and location data and then obtains one row, or scan line, of sensor data taken cross-wise on the road. The software then checks to see whether the data indicates a damaged area of fabric and stores this information in a line buffer memory. The software may also save the line buffer contents to disk and/or append the line buffer contents to an on-going display and/or produce an alert in some other way. All the above-listed steps are then repeated.

Results

We conducted tests of the model in three situations: a) no damage to the geofabric indicating that the road subbase is intact; b) slight damage to the geofabric indicating possible local damage to the subbase which should be checked again in a few months; and c) extensive damage to the geofabric indicating a need for immediate repairs.
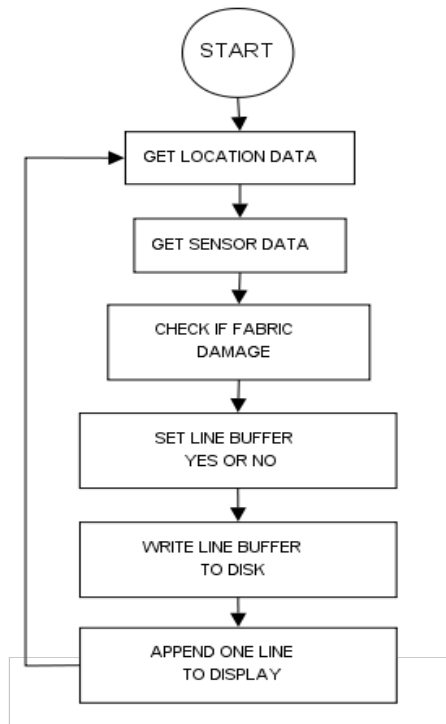
Figure 5. Sensor Software Flow Diagram

Figure 6 shows the test model in use. In all three tests, the "damaged" and intact regions of the geofabric were correctly detected.. Figure 7 shows the screen images obtained from these three tests
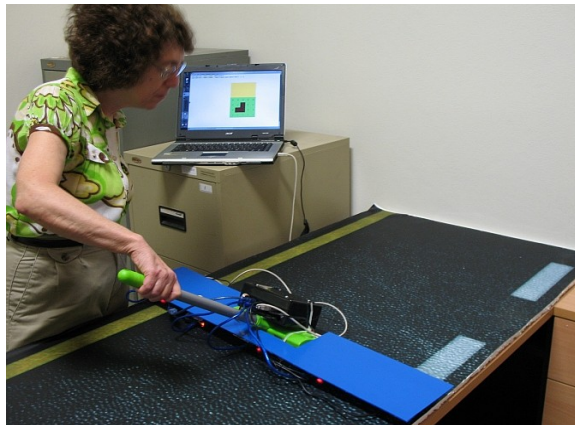

Figure 6. Test Model in Use.
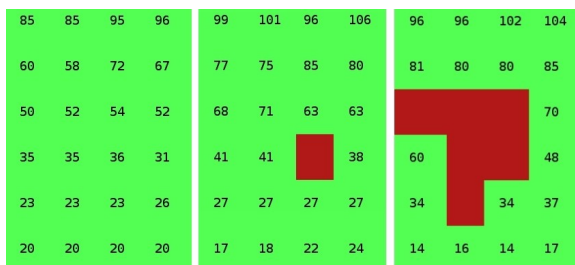
(a) No damage   (b) Minor damage   (c) Major damage

Figure 7. Detected Road Damage.

Future Plans

This paper has described a new geofabric and sensor combination. While the sensor assembly tested is very similar to the expected full-size sensor, the geofabric was tested only by simulation. Before we can begin to use this to build real roads we need to test using a real geofabric, and using test roads built with more realistic construction materials rather than styrofoam.

Conclusions

Deterioration of the subsurface structure of a road, highway, airport runway, railway track, river or ocean dike, or similar construction which is earth supported can lead to unanticipated collapse, which in turn causes expenses to perform emergency repairs, economic losses due to traffic rerouting, possible destruction of property, injury to people or animals, and even death.

Our research demonstrates an early warning system which permits routine and inexpensive real-time monitoring and detection of such subsurface failures, before the incipient failures become apparent at the surface. Use of this system will enable preventive measures to be applied at convenient and scheduled times, rather than waiting until a catastrophic failure mandates emergency repairs.

References:

123rf.com (undated photo), http://www.123rf.com/photo_9574506_part-of-demolished-road-near-coast-ordzhonikidze-urban-village-environs-crimea-ukraine.html

Cardimona,S. et al, (undated), Ground Penetrating Radar Survey of Interstate 70 Across Missouri, *The University of Missouri-Rolla, Department of Geology and Geophysics and the Missouri Department of Transportation.*

Daley, M.A.,et al (1985), Seismic Refraction Data Collected in the Chugach Mountains and along the Glenn Highway in southern Alaska in 1984, *United States Department Of The Interior Geological Survey USGS Open-File Report: 85-531.*

FHA (2011), Priority, Market-Ready Technologies and Innovations: Ground-Penetrating Radar, *Federal Highway Administration report FHWA-HRT-04-072.*

Garber, N.J. and Hoel, L.A. (2010), Traffic and Highway Engineering, 4th Edition, *Cengage Learning.*

O'Flaherty, C.A. ed (2002), Highways: The Location Design, Construction and Maintenance of Road Pavements, 4th Edition, *Elsevier.*

Qihau Weng (2008), Remote Sensing of Impervious Surfaces, *CRC Press.*

Application of Spark Plasma Sintering for Fabrication of Functionally Graded Thermal Barrier Coating on a Superalloy Substrate

M. Bahrami[1], A.H. Pakseresht[2], A.H. Javadi[3], A. Simchi[1*]

[1]Department of Material Science and Engineering, Sharif University of Technology, Tehran, Iran
[2]Department of Ceramics, Materials and Energy Research Center, Karaj, Iran
[3]Engineering Research Institute, Tehran, Iran
[*]Corresponding author. Tel: (+98) 2166165261; Fax: (+98) 2166005717; E-mail: simchi@sharif.edu

Abstract: Thermal barrier coatings (TBC) are commonly used in high temperature components of gas turbine engines such as blades, vanes and nozzles, for aeronautic and energy production applications. These coatings consist of superalloy substrate, metallic layer called bond coat, and ceramic layer called top coat. The difference between the thermal expansion coefficient of ceramic and metallic layers is an unfavourable parameter leading to an extensive usage of functionally-graded coatings. In this paper, a novel procedure is presented to prepare functionally-graded TBC. The process includes spark plasma sintering of a nanostructured 8% yttria stabilized zirconia (8YSZ) layer (~200 μm) on the top of 738 superalloy substrate. An intermediate layer of 50%YSZ+ 50%NiCrAlY is utilized. A bond coat of NiCrAlY is also used close to the substrate. Microstructural studies show that the prepared coatings are dense and without common defects of conventional coatings such as pores and micro-cracks. The grain size of the TBC is in the range of 40-50 nm, which indicated very limited grain growth of the nanostructured ceramic powder (30 nm) during the sintering process. These microstructural features of the bonded area and the advantages of the process are presented.

Keywords: Functionally graded materials, Thermal barrier coating, Spark plasma sintering, Nanostructure .

Introduction

The main function of Thermal barrier coating is to decrease the surface temperature and consequently to reduce oxidation and corrosion rates of the superalloy as substrate. The most common TBC-system can be considered as a four-layer material, consisting of (1) superalloy substrate, (2) metallic bond coat (BC), (3) thermally grown oxide (TGO) and (4) ceramic top coating (TC) [1-4]

Recently, FGM layers with gradual compositional variation are employed between the top and bond coats, which consist of composing of ceramics and metals in various ratios .This kind of coating reduces the residual and thermal stresses and enhances bonding strength along the interface of the coating and the substrate [5-8].

The ability of producing full FGM-TBC systems in one step can decrease the manufacturing costs and research complications. Usage of SPS can cause the elimination of multiple process steps. The major purpose of this research is focused on in situ production of FGM-TBC coating containing of the nanostructured top layer. Nanostructured YSZ has been used to decrease the sintering temperature and to improve the performance of multilayer TBC coatings.

Experimental

The substrate used for this study was a 30 mm diameter disc, which was made of Ni-base superalloys (738). The substrate surface was mechanically polished using 2000 grit SiC paper and cleaned with acetone.

NiCrAlY (Metco 442) commercial powders with an average particle size of 70μm were used as bond coat. The top coat was fabricated from high purity (> 99.9%) commercial 8YSZ (US3630) powder with an average particle size of 40 nm.

A pure Al foil with a thickness of 10μm was positioned between the %50 YSZ + %50 NiCrAlY mixed powders (FGM layer) and the NiCrAlY powder in order to generate the Al2O3 TGO to keep the interface flat and homogeneous after sintering.

For producing TBC coating, at first superalloy disc was inserted into a graphite die (with an inner diameter of 30 mm). Then the powders were poured on the substrate with a specified order.

The samples were sintered at 1045 °C, under a pressure of 40 MPa with a dwell time of 10 min by SPS (Easy Fashion 20T-10) apparatus.

The microstructure of the coating samples was characterized by SEM (VEGA//TESCAN-XMU, Russia), using a microscope equipped with an EDX system.

Results and discussion

One step fabrication of complete FGM-TBC system

Figure 2 shows relation among densification, temperature and pressure. As shown in Fig.2 the pressure pattern begins with an initial dwell of 10 MPa, and increased to 20 MPa at 600 °C. Then the pressure was held at 20 MPa until the final temperature reached up to 1045°C, and then it increased to 40MPa. In this process expansion occurred due to the

consolidation behaviour of the green body and thermal expansion coefficient of substrate [3].
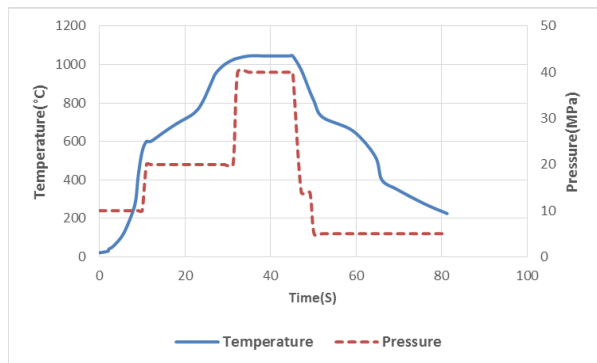

Fig. 1.Temperature-Pressure curve in SPS process

FGM-TBC coating which was prepared by SPS has five layers are as following:
a) Inconel substrate b) Bond coat layer with a 100 micron thickness, c) TGO layer with a 5-10 μm thickness, d) 50% 8YSZ and 50%NiCrAly with 200 μm thickness and e) 8YSZ with a 200 μm thickness as a top layer. Fabrication of FGM-TBC coating has been carried out in one step by SPS for the first time. Sintering temperature difference of materials is a key parameter to optimize the sintering temperature, time and applied force.

Microstructure
SEM micrograph of heat treated FGM-TBC was shown in Fig. 2. This figure presents formation of dense layers and absence of common sprayed defects such as pores and micro cracks.
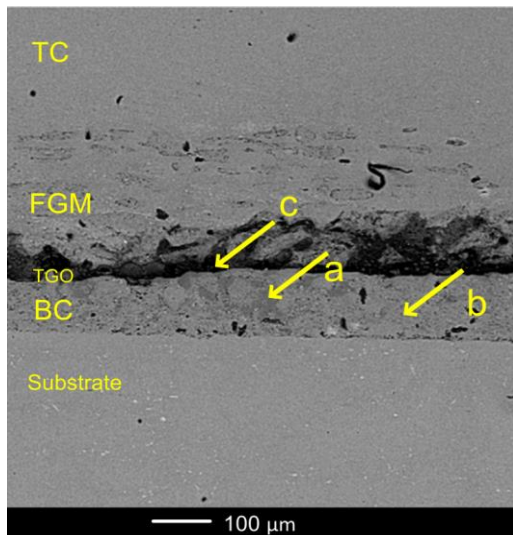
Fig. 2.BSE image of FGM-TBC system fabricated in one step by SPS and heated at 1000 °C

It was observed that the bond coat comprised two main phases: Solid solution of γ (Ni) with dark gray colour (point A) and β (NiAl) phase with bright gray colour (point B).
Point C of Fig.2 shows the TGO layer of TBC. This layer was composed of alumina with small ZrO_2 inclusions.
The role of β phase is the Al storage to form the Al_2O_3 protective layer [9].
In SPS process, samples don't contain typical lamellar structure, pores, cracks and inter splat boundaries. Thus, elimination of these defects can improve mechanical and physical properties of SPS samples.

TGO formation
TBC life depends on the properties of TGO layer [1]. The thin black layer in Fig. 2 is the TGO (Al_2O_3) layer. The formed TGO improves the durability and reliability of TBCs by stress concentration reduction and thermal fatigue enhancement [3]. In this system, TGO grows during the coating process and it is non-uniform in both composition and thickness [3, 10].
In SPS process, initial TGO layer is formed by the reaction between the Al with ZrO_2 in the top coat [3]. There are two sources of Al in this coating process: Al can be accessible by Al diffusion from substrate, BC and FGM layer to TGO layer, and by Al foil [1, 3].

Nanostructure of top coat
Keeping the initial structure of nano powder in the top layer is one of the purposes of this research. The SEM image in Fig. 3 shows grains size of 8YSZ as a top coat, which was fabricated without noticeable grain growth and has a nano-structure. Using nanometer YSZ as a top coat provides better properties than conventional micrometer-sized ones such as higher coefficients of thermal expansion, lower thermal diffusivity, higher hardness and toughness and better wear resistance [11, 12].
In SPS process because of lower sintering temperature and dwell time, it is possible to obtain nanostructural layer. Nano sized YSZ is a dense layer which remains without cracking even after cutting section (as shown in Fig. 3).
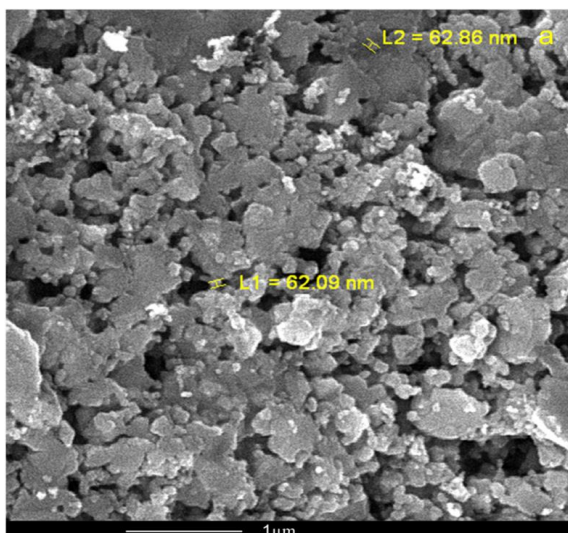
Fig. 3.Grains size of 8YSZ as a top coat

Conclusion

By employing spark plasma sintering, a FGM-TBC coating based on 8YSZ/%50 8YSZ+%50 NiCrAlY/Al$_2$O$_3$/NiCrAlY layers on 738 superalloy substrate was Fabricated. Sound parts were obtained after sintering at 1045°C under 40 MPa pressure. The microstructural features of the prepared coatings were almost as the same of the conventionally prepared TBCs but the grain size of the top layer was of <100 nm. No defects, pores and cracks were observed in the microstructure of the prepared coatings.

Acknowledgement

References:

1. Boidota, M., Selezneff, S., Monceau, D., Oquab, D., Estournès, C.(2010), Proto-TGO formation in TBC systems fabricated by spark plasma sintering, *Surface & Coatings Technology*, 205 (5), 1245–1249.
2. Hejwowski, T.(2010), Comparative study of thermal barrier coatings for internal combustion engine, Vacuum. 85 (5), 610-616.
3. Song, J., Ma, K., Zhang, L., Schoenung, Julie M. (2010) , Simultaneous synthesis by spark plasma sintering of a thermal barrier coating system with a NiCrAlY bond coat, *Surface & Coatings Technology*, 205 (5), 1241–1244.
4. Vande Put, A., Oquab, D., Pe´re´, E., Raffaitin, A., Monceau, D.(2011), Beneficial effect of Pt and of pre-oxidation on the oxidation behaviour of a NiCoCrAlYTa bond-coating for thermal barrier coating systems, Oxid. Met. 75 (5-6), 247-279.
5. Lee, Y.D., Erdogan, F. (1994/1995), Residual/thermal stresses in FGM and laminated thermal barrier coatings, Int. J. Fract. 69 (2), 145-165.
6. Chi, S., Chung, Y.(2003), Cracking in coating substrate composites with multi-layered and FGM coatings, Eng. Fract. Mech.70 (10), 1227–1243.
7. Afsar, A.M., Song, J.I.(2010), Effect of FGM coating thickness on apparent fracture toughness of a thick-walled cylinder, Eng. Fract. Mech.77 (14), 2919–2926.
8. Khoddami, A.M., Sabour, A., Hadavi, S.M.M. (2007), Microstructure formation in thermally-sprayed duplex and functionally graded NiCrAlY/Yttria-Stabilized Zirconia coatings, Surf. Coat. Technol. 201 (12), 6019–6024.
9. Poza, P., Grant, P.S. (2006), Microstructure evolution of vacuum plasma sprayed CoNiCrAlY coatings after heat treatment and isothermal oxidation, *Surface & Coatings Technology*, 201 (6), 2887-2896.
10. Liu, J., Byeon, J.W., Sohhn, Y.H. (2006), Effects of Phase Constituents and Microstructure in Thermally Grown Oxide on The Thermal Cycling Lifetime and Failure of Thermal Barrier Coatings, *Surface & Coatings Technology*, 200, 5869-5876.
11. Bacciochini, A., Montavon, G., Ilavsky, J., Denoirjean, A., Fauchais, P. (2010) , Porous architecture of SPS thick YSZ coatings structured at the nanometer scale (~50 nm), *Journal of Thermal Spray Technology*, 19 (1-2), 198-206.
12. Racek, O., Berndt, C.C., Guru, D.N., Heberlein, J. (2006), Nanostructured and conventional YSZ coatings deposited using APS and TTPR techniques, *Surface & Coatings Technology*, 201 (1-2), 338–346.

Synthesis and Optical Characterization of Ca_2PO_4Cl:Tb^{3+} and Mn^{2+} phosphor for solid state lighting.

N.S.Kokode[*1] , V.R.Panse[2] and S. J. Dhoble[3]

[1]N.H.College,Bramhapuri, Gondwana University Gadchiroli-441205,India

[2]Department of Applied Physics, NCET, Gadchiroli,442605,India

[3]Department of Physics, RTM Nagpur University, Nagpur -440033, India

*1Corresponding Author: drns.kokode@gmail.com

Abstract

In our work we studied the luminescence properties of Tb^{3+} and Mn^{2+} doped Ca_2PO_4Cl phosphor synthesized by wet chemical method with extra heat treatment, to understand the mechanism of excitation and the corresponding emission of prepared phosphor. Generally for the green emission, Tb^{3+} ion is used as an activator, the excitation and emission spectra indicate that this phosphor can be effectively excited by 380 nm, to exhibit bright green emission cantered at 545 nm corresponding to the f→f transition of Tb^{3+} ions. The emission spectrum of Mn^{2+} ion at 405 nm excitation $^4T_1(4G)$-$^6A_1(6S)$ gives an emission band at 591 nm (orange-red) . The observed photoluminescence measurements of Tb^{3+} and Mn^{2+} activated prepared phosphor indicates that these are the outstanding potential phosphor ,suitable for the solid state lighting. The phosphors were used for further characterization by X-ray diffraction (XRD), scanning electron microscopy.

Keywords: - Wet Chemical Method, Solid state lighting, Photoluminescence, XRD,SEM

Introduction

Solid-state lighting and phosphor material to produce white light is the recent research focus in the lighting industry. It has lots of advantages over conventional fluorescent lamps for example reduced power consumption, compactness, efficient light output, and longer lifetime. Solid-state lighting will have its impact on reducing the global electricity consumption.[1-2] White light-emitting diodes (LEDs) can save about 70% of the energy and do not need any harmful ingredient in comparison with the conventional light sources, such as incandescence light bulbs and the luminescent tubes. [3] Therefore white LEDs have a great potential to replace them and are considered as next generation solid state light devices [4-5]. Rare earth ions are characterized by an incompletely filled 4f shell, which can absorb the excitation energy to be at the excited state and then return to the ground state, resulting in emitting state in the visible region [6-7]. These feature transitions within the 4fn configuration have been found an important application in lighting and display. The syntheses of conventional rare earth phosphors primarily focused on the high-temperature solid-state reactions providing agglomerated powders. They can allow to readily altering the structural characteristics of the powders [8].So in this paper we focused on the preparation conditions and process of the phosphor with extra heat treatment because many factors affect its structure and luminescent properties. The Tb^{3+} and Mn^{2+} doped Ca_2PO_4Cl phosphor were prepared by using wet chemical method with extra heat treatment and their luminescent properties are discussed in detail and thermal stability, the

synthesis processing details and factors those affect the structure and luminescent properties of phosphor [9] were also studied.

Experimental

Sample Preparation

Phosphors with compositions of Ca_2PO_4Cl explained prepared by a wet chemical synthesis method with extra heat treatment. The constituent raw materials was all from A.R. grade from merk such as $Ca(NO_3)_2$,NH_4Cl and $NH_4H_2PO_4$, Tb_4O_7 and $Mn(NO_3)_2$with purity 99.99 %. Tb_4O_7 is converted in to nitrate form by mixing of appropriate amount of dilute nitric acid. All the mixtures were mixed according to stochometric ratio. Take an appropriate amount of distilled water to dissolve all the compounds. After dissolving all the mixture put it on magnetic stirrer for complete the dissolve process. The resulting solution is then transferred into a hot oven maintained at 100^0C for 24 hrs. After that the solid compound was formed kept it out of oven and crush it for 15 to 20 minute and then a homogeneous compound was formed which was further heated at 350^0C in case of Tb^{3+} for 8 hrs and with reducing atmosphere of charcoal treatment at 450^0C for 12 hr duration in case of Mn .The final product obtained is in the powder form, which is used for the further investigations.The resultant powder was formed which was collected and used for the further analyzed. The same amount of sample was used for each measurement. Emission and excitation spectra were recorded using a spectral slit width of 1.5 nm.
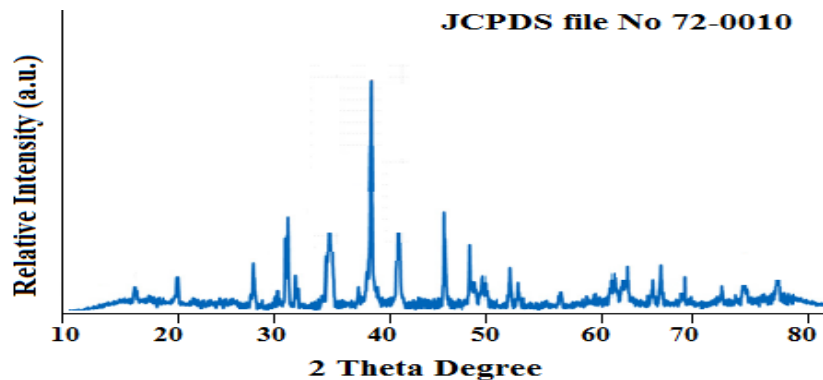
Results and discussion:- XRD phase analysis

FIGURE 01. XRD-pattern of Ca_2PO_4Cl phosphor

In order to explore the crystal phase structure, the XRD phase analysis was adopted. The typical XRD patterns of Ca_2PO_4Cl phosphor are shown in Fig. 1. For the obtained phase, it is carefully observed that there are no peaks of raw materials. It is found that the main phase is in good agreement with standard JCPDS data file available i.e. file no.72-0010.

SEM Analysis

The surface morphology and crystalline sizes of the synthesized Ca_2PO_4Cl phosphors was observed and shown in fig 02. It can be seen that all of the phosphor powders consisted of irregular grains with an average size of about micrometer range and have surface morphology of crystalline grains i.e. looks like sharp edge chip . It is seen from the micrographs that the crystallite sizes vary from a few microns to several tens of microns.
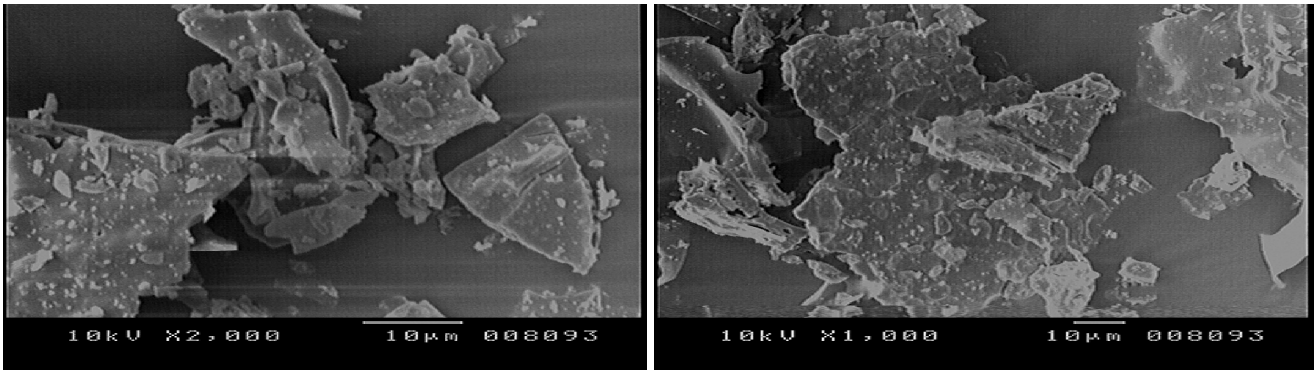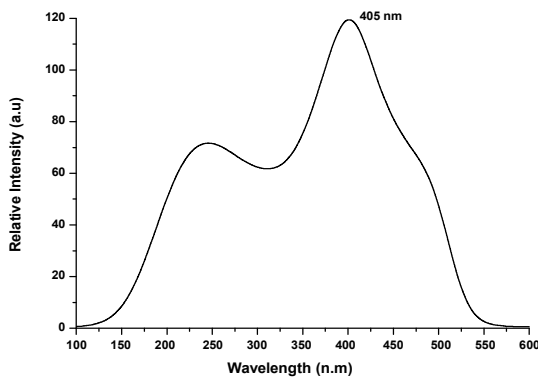
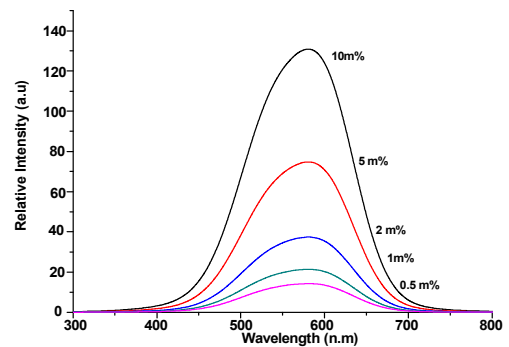**Figure 02** SEM of Ca_2PO_4Cl phosphor
Photoluminescence Measurements
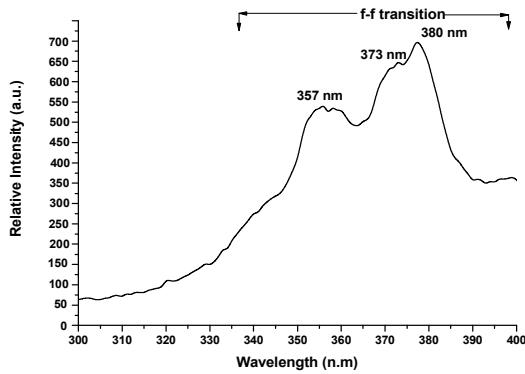
FIGURE 3 . Excitation spectrum of $Ca_2PO_4Cl:Tb^{3+}$ phosphor at $\lambda em= 545$ nm
FIGURE 4. Emission spectrum of $Ca_2PO_4Cl: Tb^{3+}$ λex 380 nm
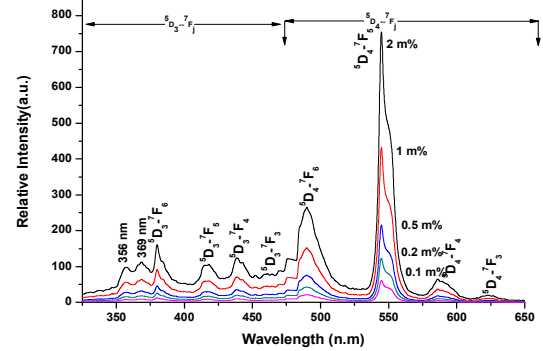
FIGURE 5 . Excitation spectrum of $Ca_2PO_4Cl:Mn^{2+}$ phosphor at $\lambda em= 591$ nm
FIGURE 6. Emission spectrum of $Ca_2PO_4Cl: Mn^2$ λex 405 nm

As shown in fig 03,the excitation spectrum observed at 545 nm emission wavelength of Ca_2PO_4Cl activated withTb^{3+} consisting of a broad band as well as some sharp lines. Some peak observed due to f-d interaction while sharp lines are due to f-f transitions. The emission spectrum fig 04 has sharp lines on account of f–f transition of Tb^{3+} ions. The emission spectrum usually has major contribution from $^5D_4–^7FJ$ (J= 6, 5, 4, 3) and peak due to $^5D_3–^7F_{J(J= 6, 5, 4, 3)}$ can also be seen. The nature of $^5D_4 \rightarrow {}^7F_J$ transitions is governed by the selection rule $\Delta J = \pm1$ for electric dipole and $\Delta J = 0, \pm2$ for magnetic dipole transitions respectively. The emission intensity of $^5D_3$ level is very weak and weakens further with increasing Tb^{3+} concentration, followed by the enhancement of the emission from the $^5D_4$ level, occurs due to non-radiative cross-relaxation via the resonant energy transfer process between $^5D_3$ and

$^5D_4$ levels. As the concentration of Tb^{3+} is changed, the cross-relaxation effect becomes stronger, which enhances the intensity of green emission at 545 nm. The other reason that has been assigned to weak luminescence from $^5D_3$ level is the lack of phonon energy of the host. The smaller the phonon energy of the host at diluted concentrations of terbium ions, the lower will be the $^5D_3$ emission intensity and vice versa [9-10]. Fig. 05 shows that Ca_2PO_4Cl: Mn^{2+} had a orange-red emission around 591 nm, ascribed to the spin forbidden $^4T_1(4G)$–$^6A_1(6S)$ transition of the Mn^{2+} ion for different Mn^{2+} concentrations. The excitation spectrum of Ca_2PO_4Cl: Mn^{2+} contains a number of bands, and the strongest excitation at 405 nm corresponds to the transition from the $^6A_1(6S)$ ground state to the excited states [4E(4G), $^4A_1(4G)$]shown in fig 05. [11-12]. The emission intensities increased with increasing Tb^{3+} and Mn^{2+} concentration, reaching a maximum at 2 m% and 10 m%.

Conclusion

Tb^{3+} and Mn^{2+} activated Ca_2PO_4Cl phosphor was prepared successfully by the wet chemical synthesis with extra heat treatment. The SEM indicated that the particle size of the phosphor is in the sub-micron range .The crystal phases of the prepared particles were analyzed by Xray diffraction (XRD) pattern which is exactly match with standard JCPDS data file. The emission spectrum of Ca_2PO_4Cl:Tb^{3+} (at 380 nm excitation) has intense bands cantered at 545 nm and which correspond to the green regions and under the excitation around 405 nm, the Ca_2PO_4Cl:Mn^{2+} phosphors show the orange-red emission 591 nm from Mn^{2+} ion. The result indicates that Ca_2PO_4Cl: Tb^{3+} and Mn^{2+} phosphor is a good promising green emitting phosphor while Mn^{2+} is the orange-red emitting phosphor for solid state lighting.

ACKNOWLEDGMENT

References

[1] W.J. Yang, L. Luo, T.M. Chen, N.S. Wang, J.of.Chem. Mater. 17 (15) (2005) 3883–3888.

[2] I.M. Nagpure, V.B. Pawade, S.J. Dhoble, J. of. Lumin. 25 (2010) 9–13.

[3] Y. Karabulut ,A.Canimoglu ,Z. Kotan ,O. Akyuz, E. Ekdal ,J.of Alloys &Compd 583 (2014) 91–95

[4] H.A. Hoppe Angew, Chem. Int. Ed. 48 (20) (2009) 3572–3582.

[5] T.S. Chan, R.S. Liu, B. Ivan, Chem. Mater. 20 (4) (2008) 1215–1217.

[6] D.M. Burland, R.D. Miller, C.A. Walsh, Chem. Rev. 94 (1) (1994) 31–75.

[7]L.Hesselink,S.S.Orlov, A.Liu,A.Akella,D.Lande,R.R.Neurgaonkar, Science 282 (1998) 1089–1094.

[8] A.M.G. Massabni, G.J.M. Montandon, M.A. Santos Couto dos, Mater. Res. 1 (1)(1998) 1–4

[9] Nag, A.; Kutty, T.R.N.; Mater. Chemi. Physi. 2005, *91*, 524

[10] Chang,Y.S.; Lin, H.J.; Li, Y.C.; Chai, Y.L.; Tsai, Y.Y.; J.Sol.State Chemi. 180 (2007) 3076

[11]C.H.Huang,T.M.Chen,W.-R. Liu,Y.-C. Chiu, Y.-T. Yeh ,S.-M.Jang,ACS Appl. Mater. Interfaces, 2010, 2, 259.

[12]W.R.Liu, C.-H. Huang, C.W. Yeh, Y.-C. Chiu, Y. T. Yeh andR.-S. Liu, RSC Adv., 2013, 3, 9023.

Development of Through-Silicon Stacking Technology for Capacitive Acoustical MEMS Resonators

N. Belkadi,[1,*] B. Dulmet, [1], T. Baron[1]

[1]FEMTO-ST Institute, Time and Frequency Dpt., 26, chemin de l'épitaphe – 25030 Besançon Cedex, France.

nesrine.belkadi@femto-st.fr

Abstract: This article describes the key process to realize conductive vias in silicon MEMS resonators. Cancelling out the resistance of interconnections in micro-acoustic resonators structures is mandatory to improve their performances because electrostatic generation of elastic waves results into relatively small values of the electromechanical coupling factor (Ivan *et al.*; 2012). Via techniques so-called TSS (Through-Silicon Stacking or Thru-Silicon Stacking) are the cornerstone of 3D integration. The achievement of TSS consists of two main steps. First, the holes are etched through a low doped n-type silicon wafer using Deep Reactive Ion Etching (DRIE). After dry etching, the holes can be filled by a conductive material. An "electrochemical" approach was explored because of its low manufacturing cost compared to dry-chemical techniques. We propose here a brief description of these two steps while stipulating technology issues for each of them, as well as some examples of widely used methods.

Introduction:

The three-dimensional (3D) silicon integration brings many advantages regarding the device performances for everything concerning the homogeneous integration (known as 'Moore Moore'), as well as multiple opportunities in terms of heterogeneous integration (known as 'More than Moore'). The 3D integration as defined today represents a new integration schema of multi-level systems, where different layers of components are stacked and interconnected by vertical vias through the silicon floors. These vias of a new kind - they pass through the silicon - are commonly known as TSS, for "Through-Silicon Stacking", by the scientific community.

The Through-Silicon Stacking "TSS" technology is the key parameter for 3D integration allowing through-silicon connections. It must be stressed that the vertical dimension is a recent trend in the evolution of electronics and plays a leading role in the development of MEMS, NEMS and Micro-sensors. Mastering TSS technology is especially promising to micromachining capacitive Bulk Acoustic Wave (BAW) resonators with out-of-plan mechanical displacements.

The physical constitution of these conductive vias generally consists of a set of four generic steps. First, the holes are machined by Deep Reactive Ion Etching (DRIE), most often with the help of the Bosch process (Laermer et al., 1996). DRIE is the most widespread technique to elaborate structures with high aspect ratio and optimally vertical edges. This technique requires both chemical and physical silicon attacks (Laermer et al., 2010) to achieve anisotropic etching of silicon.

An initial alkaline etching in KOH bath (B. Kim et al.,) can be performed in order to decrease the depth machined by DRIE, step which allows the achievement of non-through holes. The backside of the sample is etched through a SiO_2 mask and also uses wet etching to meet the limits of the previously drilled holes of the front side in order to avoid manufacturing technology issues.

This etching step represents somehow the skeleton of the TSS. Once it is achieved, it becomes necessary to prepare the edges for subsequent operations. The first step of this preparation consists in achieving an electrical insulation of the via sidewalls from the silicon substrate in order to prevent any risk of short circuit. After this insulating coating, a barrier material is deposited to prevent atomic diffusion by substitution.

The ultimate step in the realization of the TSS consists in filling the via hole by a conductive material. Electrochemical deposition is a well-suited technique to perform this step in the frame of silicon resonators development. The electrolytic solution mainly consists of additives determined by the influence on the deposition kinetics. We briefly describe their role and their deposition conditions as well. A compound metallic seed layer is deposited on the backside of the silicon wafer in a view of a "bottom-up" filling. The main goal of this step is to improve the uniformity of the electrodeposited copper filling.

1   Through-Silicon Stacking Etching

To achieve Through-Silicon Stacking, n-type, 380 μm thick, 1−10 Ωcm resistivity, (100) silicon wafers were employed. The TSS may be etched in silicon by several techniques. Deep Reactive Ion Etching process known by the acronym DRIE commonly known as Bosch process is the most widespread technique for producing high aspect ratio (HAR - High Aspect Ratio) of TSS. It was patented by Mr. Lärmer and Mr. Schilp.

Before this deep etching step, the samples must be immersed in an aqueous solution of potassium hydroxide "KOH" which will enable us to initiate the deep etching holes. This etching is often performed through a mask (Generally a silicon dioxide mask) identified by a photolithography step (Figure 1.a) which is chemically etched in a BHF "Buffered Hydrofluoric acid" bath. The crystallographic orientation of the silicon wafer will determine an inverted pyramidal form of the etching (Figure 1.b). However, to avoid the step of thermal grown of the silicon dioxide, it is preferable to use double-ride oxidized wafers.

Figure 1 : (a) Opening of the front side oxide mask. (b) Front side alkaline etching. This leads to initiate the formation of non-through-silicon vias.

This localization of the holes is a preliminary step to the real deep etching, *i.e.*, the deep reactive ion etching which must stop execution before reaching the threshold of the backside (Figure 2).

This technique is based on the interaction between the plasma containing the fluorinated agent and the silicon surface. This process involves the cyclical repetition of two steps; the first step is a chemical and ionic etching of the silicon substrate, assisted by a fluorinated gas 'SF_6', the second is a sidewall passivation step using a polymer with the help of a 'C_4F_8' gas. After successfully etching of the silicon, SF_6 gas is immediately pumped out of the chamber

and we inject the C_4F_8 gas which generates a deposit of CF_2. This thin layer of Teflon is deposited mainly on the already etched portion and acts as passivation layer, including the sides and bottom of the TSS's making the etching unidirectional. Then, once again we inject SF_6 gas and the cycle repeats.

Figure 2: Deep Reactive Ion Etching leading to non-through-silicon vias.

The advantage of this method is that it allows the etching of various patterns with more or less straight sidewalls. The etched structures can reach aspect ratios of up to 30 (Dixit et al., 2008). It is mandatory to take into consideration the presence of ripples on the sidewalls of the holes during the elaboration of this step (Figure 3). These ripples, often denoted "scalloping effect" result from the isotropic etching and the passivation of the sidewalls to obtain high aspect ratio via. They can create stresses and be responsible for deposition-conformity defects. This method is very expensive because it does not allow a parallel processing of wafers, to the inverse of the electrochemical way.
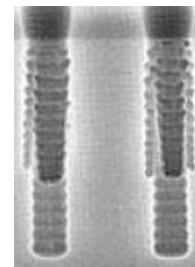
Figure 3. MEB image of through-holes created by DRIE with an example of etching defect: scalloping, (Garrou et al., 2008).

After etching the oxide mask situated on the backside preceded by a photolithography step (Figure 4.a), two methods are possible for achieving the through holes to eliminate the residual silicon layer in oxide-free regions (Figure 4.b):

- Either the withdrawal by RIE 'Reactive Ion Etching',
- Or by alkaline etching 'KOH bath'.

The second process is chosen because it presents a definite advantage over the twin-plan; economic (low

cost way) and physical (reduced surface roughness). The advantage of this step etching is summed up in search of the best way to avoid the edge defects.

Figure 4: (a) Opening of the backside oxide mask. (b) Backside alkaline etching. This leads to formation of through-silicon vias.

At this level of the process, the holes made in this manner are not ready to be filled with copper to form TSS. Other treatments are necessary for the achievement of these last one.

2 Through-Silicon Stacking Filling
TSS Insulation Sidewalls
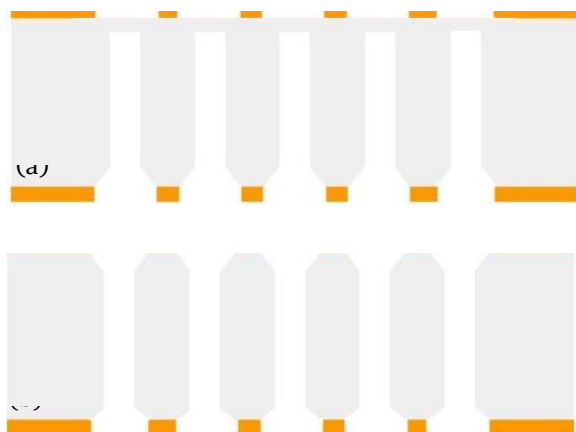
Once etch is performed, the samples are annealed under oxygen in order to grow an oxide layer of a several hundred nanometers of thickness (Figure 5). This layer electrically isolates the silicon from the electrolyte where it is immersed during the copper deposit. The isolation is performed by conformal deposition of a dielectric, generally an organic silicon type TEOS (tetraethylorthosilicate or tetraethoxysilane $Si(OC_2H_5)_4$) giving a silicon oxide 'SiO2' after deposition. In most cases, the deposit is carried out by [1]SACVD if the temperature allows it (400 °C) or [2]PECVD if the thermal budget is lower (Note that for PECVD, lower is temperature, less compliant is the deposit. One study showed good compliance of the deposit SACVD at 400 °C with a level of residual stresses rather modest (Chang et al.; 2004). The two extreme values of deposit thicknesses of oxide are 0.05 µm and 0.5 µm. The minimum value corresponds to the thickness limit not to be exceeded for reasons of reliability (A thinner deposit could cause important insulation defects), while the maximum value is a technology recommendation to avoid increasing the diameter of TSS.

---

[1]SACVD: Sub-Atmospheric pressure Chemical Vapor Deposition.
[2]PECVD: Plasma-Enhanced Chemical Vapor Deposition.
[3]PVD: Physical Vapor Deposition. This generic denomination includes all types of physical processes deposition.
[4]CVD: Chemical Vapor Deposition. This is also a generic denomination that includes all chemical vapor deposition.
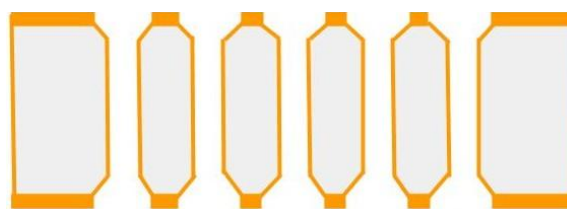

Figure 5: Silicon thermal oxidation. This leads to electrically isolate the silicon from the electrolyte.

Barrier Material Deposit

Atomic diffusion by substitution is a well known physical phenomenon in microelectronics: metal atoms may move to another material by exchanging their respective places in the crystallographic structure. This physical phenomenon is activated by temperature. In the case of silicon, the copper diffusion is facilitated, which may lead to a certain quantity of copper in the silicon, thus making him to lose its semiconducting properties. To prevent copper diffusion into silicon, we employ the said barrier material, whose function is to block literally copper atoms diffusion (Figure 6). These materials also prevent parasitic copper growth on the sidewalls of Si, thus localizing the growth from a metal base situated on one side of the sample. Details about implementation of this step will be explained subsequently. The commonly used materials are generally the nitrides, such as titanium nitride (TiN), tantalum nitride (TaN) or tungsten nitride (WN), deposited in most cases by [3]PVD or by [4]CVD, but the ease of implementation as well as its low cost makes sputtering a much appreciated technique for the microelectronics industry.

Figure 6: Barrier material deposition. This leads to stop the copper atoms diffusion and limits the parasitic copper growth on the sidewalls of silicon.

It has been demonstrated, as part of TSS, that the SiO2 insulator deposition using PVD technique significantly improves barrier integrity. This material presents the advantage to be conform (homogeneous thickness) on structures with high aspect ratio and makes the surface of silicon more hydrophilic. Thus, the penetration of the electrolyte inside the pores is facilitated. The two layers of materials are therefore complementary (Zhang et al., 2005).

The required characteristics of these materials are a low resistivity and stability at a temperature 450 ° in order not damage the doping of the substrate, hence the interests of the called 'Seed Layer'.

SEED LAYER DEPOSIT

In parallel to the deposition of the copper barrier diffusion; a nucleation layer; commonly known as *Seed Layer*, will be deposited by PVD. This base consists of a bilayer of Ti/Au, or Ti has the function of facilitating the adhesion of gold to barrier material. In our case 'Through holes', this layer must be deposited only on the backside of the holes and not on the sidewalls (Figure 7), and is essential to the growth of copper from the backside for a 'bottom up' filling. It's on its surface that occurs the cupric ions reduction to copper metal; contrary to the non-through-holes where the hole is completely covered. The sample is then ready for filling.
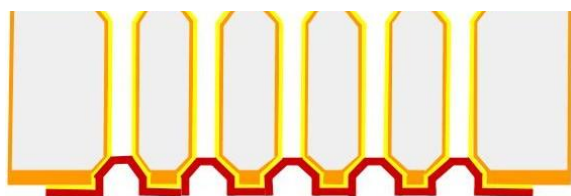

Figure 7: Backside Seed Layer deposition. This ensures the metal electrochemical bottom-up filling.

The function of the Seed Layer consists to initiate the electrolytic deposit; it is made necessary by the high resistivity of the barrier materials which induces a considerable ohmic drop during electrolysis and does not allow thus a uniform deposition of copper on the surface of the silicon wafer.
All these steps constitute an obliged passage to a successful filling of the structures by copper using an electrochemical way.

COPPER FILLING BY ELECTROCHEMICAL WAY

As mentioned in the introduction, the filling of vias will be done essentially by electrochemical deposition of copper due to its low production cost. This deposition is carried out by immersing the sample in an aqueous solution of copper sulphate '$CuSO_4$', sulfuric acid H_2SO_4 to which will be added three additives whose denomination comes from the impact they have on the kinetics of deposition:

- The accelerator, [5]SPS, whose role is to favor the growth of Cu from the bottom of the holes.

- The suppressor, compound of [6]POE and chloride ions which is absorbed in the surface of the sample, but few or no into the holes which limit thus the growth of copper on the sample surface.

- And finally, the leveler [7]JGB whose role is to limit the growth of Cu vias at the exit.
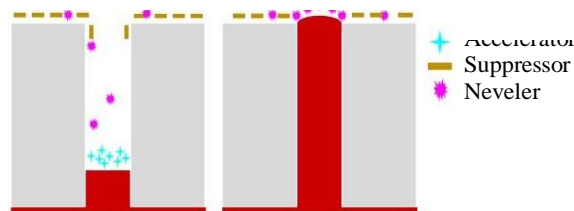
Figure 8: Schema of the impact of additives (accelerator, suppressor and leveler) on the holes filling.

On the other hand, the quality of filling holes is conditioned both by the nature of the electrolyte and the deposition conditions. However, the solution must be adapted for High Aspect Ratio (HAR) structures in order to limit the risk of inclusions voids during the filling (homogeneous copper growth), this risk is exacerbated when the nucleation layer covers the walls of the holes leading to premature closure causing thus low conductivity copper filling.

A chemical mechanical polishing or CMP step is required at the end of filling in order to remove the metal base on backside of TSS, allowing then the mutual insulation (Figure 8).

Figure 9: Backside Chemical Mechanical Polishing. This leads to the separation of through-silicon holes.

Conclusion:

In this paper we have described the realization of TSS involving a process where the first step is performed by both KOH and DRIE leading to the formation of the via holes. Then, the holes were filled by copper electromechanical deposition.

---

[5]SPS: SulfoPropyldiSulfite.
[6]POE: PolyOxyethylene lauryl Ether.
[7]JGB: Janus Green B.

References:

Ivan, M., Dulmet, B., Martin, G., Abbe, P., Robert, L., Ballandras, S. (21-24 may 2012), A new electrostatically-excited silicon structure for CMUT and TE-mode resonators and sensing applications, Proc. 2012 IEEE *International Frequency Control Symposium.*, Baltimore, MD, USA, DOI: 10.1109/FCS.2012.6243724.

Rousseau, M. (2009), Impact des technologies d'intégration 3D sur les performances des composants CMOS (Doctoral dissertation, Université Paul Sabatier-Toulouse III).

Laermer, F., & Schilp, A. (1996), Method of anisotropically etching silicon, *U.S. Patent and Trademark Office.*, U.S. Patent No. 5,501,893. Washington, DC.

Laermer, F., Franssila, S., Sainiemi, L., & Kolari, K. (2010). Deep Reactive Ion Etching. Handbook of silicon based MEMS materials and technologies, 349-374.

B. Kim et D. Cho. (1999), Aqueous KOH etching of silicon(100)-etch characteristics and compensation methods for convex corners, *Journal of Electrochemical Society.*, 145 (7), pages 2499–2508.

P. Garrou, C. Bower, P. Ramm. (2008), *Handbook of 3D Integration*, volume 1 – 1st Edition. Weinheim: WILEY-VCH Verlag GmbH & Co. KGaA, 269 p.

Dixit, P., & Miao, J. (2008), High aspect ratio vertical through-vias for 3D MEMS packaging applications by optimized three-step deep RIE, *Journal of The Electrochemical Society.*, 155(2), H85-H91.

C. Chang et al., (2004), Trench filling characteristics of low stress TEOS/ozone oxide deposited by PECVD and SACVD, *Microsystem Technologies.*, 10 pp 97-102.

S.X. Zhang et al., (2005), Characterization of copper-to-silicon diffusion for the application of 3D packaging with through-silicon vias, *Proceedings of the Electronics Packaging Technology Conference*.

Establishment of Optimized Metallic Contacts on Porous Silicon for Thermoelectric Applications

O. Abbes,[1,*] A. Melhem,[1] K. Snabi,[1] C. Leborgne,[1] N. Semmar,[1]

[1]GREMI CNRS-Université d'Orléans, 14 Rue d'Issoudun, 45067 Orléans, France

Abstract: While the world's need of energy is rising with a decrease of fossil fuel supplies, it becomes crucial to develop smart materials that can supply clean and sustainable energy to meet the needs of the future. Thermoelectric materials are currently investigated as a promising pathway, they allow the conversion of temperature gradients into electricity, which provides power generation without refrigerant or moving parts. During last years, nanostructured silicon demonstrated a great potential to ameliorate thermoelectric figure of merit *ZT* (Lee *et al.,* 2008). In addition, porous silicon (por-Si) exhibits interesting properties, such as good features of electroluminescence and photoluminescence in the visible and IR spectra (Hamadeh *et al.,* 2008 and Fauchet *et al.,* 1996). A lot of effort has been devoted to boost the material's figure of merit, however, in a realistic device, metallic contacts are needed to extract electricity. Those contacts could gradually lower the resulting current, in the case of high electrical contact resistivity. Therefore, optimizing the metallic contacts grown on Silicon is of a high interest, toward their integration in thermoelectric applications. For example, in Complementary Metal-Oxide-Semiconductor (CMOS) technology, transition-metal silicides are used as contacts between metal interconnects and the Si (source, drain, and gate of the transistors).

Silicides offer major advantages such as contact resistance as well as excellent process compatibility with the standard Si technology. The production of silicides occurs during the reaction between a thin metal film and the Si thanks to the Salicide (Self-aligned silicide) process. The contact used nowadays, is the Ni monosilicide (NiSi), but PtSi is presented as a very good candidate to be used as a realistic contact.

In this work we present a study of the effect of several metallic contacts on the figure of merit, using a new process, and comparing the different factors influencing the electrical and thermal conductivities. Besides, a thermoelectric micro-generator was produced, and several masks were used in order to optimize metallic contacts on thermoelectric elements (Figure 1).

Si substrates were cleaved from Si(001) epi-ready wafers, the chemical cleaning of Si surfaces was done in two steps: the first was the rinsing in acetone and ethanol solvents to eliminate hydrocarbon contaminants due to storage of the substrates in air ambient. The next step was etching the contaminated Si native oxide layer in a diluted HF solution (10%) for several minutes. These cleaning steps of substrates was done prior to their introduction into the deposition chamber of the PECS set-up, exhibiting a base pressure better than 2.10-6 Torr, and equipped with high purity Ni and Pt charges (minimum of 99.99 wt. %).

Keywords: thermoelectricity, metallic contacts, porous Silicon, figure of merit, thermal conductivity, electrical resistivity.
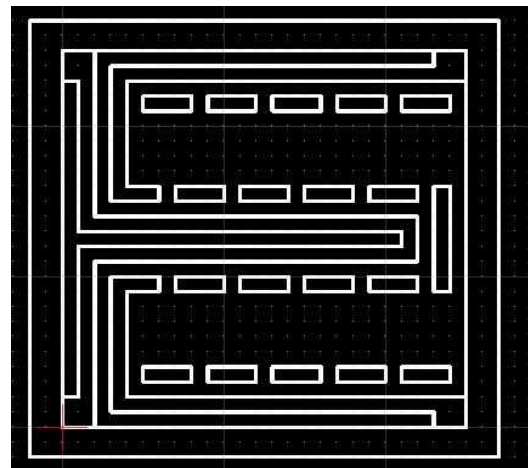
Figure 1: Figure illustrating the mask used in order to realize low resistive contacts on thermoelectric elements.

References:

Lee, J.H., Galli, G.A., Grossman, J.C., (2008) Nano-porous Si as an Efficient Thermoelectric Material, *Nano Letters*, 8, 3750-3754.

Hamadeh, H., Naddaf, M., Jazmati, A., (2008) Near infrared photoluminescence properties of porous silicon prepared under the influence of light illumination, *Journal of Physics D: Appl. Phys.*, 2008, 41, 245108.

Fauchet, P. M., (1996) Photoluminescence and electroluminescence from porous silicon, *Journal of Luminescence,* 70, 294-309.

Formation of magnetic phases by reactive diffusion between Mn and Ge for Spintronic Applications

O. Abbes,[1,*] A. Portavoce,[2] C. Girardeaux,[2] L. Michez,[3] and V. Le Thanh,[3]

[1]GREMI CNRS-Université d'Orléans, 14 Rue d'Issoudun, 45067 Orléans, France

[2]Aix-Marseille Université, CNRS, IM2NP-UMR 6242, Saint Jérome Case 142, 13397 Marseille, France

[3]Aix-Marseille Université, CNRS, CINaM-UMR 7325, Luminy Case 913, 13288 Marseille, France

Abstract: The synthesis of an epitaxial ferromagnetic silicide or germanide, exhibiting a high Curie temperature, is an important issue in order to efficiently inject spin-polarized currents into standard semiconductors (Dietl *et al.,* 2010). Among the different compounds, the Mn-Ge system presents a particular interest since it provides many phases with different magnetic properties. The most interesting phase is the intermetallic phase Mn_5Ge_3, which has been shown to epitaxially grow on germanium (Olive Mendez *et al.,* 2008) and has a Curie temperature at room temperature (Sawatzky *et al.,* 1971). Hence, it is opening the road for spin injection into group IV semiconductors. The phase diagram of the bulk Mn-Ge system contains a number of phases: $Mn_{3.4}Ge$, Mn_5Ge_2, Mn_7Ge_3, Mn_2Ge, Mn_5Ge_3 and $Mn_{11}Ge_8$, but data on thin films in the Mn-Ge system are relatively scarce. Therefore studying the phase formation sequence is of high interest. Furthermore, the current microelectronic technology uses the self-aligned silicide (SALISIDE) process (Chen *et al.,* 2008), to establish silicide contacts on silicon by solid state reaction. In our case, the reaction between a thin Mn metal layer and the germanium substrate gives a phase formation sequence of only some Mn germanides. In fig. 1, we present First results of in-situ X-ray diffraction measured during thermal annealing of 50 nm thick Mn layer deposited on 150 nm amorphous Ge are presented (Figure 1). The annealing temperature range was from 30 °C to 280 °C. These in-situ XRD measurements indicate that the Mn layer is stable on the Ge film until a temperature of about 130 °C, beyond which Mn starts to be consumed. The first phase to be observed is the Mn_5Ge_3 one, which appears in the phase sequence diagram. After that, at about 210 °C, we observe peaks characteristic of the $Mn_{11}Ge_8$ phase.

Numerous characterization techniques, including in-situ X-Ray Diffraction (XRD), Atomic Force Microscopy (AFM), and Transmission Electron Microscopy (TEM), were combined to study the sequential formation of Mn-Ge phases during reactive diffusion.

A 120 nm thick SiO2 oxide grown on Si(100) was used as substrates, which served as support for amorphous Ge deposition. The substrates were cleaned chemically with an ultrasonic rinsing in etha-nol and acetone, in order to eliminate hydrocarbon contaminants, prior to their introduction into the deposition chamber. This chamber exhibits a base pressure better than 5.10-9 mbar equipped with an evaporator set-up and high purity Mn and Ge charges (~ 99.999 wt.%). By the mean of electron beam evaporation, a 150 nm thick film of amorphous Ge film (a-Ge) was first deposited, than 50 nm thick Mn layer topped the sample. Both depositions were executed at room temperature, with a rate of 0.2 nm/s. X-Ray Reflectivity permitted to determine the thicknesses of the Mn and Ge layers.
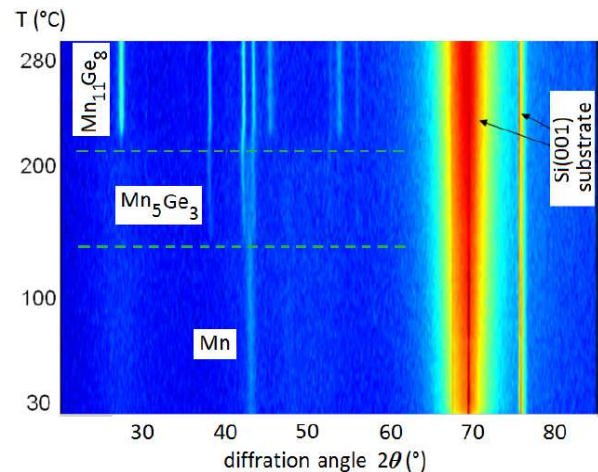
Figure 1: Figure illustrating the planar view of diffraction peaks corresponding to sequential formation of Mn_5Ge_3 and $Mn_{11}Ge_8$ during thermal annealing reaction of 50 nm thick Mn film with 150 nm thick film of amorphous Ge deposited on $SiO_2/Si(001)$ substrate.

References:

Dietl T. (2010), A ten-year perspective on dilute magnetic semiconductors and oxides. *Nature Mater.* 9, 965-974.

Olive-Mendez S. F., Spiesser A., Michez L. A., Le Thanh V., Glachant A., Derrien J., Devillers T., Barski A., Jamet M. (2008), Epitaxial growth of Mn_5Ge_3/Ge(111) heterostructures for spin injection. *Thin Solid Films,* 517, 191.

Sawatzky E., (1971), Magneto‑Optical Properties of Sputtered Mn_5Ge_3 Films. *J. Appl. Phys.* 42, 1706.

Chen Y. N., Lippitt M. W., Chew H. Z., Moller W. M., (2003), Manufacturing enhancements for CoSi2 self-aligned silicide at the 0.12-μm CMOS technology node. *IEEE Trans. Electron Devices* 50, 2120-5.

Strength and Ductility of SGFRP Confined Concrete

Q. Hussain[1], L. Lalin[1] and A. Pimanmas[2]

[1]Graduate Student, Sirindhorn International Institute of Technology, Thammasat University

Emails: ebbadat@hotmail.com, lamlalin08@gmail.com

[2]Associate Professor, Sirindhorn International Institute of Technology, Thammasat University

Email: amorn@siit.tu.ac.th

Abstract: During last decade, external confinement of concrete using different uni-directional fiber reinforced polymer composites (FRP) is proved successful to enhance strength and ductility of concrete. FRP are high strength and low weight compared with steel and concrete. In contrast to the uni-directional FRP composites, sprayed glass fiber reinforced polymer composites (SGFRP) are comprised of randomly distributed chopped fibers. In SGFRP, the fibers are sprayed using spraying and pumping equipment.

In this study the behavior of concrete confined with SGFRP is evaluated in terms of strength and ductility enhancement. Both circular and square concrete cylinders externally strengthened with different SGFRP thickness and fiber length in SGFRP were investigated. A total of 20 concrete cylinders including SGFRP strengthened and un-strengthened were tested under axial compression loading. The experimental investigations clearly show that SGFRP are significantly effective to enhance strength and ductility of concrete. There is found momentous increase in load carrying capacity and ductility with an increase in thickness of SGFRP. However increase in strength and ductility is more significant for circular specimens compared with square specimens.

Key words: SGFRP; strengthening; cylinders; strength; ductility.

1. Introduction: In recent years, strengthening of concrete columns by wrapping and bonding of fiber reinforced plastic (FRP) sheets, straps, belts or procured shells around the column has become increasing popular. Nanni and Bradford (1995) investigated the behavior of FRP encased concrete with three different types of fiber wraps; namely, braided aramid FRP tape, filament wound E-glass, and preformed hybrid glass-aramid FRP shells. Dai et al. 2012 has investigated the behavior of concrete confined by FRP jackets (PET and PEN) with a large rupture strain (LRS). LRS FRPs can enhance the ductility of concrete substantially with a much smaller associated increase in compressive strength compared with low strain fibers. In addition to the experimental investigations a large database is available in which models are proposed to predict the compressive strength of concrete confined by uni-directional FRP (Lam and Teng 2002).

In contrast to the lamination and wrapping techniques, a new technique using sprayed glass fiber reinforced polymer composites (SGFRP) has recently been used to strengthen RC structural members (Banthia and Boyd 2000). In the SGFRP technique, chopped fibers of a controlled length are sprayed with a polymer matrix using a spray gun that is mounted with a chopper unit and epoxy containers. Once the sprayed fibers reach the required thickness, a ribbed aluminium roller is rolled across the sprayed fibers to remove any entrapped air. The result is a mixture of randomly distributed chopped fibers with resin. This paper presents an experimental study on behavior of concrete confined with SGFRP. Plain concrete specimens of circular and square shape were strengthened with different thickness and fiber length in SGFRP and tested under uni-axial compression loading.

2. Material properties

2.1 Concrete Mixture

A single concrete mixture (cement = 265 Kg/m^3, sand = 689 Kg/m^3, gravels = 1086 Kg/m^3, water = 172 Kg/m$^{3)}$ was sued to achieve the desired range of unconfined compressive concrete strength (28 days target strength = 25 MPa).

2.2 SGFRP Material

The glass fiber roving used in this study was an assembled glass-fiber manufactured by Jushi Group Co., LTD. The resin system that was used to spray glass fiber over the concrete surface was the polyester resin made of two parts, resin and hardener. The resin and hardner was manufactured by the QualiPoly Chemical Corporation, Taiwan and AkzoNobel Polymer Chemicals, respectively. The mechanical properties of SGFRP material, including tensile strength and modulus were obtained through tensile testing of flat coupons. The tensile coupons where prepared and tested following the ASTM standards (ASTM D638, 1999) with slight modifications in the size. Prior to the testing, strain gauges were glued at the middle to record strains. The tensile coupons were cut from SGFRP rectangular of 3 mm and 5 mm. The sheets were prepared by spraying glass fibers onto the planar surface. For both 3 mm and 5 mm SGFRP, a total of 10 tensile strips were prepared for tensile testing. The density and the fiber-volume fraction were measured using ASTM methods D792 and D2584 (ASTM D792, 2000; ASTM D2584, 2002). [Tensile strength = 63-75 MPa, tensile modulus = 8.4-9.5, density 1.43-1.47 and fiber volume fraction = 30-40%].

3. Specimen Preparation

Two series of experiments were performed to investigate the behavior of plain concrete circular and square cylinders confined by SGFRP.100 mm-diameter by 200 mm-height of cylindrical specimens and 100 mm by 100 mm in width and depth along with 200 mm-height of square specimens were used in this study. Prior to the SGFRP strengthening, the corners of square columns were rounded off by corner radii of 20 mm to avoid rupture of SGFRP at corners. Further in this experimental program, the surface of circular and square cylinders was roughened using a chisel and a hammer prior to the application of SGFRP (Figure 1) to increase the bond strength of SGFRP to concrete surface. Details of test matrix are given in the Table 1.

Figure 1: Typical roughened surface of specimens

Table 1: Test matrix

	thickness (mm)	length (mm)	numbers

4. SGFRP Strengthening

After 28 days of curing, SGFRP were applied to the specimens by spraying glass fiber with polyester resin. Prior to the SGFRP strengthening an arrangement of steel stand and end plates were prepared to continuously rotate the cylinders during the spray process (Figure 2). During SGFRP spraying process skilled labor continuously monitored and controlled the fiber loading and thickness of applied SFRP. Once glass SFRP was sprayed, an aluminum ribbed roller was used to remove the entrapped air and to obtain uniform thickness of sprayed fiber.

Figure 2: SGFRP strengthenin process

5. Test Setup and procedure

The both circular and square specimens were loaded under a motonic uniaxial compression load up to failure. The compressive load was applied at a rate of 0.24 MPa/s and was recorded with an automatic data acquisition system. Axial and lateral strains were recorded using three different vertical and horizontal linear variable differential transducers (LVDTs), respectively. Prior to testing, all SGFRP strengthened cylinders as well as the un-strengthened cylinders were capped with sulfur mortat at both ends. Additionally, in SGFRP strengthened specimens, a steel plate of 5mm thickness were provided in between sulfur mortar and loading plate to avoid compression load over the SGFRP shell.

6. The Experimental stress-strain relationship

The experimental results are presented by the axial stress strain relationships. The stress strain behavior of SGFRP confined circular and square cylinders along with un-strengthened specimens are presented in the figures 3-5. The experimental results are summarized in the Table 2. As seen in these figures, both compressive strength and ultimate axial strain are increased significantly as a result of SGFRP Strengthening.

6.1 Effect of SGFRP Thickness
6.1.1 Circular specimen

For SGFRP strengthened circular specimens (fiber length of 13 mm) with the SGFRP thickness of 3 mm, the compressive strength and ductility increased 130% and 278%, respectively while those of 229% and 506% increased for the specimens with SGFRP thickness of 6 mm. In SGFRP strengthened circular specimens (fiber length of 26 mm) with the SGRP thickness of 3mm, the compressive strength and ductility increased up to 156% and 301%, respectively while those of 259% and 536% increased for the specimens strengthened with higher thickness of 6mm. Stress-strain curves of circular specimens with different thickness are shown in Figure 3.

6.1.2 Square specimen

For SGFRP strengthened square specimens (fiber length of 13 mm), 89% and 175% increase in strength and ductility were observed with thinner SGFRP thickness (t = 3 mm), while 188% and 258% increases in strength and ductility were recorded by the thicker SGFRP thickness i.e. 6 mm. In SGFRP strengthened with the fiber length of 26 mm square specimens, 91% and 203% increases in strength and ductility were observed with the thin SGFRP while the thick SGFRP increased them by 206% and 308%, respectively. Figure 4 shows the comparison of the stress-strain curves of square specimens with different thickness.

Table 2: Experimental results

Specimen	f_{co} (MPa)	f_{cc} (MPa)

6.2 Effect of fiber length

6.2.1 Circular specimen

The typical stress-strain curves of circular specimens with two different lengths of 13 and 26 mm (SGFRP thickness of 6 mm) are presented in figure 3 to investigate the influence of fiber length on the strength and ductility of concrete. 229% and 506% increases in strength and ductility, respectively, were observed with the SGFRP have short fibers (*l=13mm*), while 259% and 536% increases in those of specimens strengthened with long fibers (*l= 26mm*).

6.2.2 Square specimen

The typical stress-strain curves of square specimens with two different lengths of 13 and 26 mm are presented in figure 4 to investigate the influence of fiber length on the load strength and ductility of concrete. 188% and 258% increases in strength and ductility, respectively, were observed in specimens strengthened with short fibers (l=13mm), while 206% and 308% increases in those where recorded by the SGFRP with long fibers (l= 26mm) in figure 4.

6.3 Effect of shape

The typical stress-strain curves of specimens strengthened with 6 mm SGFRP for both circular and square shape are shown in the figure 5. It is evident that efficiency of SGFRP strengthening is higher for circular specimens compared with square ones.
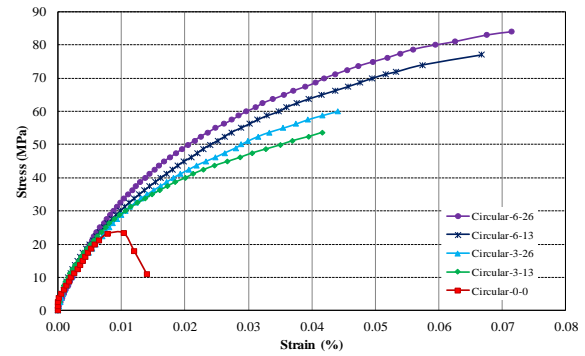

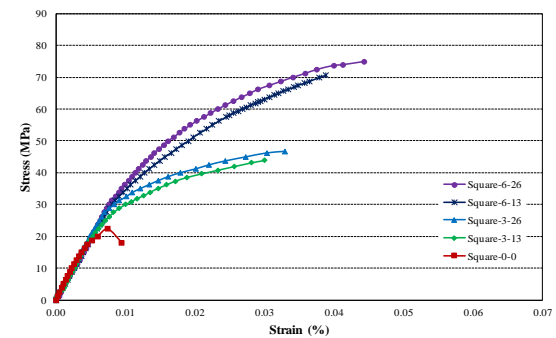Figure 3: Stress-strain curves of circular specimen (effect of thickness)

Figure 4: Stress-strain curves of square specimens (effect of thickness)
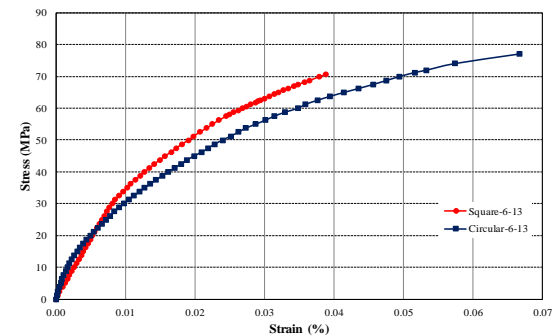

Figure 5: Stress-strain curves of circular and square specimens (effect of specimen shape)

In figure 5, 229% and 506% increases in strength and ductility respectively were recorded for circular specimens while 188% and 258% increases in those were observed for square specimens.

7. Failure Modes

The un-strengthened circular specimens were failed in typical manner by crushing of the concrete at peak load. Whereas, SGFRP strengthened circular specimens were failed in three different modes; 1) vertical rupture, 2) partially inclined and 3) inclined ruptures (Figure 6). While all SGFRP strengthened square specimens were failed by rupture of SGFRP at the corners(Figure 7). The final failure was sudden and explosive preceded by moderate snapping sounds in both shapes.

8. Comparison of Analytical predictions with experimental data

The analytical expressions proposed by Toutanji (1999) and Shehata et al.(2002) for uni-directional FRP confined concrete were utilized here for the prediction of compressive strength of circular and square specimens confined with SGFRP, respectively. These expressions are given in the equations 1 and 2.

For circular specimen

$$\frac{f'_{cc}}{f'_{co}} = 1 + 3.5 \left(\frac{f_l}{f'_{co}} \right)^{0.85} \qquad (1)$$

For square specimen

$$\frac{f'_{cc}}{f'_{co}} = 1 + 0.85 \frac{f_l}{f'_{co}} \qquad (2)$$

Where f'_{cc} and f'_{co} are compressive strengths of confined and un-confined concrete, respectively, and f_l is the lateral confining pressure provided by FRP.

$$f_l = \frac{2 f_{FRP} t}{D} \qquad (3)$$

Where f_{FRP} is the tensile strength of the FRP in the hoop direction, t is the total thickness of the FRP and D is the diameter of the core concrete i.e. confined circular concrete section. The comparison of analytical and experimental results is shown in the Table 3. As seen in the Table 3 that both models are close to predict the compressive strength of the concrete confined with SGFRP however both models are under estimating the predicted values.

7. Conclusions

This paper present the study on behavior of concrete confined with SGFRP. Based on experimental results it can be concluded that;

1. The compressive strength and ductility are enhanced significantly when the cylinders are strengthened with SGFRP.

2. The analytical expressions proposed by Toutanji (1999) and Shehata et al.(2002) for FRP confined produces close results for circular and square SGFRP confined concrete specimens, respectively.

Table 3: Comparison of results

	f'_{cc} (MPa)	f'_{cc} (MPa)

vertical rupture   Partially inclined   inclined ruptures

Figure 6: Failure mode of circule specimens

Figure 7: Failure mode of square specimens

References:

Nanni, A and Bradford, NM. (1995) FRP Jacketed concrete under uniaxial compression, *Const. Build. Mater.,* 9(2), 115-124.

Dai J., Bai Y., and Teng JG. (2012) Behavior and modeling of concrete confined with FRP composites of large deformability. *J Compos Constr.* 2012;15(6):963-73.

Lam, L., and Teng, JG. (2002) Strength models for fiber-reinforced plastic-confined concrete. *J Struct Eng.,* 128(5), 612-23.

Banthia, N. and Boyd AJ (2000). Sprayed fiber-reinforced polymers for repairs. *Can J Civ Eng* .,27(5):907-15.

ASTM D638 (1999). Standard Test Method for Tensile Properties of Plastics. ASTM International, 13 pages.

ASTM D792 (2000). Standard test method for density and specific gravity (relative density) of plastics by displacement. ASTM International, 6 pages.

ASTM D2584 (2002). Standard test method for ignition loss of cured reinforced resins. ASTM International, 3 pages.

Toutanji, HA., (1999) Stress-strain characteristics of concrete columns externally confined with advanced fiber composite sheets. *ACI Mater J,* 96(3):397-404.

Shehata, LAEM., Carneiro, LAV., and Shehata, LCD., (2002) Strength of short concrete columns confined with CFRP sheets. *Mater Struct.* 35(1):50-58.

Smart Focused-Ion-Beam-fabricated Nanostructures for Improving Surface Enhanced Raman Scattering on Trace Detection of Single Molecules

Kundan Sivashanmugan[1], Jiunn-Der Liao[1,2,], Chih-Kai Yao[1]*

[1] Department of Materials Science and Engineering, [2] Center for Micro/Nano Science and Technology, National Cheng Kung University, 1 University Road, Tainan 70101, Taiwan.
[*] Corresponding author: jdliao@mail.ncku.edu.tw

Abstract

In this work, Au and Au/Ag nanorod arrays (*fib*Au_NR and *fib*Au/Ag_NR) were fabricated by focused ion beam (FIB) with low and high ion energy. The formation of $AuGa_2$ alloys on *fib*Au_NR was controlled by ion energy and temperature treatment. On the other hand, *fib*Au/Ag_NR embedded nanovoids were generated with an increase in stress mostly caused by the effects of oxidation and heat expansion. In addition, the nanovoids formed in the embedded Ag layer. However, Au and Ag interface have different diffusion rates of the metal atoms and temperature treatment where atomic diffusion is possible; the interface could be moved and produce the alloys and voids in Au/Ag. Moreover, $AuGa_2$ on *fib*Au_NRs was anticipated to increase the localized surface plasmon resonance (LSPR) due to the matched photon energy between Au and $AuGa_2$. The embedded nanovoids increased the available space for the interaction an analyses with laser light and a strong electromagnetic (EM) field effect is generated in and around these nanovoids, creating LSPR. The *fib*Au_NR and *fib*Au/Ag_NR Surface-enhanced Raman scattering (SERS) properties were investigated using crystal violet as molecular test probes. The enhancement factor reached up to 10^7. Furthermore, an optimized *fib*Au_NR SERS-active substrate was applied to the detection of melamine cyanurate (MEL-CA) in milk solution at low concentration (pM). Results show that SERS-active *fib*Au_NR have potential for rapidly detecting low-concentration samples.

Keywords: Focused ion beam; Nanorods; Surface-enhanced Raman scattering; Crystal violet; Melamine-cyanurate

Introduction

SERS is a label-free and extremely selective spectroscopic tool for analyzing a wide variety of chemical or biological species owing to its excellent sensitivity to molecular vibrations (*Nusz et al.,*). The effect of SERS is mainly attributed to two primary mechanisms, namely chemical and EM effects. The interaction of noble metal nanoparticles (NPs) or nanostructure (NSs) with a laser with a constant wavelength can result in a collective oscillation caused by an excitation of conduction electrons and a subsequent electric field in the vicinity of NPs or NSs owing to the induction of LSPR. The frequency of LSPR strictly depends on the composition and geometry of NPs or NSs as well as the refractive index of the localized environment and that allows single molecule detection (*Campion et al.,*). The optical properties of FIB-fabricated NSs may be suitable for Raman-active substrates (*Sivashanmugan et al.,*). There still occur some drawbacks to NSs for use as photonic components. For example, FIB-fabricated NSs are strongly influenced by the residual Ga concentration and have a limited aspect ratio (*Tao et al.,*). In the present work, *fib*Au_NR and *fib*Au/Ag_NR SERS-active substrates were fabricated using FIB and applied to the detection of contaminant molecules at a low concentration in milk. The SERS-active

substrates had high enhancement due to a large LSPR effect from the arrangement of hot-spot arrays.

Detection of melamine cyanurate in milk
The rapid detection and identification of toxic substances in food or the environment is one of the most important applications of SERS analysis. In order to understand the interaction of MEL with CA was studied at a Raman laser wavelength of 785 nm. The spectrum of MEL-CA exhibits solid peaks at 680, 705, and 988 cm^{-1}. For SERS-active *fib*Au_NR sample even a small amount of MEL-CA produced strong Raman signals at 686 to 705 cm^{-1}, assigned to ring breathing mode II. The peak area increases with increasing concentration. The reproducibility of *fib*Au_NR sample was confirmed at 25 sampling positions. The SERS spectra exhibit fairly consistent peak intensities. As a consequence, the effect of hot spot (figure 1) uniformly distributed upon *fib*Au_NRs sample was anticipated. MEL-CA was detected on *fib*Au_NR sample even at 10^{-12} M. Therefore, the proposed substrates are promising for the field detection of MEL-CA in milk products.
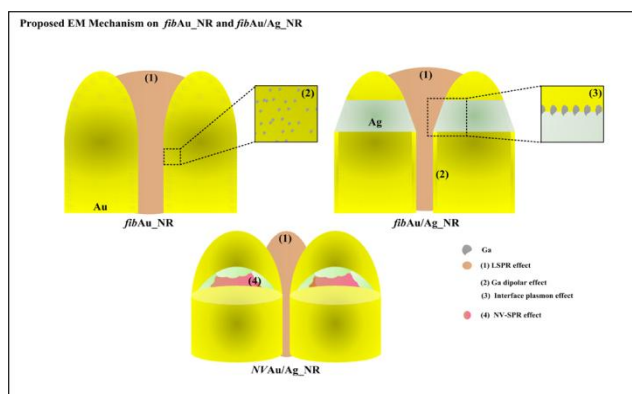
Figure 1 Brief description of proposed EM mechanism for *fib*Au_NR and *fib*Au/Ag_NR.

Conclusion
The *fib*Au_NR samples had high SERS activity for MEL-CA detection, and thus have potential for the ultrasensitive measurement of MEL-CA in milk solution.

References:

Nusz, G. J., Curry, A. C., Marinakos, S. M., Wax, A., Chilkoti, A. (2009), Rational selection of gold nanorod geometry for label-free plasmonic biosensors. *ACS Nano* 3, 795-806.

Campion, A., Kambhampati, P. (1998), Surface-enhanced Raman scattering. *Chem. Soc. Rev.* 27, 241-250.

Sivashanmugan, K., Liao, J. D., You, J. W., Wu, C. L. (2013), Focused ion beam fabricated Au/Ag multilayered nanorod array as SERS-active substrate for virus strain detection. *Sens. Act. B: Chem.* 181, 361-367.

Tao, H. H., Ren, C., Feng, S., Liu, Y. Z., Li, Z. Y., Cheng, B. Y., Zhang, D. Z., Jin, A. Z. (2007), Optical improvement of photonic devices fabricated by Ga + focused ion beam micromachining. *J. Vac. Sci.Technol. B* 25, 1609 -1614.

Nanostructured Metal oxides: Catalyst-free Synthesis, Characterization and Integration with MEMS Processing for Gas Sensor

S. Chandra[*] and B. Behera
Centre for Applied Research in Electronics, Indian Institute of Technology Delhi,
HauzKhas, New Delhi-110016, India
[*] E-mail: schandra@care.iitd.ernet.in

Abstract. In the present work, we report a novel catalyst-free low cost technique for synthesis of nanostructured ZnO and its integration with MEMS processing to demonstrate a sensor for VOC detection. For this purpose, thin films of Zn were prepared by RF sputtering method on oxidized silicon substrates. These were then subjected to an annealing cycle in oxidizing ambient in the temperature range 400-550 C in a horizontal tube furnace resulting in the growth of nanostructured ZnO. The effect of parameters such as initial Zn film thickness, sputtering parameters (RF power, pressure), annealing time, ambient (dry O_2, wet O_2, atmospheric air, synthetic air, wet N_2 etc.) were investigated in detail on the nature of nanostructures formed by the annealing step. The process was optimized to yield long nanowires of ZnO. The characterization included: Scanning Electron Microscopy (SEM) and X-ray diffraction (XRD) studies on the synthesized nanostructured ZnO material. A complete sensor incorporating an on-chip heater and inter digital electrode (IDE) for sensing on a MEMS platform using bulk micromachining is demonstrated.

Introduction: Thin films of metal oxides (such as tin oxide, indium tin oxide, zinc oxide, tungsten oxide etc.) are potential candidates for gas and VOC (volatile organic compound) sensing applications (Branna G). In nanostructured form, these materials are more sensitive as gas sensor due to their much higher surface area-to-volume ratio compared to their corresponding thin films. For efficient operation, it is a requirement that the gas sensor, incorporating metal oxide material, is heated upto 350 °C. The power consumption is an important issue in sensor design. Sensors made on suspended thin diaphragm of silicon using MEMS (Micro-Electro-Mechanical-Systems) technologies consume much less power due to thermal isolation. There is thus certain advantage in using nanostructured metal oxides integrated with MEMS technologies for gas and VOC sensing (Gong et al). There is a challenge in developing these MEMS based sensors using low cost and easy-to-manufacture technologies (Pandya et al. and Ahne al.).

Results and discussions: The RF magnetron sputtering process was performed for deposition of Zn films (thickness: ~130 nm). The sputtering was carried out at 5 mTorr of Ar pressure, 50 W of RF power for 30 minutes. The target to substrate spacing was 10 cm. These samples were thermally oxidized in N_2 mixed water vapour environment (40%, 70% and 100% Relative humidity (RH)) for 1h at 500 °C. The SEM images of these post oxidized samples are shown in Fig. 1 (a), (b) and (c)
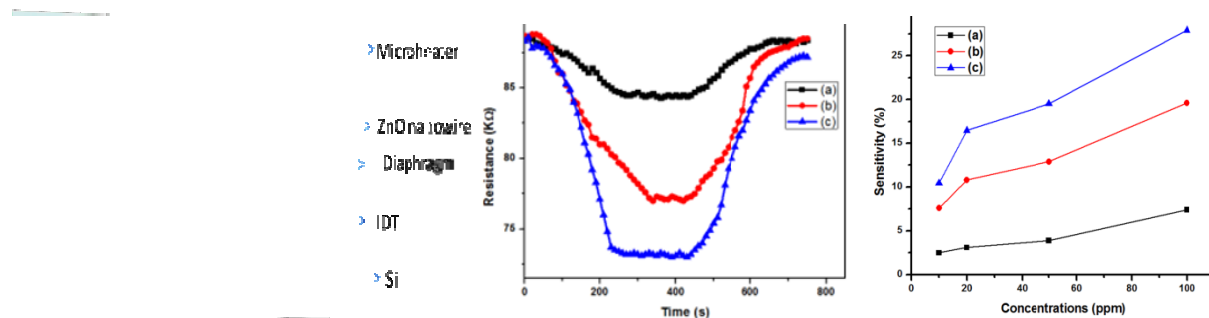

.
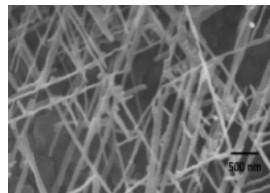
Fig. 1 SEM images of three different types of ZnO nanostructures synthesized at (a) 40 % RH, (b) 70 %(c) 100% RH and (d) XRD pattern of ZnO nanowires synthesized in 100% RH conditions

Fig. 1(d) shows XRD pattern of ZnO nanowires grown on oxidized Si substrate. These nanowires were found to be polycrystalline with (100) and (101) as dominant peaks. Thus it can be concluded that, the

oxidizing environment strongly affects the structural growth of ZnO nanostructures. At 100% RH environment, the nanowires are branched, long and dense.

It was found that ZnO nanowires were less sensitive towards VOCs at room temperature and thus heating of sensing layer was a necessary requirement. For lower power consumptions, micro sized hotplate was designed and fabricated over thin Si diaphragm. The schematic diagram of MEMS based sensor is depicted in Fig. 2 (a). The micro-heater temperature coefficient of resistance was calibrated for temperature measurement. The nanostructures obtained in different RH conditions were tested for 10-100 ppm of ethanol at 100 °C and results are presented in Fig. 2(c)

Fig. 2(a) Schematic diagram of MEMS based gas sensor (b) Change in resistance for 50 ppm of ethanol tested at 100 °C for three different types of ZnO nanostructures synthesized at (a) 40% RH, (b) 70% (c) 100% RH conditions and**(c)** Sensitivity of10-100 ppm of ethanol for same nanostructures.

The sensitivity (defined as (Ra- Rg)/Rg, where Ra and Rg are the electrical resistance values in atmospheric environment and in ethanol environment respectively) increases with nanostructures obtained in increasing RH condition i.e. with dense and uniformly dispersed nanowires. At 100 °C operating temperature, the reaction mechanism at sensing layer can be explained as follows:

$$O_2(g) \rightarrow O_2^-(ads), C_2H_5OH(g) + O_2^- ads) \rightarrow CH_3 HO + _2O + e^-$$
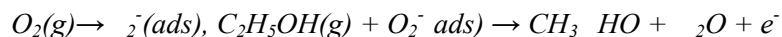
The electrons generated during this reaction are responsible for decreasing in resistance of ZnO nanowire measured through IDT (inter digited electrode) structure. When the Debye length is in the range of ZnO nanostructures size (in this case diameter of nanowire), the entire ZnO will be treated as a electron depleted region and hence the electron activity drastically rises. Thus Nano structured ZnO (in the case of dense, branched and long nanowires) have higher sensitivity over other two.

References

Eranna G 2011 *Metal Oxide Nanostructures as Gas Sensing Devices* (Boca Raton, FL: CRC Press)

Gong J, Chen Q, Fei W and Seal S 2004 Micromachinednanocrystalline SnO₂ chemical gas sensors for electronic nose Sensor Actuators B Chem. 102 17–25

Pandya H J, Chandra S and Vyas A L, 2012 Integration of ZnO nanostructures with MEMS for ethanol sensor *Sensors Actuators B Chem.*161**,** 923–8

Ahn M W, Park KS, Heo J H, Kim DW, Choi KJ, and Park JG, 2009 On-chip fabrication of ZnO-nanowire gas sensor with high gas sensitivity*Sensors Actuators B Chem.* 138, 168.

Micro-scale Piezoelectric Harvester from Fluid Flow at Low Velocity

Krit Koyvanich [1], Pruittikorn Smithmaitrie [2], Nantankan Muensit [1,*]

ABSTRACT

We have developed a newly designed energy harvester for the utilization of energy from water flow with vortices based on cantilever beam energy conversion. It converts fluid flow energy into electrical energy through the vibration of a piezoelectric film. The full wave oscillation of the piezoelectric film was induced by vortex induced vibration phenomena to the piezoelectric film sheet (polyvinylidene fluoride, PVDF). Variations in the vibration frequencies have been created by pressure fluctuations in vortices of the fluid flow from the bluff body. The PVDF attachment obtained the oscillation from flow kinetic energy. The coupling mathematical model of energy harvesting technique and experimental data were established. Experiments were carried out to verify the validity of the numerical simulation results. It shows that the power output and the peak frequency obtained from the numerical analysis were in good agreement with the experimental results. This approach leads to the potential of hydropower harvesting and converting it into electrical energy for powering wireless devices. The micro-scale of the output power from this harvesting can be improved by increasing the piezoelectric constant of piezoelectric materials or by an optimization of the design harvesting process. Multiply arrays of this harvester together with a rectifier can be made available to be part of a hydropower harvesting devise placed into a flowing river.

**Keywords**: piezoelectric, fluid flow, PVDF, energy harvesting.

1. INTRODUCTION

Flow energy is readily available in the form of air and water streams for in and/or outside the building base. Energy conversion of ambient wind energy into electricity for wireless sensor networks (WSNs) have been explored by using small scale turbine systems [1]-[4]. However, complexity, a complicated fabrication, and high maintenance costs due to unfavorable viscous drag and baring loss are disadvantages. Moreover, piezoelectric materials propose the potential as a flow energy harvester by convert flow induced vibrations (FIV) or vortex induced vibrations (VIV) into electrical energy [5]. The designed harvester device in this work is proposed to show "eel/flag" motion based on an ultralow range of fluid velocity (<0.2 m/s). Generated powers of this device were estimated on possible harvesters' dimensions and experiments of flow harvesting setup, as well the computational simulation are calculated and the results discussed.

2. FLUID FLOW HARVESTING

The piezoelectric flag energy harvester consists of piezoelectric polymers attached behind a vortex generator (bluff body) in in small channel (pipe line) structure. Fluid-solid interaction induces AC voltage generation in the converter. An analytical VIV interacted to laminate film has been proposed by finite element methods (FEM), and the results are shown in **Figure**.**1**. Film's amplitude and frequency oscillation data have been obtained in various flow velocities by COMSOL multiphysics software. The combination of mechanical and piezoelectric equivalent circuits of the converter for electrical energy output is achieved by MATLAB Simulink. Physical and piezoelectric properties of film are presented in **Table 1**. Different flow velocities (U) and other properties of the elastic film, e.g. density, Poisson's ratio, Lame coefficient, have been used for FEM analysis.
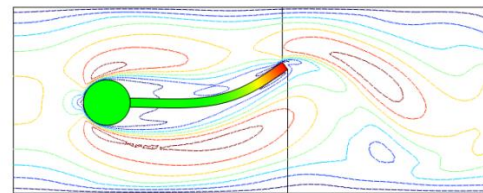
Figure 1: Contour diagram of the total displacement of film and velocity magnitude in the fluid **[6]**.

The fluid flow energy harvesting setup is consisting with power flow supply, converter, and measurement units. Water flow velocity has been controlled by a vale. Open voltage output ($V_{oc.}$) signals of the piezo film were detected by an oscilloscope. To calculate the electrical power generated (P) and the energy conversion coefficient of the device, principles to fluid flow and electrical AC power based calculations can be employed **[7]-[8]**.

Table 1: Piezoelectric, mechanical properties **[9]**, and the estimated power generated by PVDF.

The piezoelectric harvester generates random voltage amplitudes. On the other hand, the DC voltage amplitude depends on the fluid flow velocity generated. The maximum Voc. signal at low rang velocity that can be observed is about a micro watt. High frequency voltages of the harvested signal were from electromagnetic radiation of the measurement device. A low passed filter circuit is applied to the harvester unit to cut the not related frequencies off, which were over 30 Hz. A rectifier by a full wave bridge was added as well as a capacitor for energy storage. Energy management electronics must be matched to the sleep/measure/wake/transmit cycles to achieve maximum efficiency of the whole measurement system.

3. RESULTS AND DISCUSSIONS

This work presents an energy harvester, i.e. a micro-generator, utilizing fluid flow by using the piezoelectric principles. Although experiments were not performed at resonance frequency, the device can generate the f_s oscillation of an ambient system reaching resonance frequency by using a tailored fluid velocity of ~6.8 m/s. The Re number will be ~5,000 and the flow can reach unsteady-oscillating state in order to increase the output power. An outlook of possible river flow and small channel energy harvesting solutions for powering low power monitoring sensor nodes is given. In view of this conclusion, future research will focus on the developing of further physical factors as the distance to achieve maximum vortex power from the harvester and testing this experimentally in real river flow conditions. Power levels available by using the considered harvesting solutions will also be experimentally estimated as well as the optimization of the power management electronics.

4. ACKNOWLEDGMENTS

5. REFERENCES

[1] Priya, S., Myers, R., Vickers, M., and Kim, H. 2007. Small scale windmill. *Appl. Phys. Latt*. 90, 054106 (Jan. 2007), pp.1-3.

[2] Park, J.W., Jung, H.J., Jo, H., and Spencer, B.F. Jr., Feasibility Study of Micro-Wind Turbines for Powering Wireless Sensors on a Cable-Stayed Bridge, *Energ*. 5, (Sep. 2012), 3450-3464. **DOI:**10.3390/en5093450.

[3] Azevedo, J.A.R., Santos, F.E.S., Energy harvesting from wind and water for autonomous wireless sensor nodes, *IET Circuits Devices Syst*. 6, 6, (Aug. 2012), pp.413-420. **DOI:**10.1049/iet-cds.2011.0287.

[4] PRIYA, S., CHEN, C.T., FYE, D., and ZAHND, J., Piezoelectric Windmill: A Novel Solution to Remote Sensing, *Jpn. J. Appl. Phys*. 44, 3 (Dec. 2004), pp. L104–L107. **DOI:** 10.1143/JJAP.44.L104.

[5] Rao, K.M., and Manur, A.G., Modeling of Vortex Induced Vibration based Hydrokinetic Energy Converter, *IOSR-JEEE*, 6, 6 (Jul.-Aug. 2005), pp.26-31; **e-ISSN:** 2278-1676; **p-ISSN:** 2320-3331.

[6] Turek, S., and Hron, J., *Proposal for numerical benchmarking of fluid-structure interaction between an elastic object and laminar incompressible flow*, Institute for Applied Mathematics and Numerics, University of Dortmund, Dortmund, Germany. pp. 246-260. Web available:http://adhesion.ucd.ie/ccm/CCM_II_files/Hron%20Turek%20Benchmark.pdf

[7] White F.M.; Fluid Mechanics (4th eds.), McGraw-Hill international (eds.); **2003**

[8] Cook-Chennault, K.A., Thambi, N., and Sastry, A.M., Powering MEMS portable devices—a review of non-regenerative and regenerative power supply systems with special emphasis on piezoelectric energy harvesting systems, *Smart Mater. Struct*. **17**, (June 2008), 043001, pp. 1-33. **DOI**:10.1088/0964-1726/17/4/043001

[9] Piezo Film Sensors Technical Manual, Measurement Specialties, Inc., P/N: 1005663-1, **1999**. Web available: http://www.https://www.sparkfun.com/datasheets/Sensors/Flex/MSI-techman.pdf

Effect of electron beam on thermal, morphological and antioxidant properties of kraft lignin

N.RajeswaraRao,[1] T.Venkatappa Rao,[1*] SVS.Ramana Reddy,[1] B.Sanjeeva Rao[2]

[1]National Institute of Technology, Warangal, INDIA

[2]Govt. Degree College, Mulugu, Warangal, INDIA

Corresponding author Email: tvraokmm@yahoo.co.in

Abstract: Thermal, morphological and antioxidant properties of lignin irradiated with electron beam of doses 30, 60 and 90 kGy have been investigated by ESR, FITR, DSC, SEM and Spectrophotometer techniques. The absorption band at 1604cm^{-1} reveals the presence of conjugated structures whose concentration increases with the dose of irradiation. Glass transition temperature of lignin decreased abruptly at 90 kGy of dose and cracks were generated in lignin granules on EB irradiation. Antioxidant studies shows that the irradiated lignin with destructed particles and high conjugation exhibit high antioxidant activity compared to the unirradiated.

1. Introduction

Lignin, a natural polymer found in the cell walls of plants along with the other two major components, cellulose and hemicellulose. Lignin comprises 28% of the mass of wood-like plants. In wood, lignin consists of a family of phenyl-propane type polymers in a variety of structural units. In addition, lignin has a complex chemical functionality of carboxyl groups and alcohols [1]. In fact, due to its non-toxic nature, renewability and extreme versatility, lignin applications have been increasing in industry. The radiation induced modification of biopolymers is a feasible method to produce material or to tailor their usage. Electron beam (EB) irradiation is a promising green tool in this respect and optimized/alternative methods to utilize and to improve lignin as a precursor in a cost effective manner. The radioactive degradation of kraft lignin has been the subject of numerous investigations.

Barca et al [2] have reported that phenolic model compounds recognized as indigenous to the lignin structure which possess significant antioxidant property. Structures with conjugated double bonds in propyl side chains have higher antioxidant activities compared to structures with saturated side chains or isolated double bonds. Lignin also contains ortho-distributed phenolic groups. In addition, ortho-methoxy groups might provide stabilization to the incipient phenoxy radical formed by resonance structures.

In the present study, electron beam irradiation of different doses was applied to lignin. Under the treatment from an electron beam, lignin compounds are known to undergo several radical initiated reactions such as aryl hydroxylation, fragmentation and cleavage. These reactions leave the compound open to interaction with number of resins systems which have the capability to change the mechanical properties and biodegradability of resulting composite. In such cases it is necessarily important to study the properties of lignin such as radical stabilities, thermal properties and morphology on EB treatment which can effect composite properties. Further, lignin aromatic structures suggests that it is suited as a radical scavenger in existing commodity thermoplastics. Also there are limited number of papers dealing with EB irradiation of lignin as a source for antioxidant activity.

2. Material and Methods

Kraft lignin in the form of powder was purchased from *Sigma Aldrich*, USA. Three lignin sample packets were prepared for electron beam irradiation with optimum radiation doses i.e. 30, 60 and 90 kGy. The industrial electron beam accelerator is ILU-6 type, pulse linear accelerator from Board of Radiation and Isotope Technology, BARC, INDIA. In the present studies, the dose rate chosen is 5 kGy/pass. Chemicals like 1,1-diphenyl-2-picrylhydrazyl (DPPH), Methanol, L-ascorbic acid, trichloroacetic acid (TCA) and other reagents were purchased from HiMedia Laboratories to study the radical scavenging activities. ESR spectra were recorded on JES-FA200 ESR spectrometer, JOEL at an operating frequency of 9.4 GHz (X-band). FTIR spectra of the sample pellet prepared by adding KBr were recorded on Perkin Elmer spectrometer. DSC measurements were performed on a DSC-TA Q10 model calorimeter at a heating rate of 20ºC/min in flushing Nitrogen gas. The X-ray diffractograms were recorded on Bruker D8 Advance XRD. The morphology of lignin was examined under TESCAN VEGA 3 LMU with a magnification of 750 and 1000×. Lignin antioxidant capacity was determined by using DPPH scavenging activity and reducing power. The methods were followed from Mir Gul et al [3] and Qi Lu et al [4] with minor modifications.

3. Results and Discussion

Unirradiated lignin shows a weak ESR singlet with g-value of 2.0035 and it is assigned due to poly-conjugated radicals whereas the irradiated lignin shows a strong singlet with increasing dose assigned to two types of radicals (i) poly-conjugated radical (ii) peroxy radical. Lignin contain phenols, alcohol, glycosidic and acetal oxygen groups. When lignin is irradiated with electron beam, dissociation of these groups takes place and degradation occurs producing primary radicals. Kuzina et al [5] have used D-band ESR spectroscopy to resolve the singlets and detected the existence of poly-conjugated radicals in lignin. In the present studies, ESR spectrum of irradiated lignin is a superposition of singlets arising due to the poly-conjugated radicals and peroxy radicals. There is a gradual increase in intensity of ESR signal with radiation dose. ESR spectra are also recorded at RT, 333K, 363K, 413K and 453K temperatures shown in Figure 1. As the temperature is increased, the radicals gain thermal energy and begin to interact with themselves or with other radicals. It is evident that the doublet like structure appeared around 363K is disappeared at 413K i.e. around glass transition temperature of lignin. The decayed component is assigned to peroxy radical. Since the poly-conjugated radicals have high thermal stability, the singlet at 450K corresponds to poly-conjugated radicals.
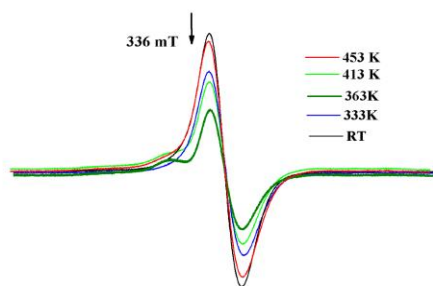
temperatures RT, 333K, 363K, 413K and 453K.

Absorption spectra of lignin reflects the change in the chemical structure induced on irradiation. The FTIR studies confirm the enhancement in conjugation of lignin on irradiation. These changes suggest that cleavage of phenoxy groups on irradiation and subsequently led to the formation of unsaturated conjugated group. DSC thermograms shows a negligible change in glass transition temperature (T_g) but at a radiation dose of 90 kGy, the T_g decreased abruptly. The decrease in T_g is assigned to a decrease in molecular weight and plastification phenomena in lignin which arise due to the intermolecular interaction of hydroxyl groups. SEM micrographs shows numerous pits on the cross-section surface of lignin granule. When the lignin is treated with EB radiation, cracks were developed on the surface of the cross-section view of granule. The antioxidant activity of lignin increased on EB irradiation was checked with DPPH radical scavenging activity and reducing power as shown in Figure 2.
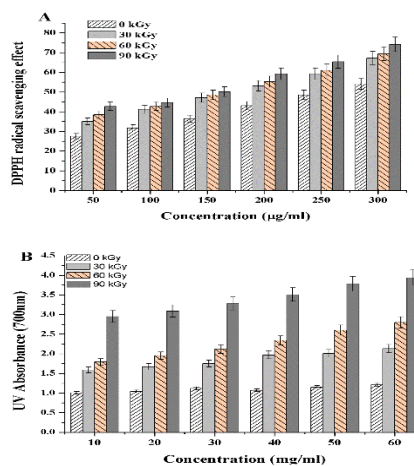
and irradiated lignin (A), Reducing power of unirradiated and irradiated lignin (B)

4. Conclusion

Electron beam irradiation of kraft lignin induce both physical and chemical changes. Cleavage of glycosidic oxygen groups in lignin is occurred producing poly-conjugated and peroxy radicals under oxygenated conditions. Due to the chain cleavage, glass transition temperature is found to decrease. Electron beam irradiation also decreased particle size with heavy damage of surface. Antioxidant properties are also observed to increase due to irradiation of lignin.

References:
1) Chuaqui CA, Rajagopal S, Kovacs A, Stepanik T. *Tetrahedron* 1993, 49, 9689-9698.
2) Braca A, Sortino C, Politi M, Morelli I, Mendez J. *Journal of Ethnopharmacol* 2002, 79, 379–381.
3) Gul ZM, Farhan A, Anand K, Qureshi A, Irfan G. *BMC Complementary and Alternative Medicine* 2013, 13: 1-12.
4) Qi L, Minghua Z, Yuangang Z, Wenjun L, Yang L, Ying Z, Xiuhua Z, Xiunan Z, Xiaonan Z, Wengang L. *Food Chemistry* 2012, 135, 63–67.
5) Kuzina SI, Brezgunov AY, Dubinskii AA, Mikhailov AI. *Radiation chemistry* 2004, 38, 298-305.

Facile growth of carbon nanotube electrode from electroplated Ni catalyst for supercapacitors

V. Yordsri,[1,2] W. Wongwiriyapan,[1,3,4*] C. Thanachayanont[2]

[1]College of Nanotechnology, King Mongkut's Institute of Technology Ladkrabang, Chalongkrung Rd., Lardkrabang, Bangkok, Thailand

[2]National Metal and Materials Technology Center, 114 Thailand Science Park, Paholyothin Rd., Klong 1, Klong Luang, Pathumthani, Thailand

[3]Nanotec-KMITL Center of Excellence on Nanoelectronic Device, Chalongkrung Rd., Ladkrabang, Bangkok, Thailand

[4]Thailand Center of Excellence in Physics, CHE, Si Ayutthaya Rd., Bangkok, Thailand

Abstract: A facile growth of carbon nanotubes (CNTs) was facilitated by the use of direct-current plating technique for catalyst preparation. Ni nanoparticles (NPs) were deposited on Cu sheet at different applied voltages of 1.0, 1.5 and 2.0 V and were subsequently used as catalyst for CNTs synthesis by chemical vapor deposition (CVD) method. Ni NPs size could be controlled by electroplated voltage. A voltage of 1.5 V is the optimum condition to deposit a uniform Ni NPs with a narrow size distribution of 55±3 nm, resulting in the synthesized CNTs with a uniform diameter of approximately 60±5 nm with graphitic layers being parallel to the CNTs axis. Ni NPs with a narrow size and a uniform diameter is a key for uniform CNT synthesis. Moreover, the CNTs synthesized from electroplated Ni NPs shows the potential application as pseudocapacitor.

Keywords: Electroplating, Carbon nanotube, Chemical vapor deposition, Pseudocapacitor

Introduction

Carbon nanotube (CNT) shows a great potential to apply in various applications to improve device properties such as electronics devices, energy storage devices and sensors. Chemical vapor deposition (CVD) is one of the main methods for CNT synthesis. Metal catalyst is an essential ingredient for CVD approach (Lee *et al.,* 2002). For practical application, facile catalyst preparation is strongly required. In this study, a facile growth of CNTs was proposed by using direct-current (DC) electroplating for Ni nanoparticles (NPs) preparation and CNTs was synthesized by CVD using ethanol as carbon source. Moreover, for potential application demonstration, the supercapacitor based on the synthesized CNTs were fabricated and its electrochemical properties were characterized.

Experimental

The 4x20 mm^2 Cu sheet (Nilaco Corporation, Japan) and Ni ingot were connected as anode and cathode, respectively. The commercial Ni electroplating was used as electrolyte. Electroplating temperature, time and distance between electrodes were fixed at 45⁰C, 5 min and 100 mm, respectively, while the applied voltages were varied at 1.0, 1.5 and 2.0V. The CNT synthesis procedure is described as follows. A quartz tube reactor was filled with Ar gas at a flow rate of 500 sccm and the Ni catalyst-electroplated Cu sheet was heated to 800⁰C. Ethanol (99.9%, Labscan) was vaporized and switched into the quartz tube by Ar bubbling for 20 min for CNT growth. Morphology of the electroplated Ni was characterized by atomic force microscopy (AFM). Morphology, diameter and crystallinity of the synthesized CNTs were characterized by filed emission scanning electron microscopy (FESEM) and transmission electron microscopy (TEM). The electrochemical measurements were carried out in a three-electrode setup connected to an electrochemical workstation (Metrohm AUTOLAB PGSTAT 302). The synthesized CNT on Ni-electroplated Cu sheet with an area of 4x10 mm^2 was used as a working electrode. Pt and Ag/AgCl electrodes were used as counting and reference electrode, respectively. 1M H_2SO_4 aqueous solution was used as the electrolyte

Results and discussion

Ni NPs could be formed by all electroplated voltage conditions. The average size of Ni NPs deposited at electroplated voltages of 1.0, 1.5 and 2.0 V were 120±14 nm, 55±3 nm and 103±12 nm, respectively (data not shown). Thus, Ni NPs with a controllable size can be achieved under the controlled electroplating condition. Figures 1(a)−1(c) show SEM images of CNTs synthesized from Ni NPs deposited at electroplated voltages of 1.0, 1.5 and 2.0 V, respectively (hereinafter referred to as Ni1.0-
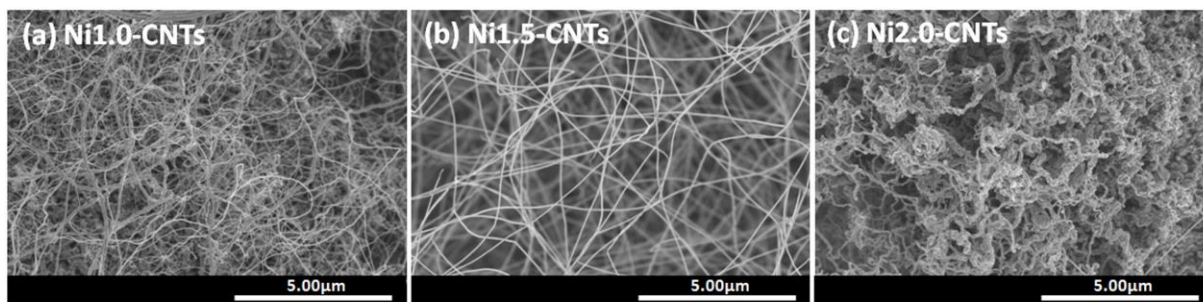
Figure 1. SEM images of (a) Ni1.0-CNTs, (b) Ni1.5-CNTs and (c) Ni2.0-CNTs.

CNTs, Ni1.5-CNTs and Ni2.0-CNTs, respectively). After CVD process, all Cu sheet surfaces were wholly covered with a black powder by visual. All Ni NPs could act as a catalsyt to synthesize tubular shapes but different in morphologies and structures. For Ni1.0-CNTs, the synthesized CNTs were tangled in network while the Ni1.5-CNTs were straight with high aspect ratio. For Ni2.0-CNTs, the synthesized CNTs were curly and agglomerated in cluster structure. From TEM observation, it was found that graphitic layers of the Ni1.0-CNTs were angle to the tube axis wall, while graphitic layers of the Ni1.5-CNTs were parallel to the tube axis (data not shown).

For the preliminary test as supercapacitor application, the Ni1.5-CNTs on Cu sheet was further evaluated their electrochemical properties. Figure 2 shows the cyclic voltammetry (CV) curves of the Ni1.5-CNTs in the potential range of -0.3−0.2 V at different scan rates. Every CV curves show a pair of redox current peaks, showing that faradic pseudocapacitance is dominantly contributed to the electrochemical properties (Li *et al*., 2013). With increasing scan rate, the current increased and the gap between redox peaks widened while the shape of the CV curves were retained, indicating the redox reversibility. This psesudocapacitive character may arises from the residual Ni NPs used as catalyst for CNTs synthesis. The specific capacitance calculated from the CV curve at a scan rate of 5 mVs^{-1} is approximately 53 Fg^{-1}. This preliminary results show that the facile growth of CNTs from Ni NPs deposited by DC electroplating method was successful. The synthesized CNTs shows a potential application as supercapacitor electrode. However, further detailed works and optimization are needed

Conclusion

Novel synthesis of CNTs with simple and low cost method was proposed by the use of controllable electroplated Ni NPs as catalyst and the use of ethanol as carbon source during CVD process.
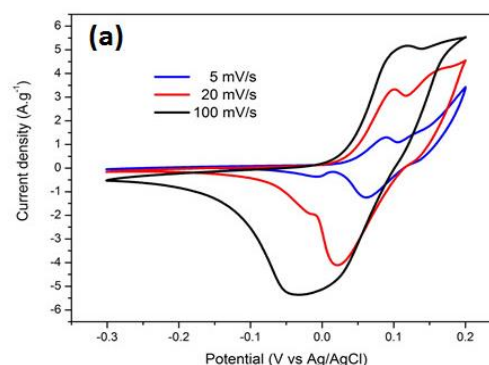
with different scan rate

The electroplated voltages directly affect the size of Ni NPs, resulting in the morphology and structure of CNTs. The graphitic layers of CNTs can be selectively parallel to the tube axis with a narrow tube diameter distribution of 60±5 nm. The synthesized CNTs show a potential application as supercapcitor with a specific capacitance of 53 Fg^{-1} at a scan rate of 5 mVs^{-1}. The optimization of Ni NPs structure and the optimum amount of Ni NPs and CNTs may improve the electrocapactive performance.

References:
Lee, C.J., Park, J., Yu, J.A. (2002), Catalyst effect on carbon nanotubes synthesized by thermal chemical vapor deposition, *Chem. Phys. Lett.*, 360, 250-255.

Li, H.B, Yu, M.H., Wang, F.X., *et al*. (2013), Amorphous nickel hydroxide nanospheres with ultrahigh capacitance and energy density as electrochemical pseudocapacitor materials, *Nature Communications*, 4, 1-7.

Immobilization of Urease Based on Adsorption in Eggshell Membrane for Urea Biosensor Application

Thanarat Suwanchaituch, Supranee Imthong, Kornvalai Panpae*

Department of Chemistry, Faculty of Science, King Mongkut's University of Technology Thonburi, KMUTT, Bangkok, Thailand

Abstract: In aqueous solutions, biomolecules such as enzymes lose their catalytic activity rather rapidly, because enzymes can suffer oxidation reactions or its tertiary structure could be destroyed at the air/water interface, hence making the use of enzyme and reagents both expensive and complex. These problems can be minimized considerably by enzyme immobilization. By attachment to an inert support material, bioactive molecules may be rendered insoluble, retaining catalytic activity, thereby extending their useful life. In view of the above necessity and advantages, since the 1960s, an extensive variety of techniques have been developed to immobilize biomolecules, including adsorption, covalent attachment and entrapment in various polymers (Gupta *et al*; 2007). In general, adsorption techniques are easy to perform, but the bonding of the biomolecules is often weak and such biocatalysts lack the degree of stabilization and easy leakage from the matrix. A biosensor is an analytical tool that comprises two essential components—an immobilized biocomponent, in intimate contact with a transducer that converts a biological signal into a measurable electrical signal (Turdean; 2011). Some reports (D'Souza *et al*; 2012, Marzadori*, et al*; 1998) on biosensors have been published using eggshell membrane as a supporting matrix for immobilization of enzymes such as D-amino oxidase, catalase, myrosinase, tyrosinase and glucose oxidase . The technique, which mostly used for immobilization of enzyme on eggshell membrane, involved adsorption followed by cross-linking with glutaraldehyde. In this study, a novel immobilization based on adsorption method em ploying eggshell membrane from hard-boiled eggs and fresh eggs as supporting matrice and polyethyleneimine (PEI) as a carrier system was investigated using Jack bean urease as a model enzyme. Eggshell membranes were studied differentiation of morphology after urease immobilization by SEM. They were studied the changes in IR spectra after urease immobilization by FTIR. Immobilized membrane was attached with a standard pH-electrode. Biosensors of eggshell membrane from fresh egg and hard- boiled egg response urea concentration range from 7.5 mM to 200 mM. The response time of biosensors was 300 s. Biosensors can be reused more than 10 times with no significant decreasing of activity. The efficiency of urease immobilization on fresh membrane is as well as that of boiled egg membrane.

1. Introduction

Enzymes have been utilized in a large number of practical applications, particularly in biomedical and bio- technological fields, through immobilization on a variety of supports. These immobilized products were intended for use in the construction of artificial organ systems, biosensors or bioreactors. Immobilization is advanta- geous because; (1) it extends the stability of the bioactive species by protecting the active material from deactivation; (2) enables repeated use; and (3) it provides significant reduction in the operation costs. Many methods exist for the immobilization of enzymes but usually one of four methods is used, physical adsorption, entrapment, co-polymerization, and covalent attachment (Arica *et al*.; 2001). The methods and supports employed for enzyme immobilization are chosen to ensure the highest retention of enzyme activity and its stability and durability. Urease hydrolyses urea, yielding ammonia and carbonate. Immobilized urease has been widely used in biosensors for diagnostic purposes, in the determination of urea in biological fluids, in artificial kidney devices for the removal of urea from blood for extracorporeal detoxification, in enzyme reactor for the conversion of urea present in fertilizer wastewater effluents or in the food industry for removal of urea from beverages and foods (Cevik *et al*; 2011). A variety of synthetic as well as natural polymeric materials have been used for the immobilization of enzymes for biosensor preparation. Among these natural materials, especially of proteinic origin, have shown promise uses. One of these natural materials is the eggshell mem brane. Some reports on biosensors have been published using eggshell membrane as a supporting matrix for immobilization of enzymes such as D-amino oxidase, catalase, myrosinase, tyrosinase and glucose oxidase (D'Souza *et al*; 2012). The technique, which mostly used for immobilization of enzyme on eggshell membrane, involved adsorption followed by cross-linking with glutaraldehyde.Glutaraldehyde has been used for fixing the enzyme to the support and polyethyleneimine (PEI) has been used for increasing the enezyme activity.

The study presented here used eggshell membrane as a supporting matrix for urease immobilization. A novel immobilization based on adsorption method em ploying eggshell membrane from hard-boiled eggs and

fresh eggs as supporting matrice and polyethylene-imine (PEI) as a carrier system was investigated using Jack bean urease as a model enzyme.

2. Experimental
2.1 Materials and reagents

Urea (enzyme grade), Jack bean urese (type III) with specific activity of 35 units / mg protein was obtained from Sigma. Urea (enzyme grade), polyethyleneimine (PEI) were obtained from Sigma Chem. Co. USA. All other chemicals used were of analytical reagent grade.

2.2 Immobilization of urease on eggshell membrane

Fresh and hard-boiled eggs were broken and the eggshell membrane was peeled off carefully from the fresh eggshell. The membrane was washed with milliQ water. Circular pieces (2 cm diameter) were cut and were dried in an incubator at 35 °C for 1 h and stored at 4 °C in the refrigerator. The membranes were soaked for 2 h in 5% aqueous solution of PEI (pH 7.0) at room temperature. The PEI-soaked membranes were rinsed with milliQ water, air-dried for 1 h and were stored in a petri dish at 4 °C. An aliquot of 100 μL of jack bean urease (100 units activity) was adsorbed on each membrane. The membranes were air dried at room temperature for 24 h. The immobilized membranes were washed and immersed in buffer (50 mM phosphate pH 7.0) and stored at 4 °C.

2.3 Membrane characterization
2.3.1 SEM

SEM observations were carried out on gold sputtered membrane samples using JEOL JSM-5410 LV scanning electron microscope. Membrane samples for SEM studies were prepared by soaking in isopropanol, then in hexane for 3 h and subsequent vacuum drying at 40 °C. The cross-sections of samples were prepared by fracturing in liquid nitrogen.

2.3.2 FTIR study of enzyme immobilized membrane

Membranes were studied by FTIR spectra and scanned in the range of 4000–400 cm−1 on Jasco (Model FTIR-660 plus) FTIR Spectrometer. The membranes were pressed directly onto the attenuated reflectance with the sampling unit.

2.4 Calibration of biosensor using immobilized eggshell membrane

The standard solution of urea (0.5, 2.5, 5, 10, 25, 50 and 100 mM) was prepared in milliQ water. The standard glass electrode was attached with urease eggshell membrane. It was first stabilized with flow of buffer as indicated by a stable baseline potential. Subsequently, 1 mL solution of standard concentration of urea was injected in the vessel and changes in potentials in mVolts were recorded.

2.5 Activity assay

The membrane with the immobilized enzyme was immersed in a 0.1 M solution of urea in 0.05 M sodium phosphate buffer, pH 7.0, 37°C. The membrane (2 cm diameter) was attached to the tip of the standard glass electrode with the help of an O-ring and then placed in the reaction vessel. The baseline potential of the sensor was achieved with flow of buffer solution (50 mM phosphate pH 7.0). The solution was stirred during the measurement on a magnetic stirrer. The membrane electrode was allowed to stabilize for 10 min before recording the reading. Between measurements, the electrode membrane was washed with buffer and used for the next reaction.

The relative activity was determined as the ratio between the specific activity of a bound enzyme and the specific activity of the free enzyme, multiplied by 100.

2.6 Determination of immobilized urease activity and immobilized protein

The amount of protein bound to the modified membranes was determined by the method of Lowry et al (1951).

3. Results and discussion
3.1 SEM study of the urease immobilized eggshell membrane

SEM study of immobilized eggshell membrane showed a network- like structure without any aggregation on the surface. Membrane consists of highly cross-linked protein fibers and cavities and the observation was similar to the previous report (D'Souza *et al*; 2012). Surface morphology of eggshell membrane showed the fibers and cavities of the eggshell membrane being occupied with PEI and urease enzyme after immobilization (Fig.1). SEM micrographs indicated that enzyme was successfully immobilized on the surface of eggshell membrane using PEI.

3.2 FTIR study of urease immobilized eggshell membrane

FTIR spectra of eggshell membrane are shown in Figure 2. It is evident that the presence of amino groups facilitates the immobilization of the enzyme by a covalent linkage to glutaraldehyde-pretreated membrane. As it can be seen (Fig. 2). It was observed that four new peaks appeared at 3068, 1416, 1070

and 983 cm^{-1} after the PEI treatment on eggshell membrane, which were corresponding to the =C-H stretch of alkenes, -C-H bending of alkanes, C-N stretch of aliphatic primary and secondary amines (peptide) and C -H blending of primary and secondary amines respectively. Results showed the occurrence of PEI on egg shell membrane. After immobilization of urease enzyme on eggshell membrane. Results showed the presence enzyme on egg- shell membrane as indicated in term of C-N amide bond in FTIR study.The new groups increased the hydrophilicity of the initial membrane.

Unimmobilized   Immobilized
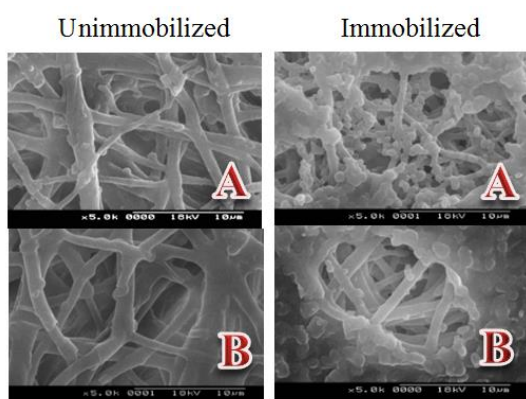
Fig.1 SEM image of urease immobilized on eggshell membrane extracted from (A) fresh egg and (B) hard-boiled egg.

Figure 1: SEM image of urease immobilized on egg-shell membrane extracted from (A) fresh egg and (B) hard-boiled egg.
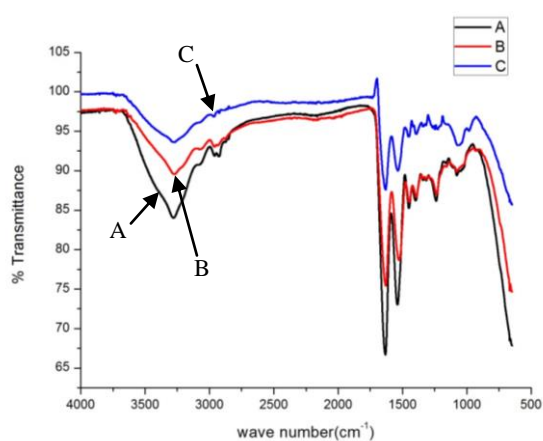

Figure 2: FTIR study of eggshell membrane (A) Only eggshell membrane, (B) Eggshell membrane treated with PEI and (C) Urease immobilized on the PEI treated eggshell membrane.

3.3 Activity and stability of immobilized urease and immobilized protein

The general behaviors of urease immobilized onto membranes under different conditions of immobiliza-

tion were studied. The activity of both free and immobilized urease was determined by measuring the amount of ammonia liberated from the urease-catalyzed hydrolysis of urea per unit time :

$$(NH_2)_2CO + 2H_2O \xrightarrow{\text{urease}} H_2CO_3 + 2NH_3$$
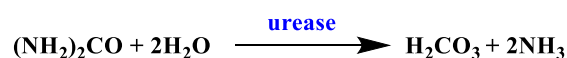
The percentages of immobilization are summarized compared with soluble enzyme.The highest activity (53-54%) was measured for urease bound to egg shell membranes at the optimum conditions: 0.01% enzyme solution, pH7.3 and 10% w/v PEI time 2h, immobilization temperature 4 $^{\circ}$C and immobilization time 24h. The stability of urease was shown by calculating the half-life of immobilized compared with soluble urease (the results not shown). **The** half-life of immobilized urease was approximately 37 days when kept in 50 mM sodium phosphate buffer (pH 7.3) at 4°C compared with a half-life of 28 days for the soluble urease under identical conditions. The higher stability of immobilized urease can be ascribed to the protection of denaturation as a result of the attachment of urase onto the eggshell membrane cross-linked and adsorbed by PEI. Furthermore, the storage stabilities showed good linearity with respect to the activity

3.4. Response time, detection range and detection limit

The biosensor prepared from urease immobilized on egg shell membrane was used sucessfully for estimation of urea samples. The calibration curve obtained by plotting the potential difference (mV) across the two leads of the separated glass electrode against the concentration of urea is shown linearly in Figure 3 and the response time with the present experiments (0.01 M urea at 7.3) is shown in Figure 4.
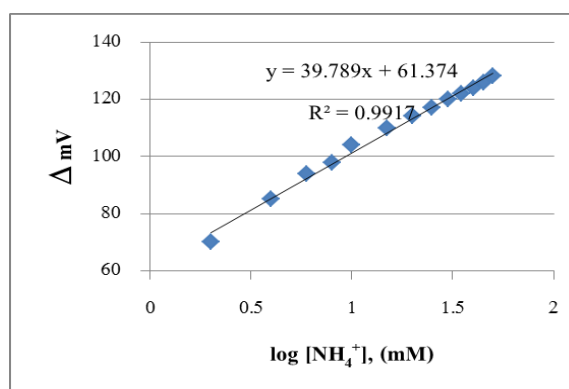

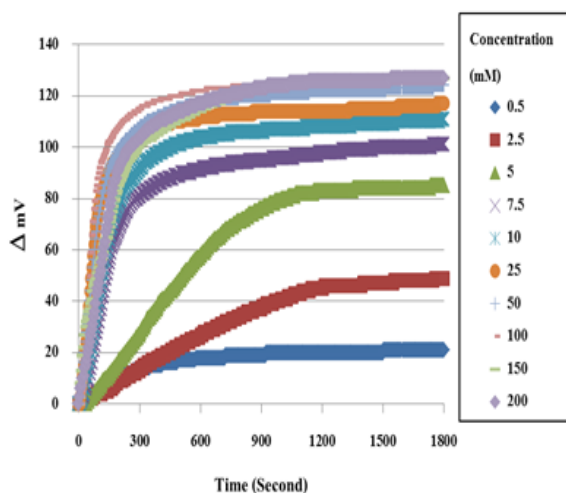Figure 3: Calibration of the biosensor using immobilized eggshell membrane.

Figure 4: Response time of enzymatic activity of urease eggshell

The response time observed in the present study is 300 s comparable with those reported for other urea biosensor (Srivastava et al.,2001; Schitogullari et al; 2002). Several parameters move evaluated to ascertain the optimum performance of the base line, slope of the calibration curve and reliability of the biosensor. The detection limit in our case is approximately 7.0 mM. At different time intervals, variation in electrode potential was monitored using 0.01M urea solution. A little loss of activity was observed over of 4-7 weeks and the reproducibility of the urea assay for the serum samples obtained from our biosensor was expected to be very good compared with other reports (Cevik *et al*; 2011, D'Souza *et al*; 2012, Magalhães *et al*;1998).

4. Conclusion

Present communication describes a much simpler method of immobilization of urease. Eggshell membranes both from fresh egg and hard-boiled egg can be used for the immobilization of enzymes through adsorption for biosensor application. Biosensor exhibited sigmoidal responses for the urea concentration range from 7.5 to 200 mM. The estimated response time of the biosensor was 300 s. A single membrane was reused not less than 10 cycles of the urea hydrolysis reaction. The immobilized membranes were stable for 2 months when stored in buffer at 4°C.

References:

Arica, MY.,Kacar, Y., Egene, A., Denizil, A.(2001), Reversible immobilization of lipase on phenylalanine containing hydrogel membranes, *Process Biochem.*, 36, 847-854.

Cevik, E., Senel, M., Abasiyanik, M.(2011), Immobilization of urease on copper chelated EC-Tri beads and reversible adsorption, Afri. J Biotechnol., 10, 6590-6597.

D'Souza, S.F., Kumar, J., Jha, S.K., Kubal, B.S. (2012), Immobilization of the urease on eggshell membrane and its application in biosensor, *Mater. Sci. Eng.C*, 33, 850-854.

Gupta, R., Chaudhury, N.K. (2007), Entrapment of biomolecules in sol-gel matrix for applications in biosensors: Problems and future prospects, *Biosens. Bioelectron.*, 22, 2387-2399.

Lowry, O.H., Rosebrough, N.J. Farr, A.L., Randall, R.J (1951). Protein measurement with the Folin phenol reagent. *J. Biol.Chem.,*193, 265-275.

Magalhães, J.M.C.S., Machado, A.A.S.C.(1998), Urea potentiometric biosensor based on urease immobilized on chitosan membranes. *Talanta,* 47, 183-191.

Srivastava, P.K., Kayastha, A.M., Srinivasan, F.S (2001), Characterization of gelatin-immobilized pigeonpea urease and preparation of a new urea biosensor. *Biotechnol. Appl. Biochem.* , 34, 55-62.

Sehitogullari, A., Uslan, A.H. (2002), Preparation of a potentiometric immobilized urease electrode and urea determination in serum, *Talanta.* 57, 1039-1044.

Turdean, G.L. (2011), Design and development of biosensors for the detection of heavy metal toxicity, Int. *J. Electrochem.*, 2011, Article ID 343125, 15 pages.

Needle-less Jet Injection System with Multi-Pore Nozzle for Viscous Drug Delivery Applications

Y. C. Jo,[1*] H. K. Hong,[1] Y. S. Choi[1], H. S. Kim[2]

[1]Korea Electronics Technology Institute, Medical IT Convergence Research Center, SeongNam-Si, South Korea
[2]Korea Electronics Technology Institute, Contents Research Center, SeongNam-Si, South Korea

Abstract: Jet injection is an important needle-free drug delivery method for insulin and vaccines[1-3]. Jet injections employ a high speed jet to puncture the skin and deliver drugs without the use of a needle. Although jet injections have been used for tens of years and continue to be researched for new applications. Needle-free jet injection constitute an important method of drug delivery, especially for beauty treatment. An experimental study was performed using a newly developed air-powered needle-free jet injector(Figure 1) to investigate the relationship between nozzle pore variation and delivered viscous liquid drug volume. The most important injector fuction for beauty treatment are the penetration depth and diffusion area which is related with jet velocity and nozzle pore number. The driver pressure of the air cylinder considered in this work ranged from 6 to 10 bar provided by an air compressor fitted with a precision regulator. Individual nozzle and pressure combinations were tested a minimum of ten times in order to ensure consistent and reliable results. Developed injector in this work is the first needle-free jet injector prototype with multi-pore nozzle for viscous drug delivery upto 12cps, 1% Hyaluronic Acid(HA) solution. The proposed injector has three types of nozzle structure, such as single pore, 4 pores array and 9 pores array nozzles(Figure 2). Experimental studies showed that the penetration depth and diffusion of drug into skin continue to decrease as the nozzle pore number increase(Figure 3, Figure 4).

Keywords: Needle-free, Jet injector, Drug delivery, Skin, High viscosity, Beauty treatment

Figure 2: Design models of the injector nozzles of the proposed jet injector used in these experiments. Each nozzle has different pore number. (a) single pore, (b) 4 pores array (c) 9 pores array
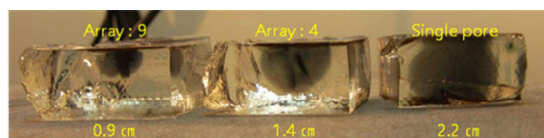
Figure 3: Sample pictures showing the jet penetration generated by the air-powered injector with three different nozzle configurations(9, 4 and single pore) into the 5% gelatin block. All of the pore diameter was 100 um in common and 1% Hyaluronic Acid(HA) solution was used for this experiments
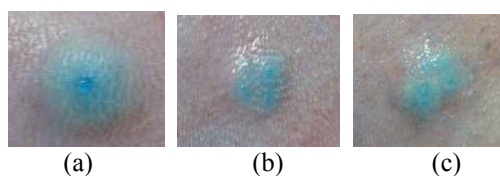
Figure 4: Guinea pig skin test results of the proposed device using designed nozzle with various pore number,   (a) 1 pore, (b) 4 pores array (c) 9 pores array

References:
Portaro, R., Dick Ng, Hoi. (2013) Experimental analysis of the performance of an air-powered needle-free liquid jet injector, *IEEE EMBS.*

Baxter, J., Mitragotri, S.(2005), Jet-induced skin puncture and its impact on needle-free jet injections : Experimental studies and a predictive model, *Int. J. Controlled Release*, 106, 361-373.

Baxter, J., Mitragotri, S.(2005), Needle-free jet injections : dependence of jet penetration and dispersion in the skin on jet power, *Int. J. Controlled Release.*, 97, 527-535.
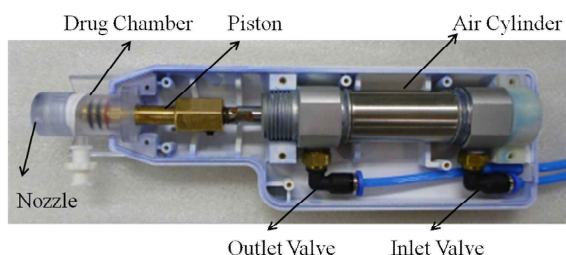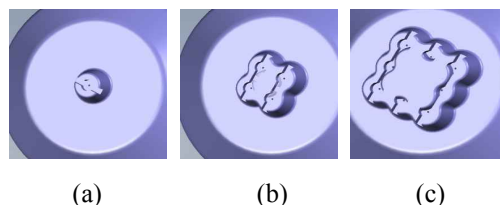
Figure 1: A New needle-free jet injector developed in these work. The injector is driven by a air compressor. The nozzle is made of clear thermoplastics.